Biophysical Modeling of the Growth and Motion of Bacterial Populations

Daniel B. Amchin

a dissertation
presented to the faculty
of princeton university
in candidacy for the degree
of Doctor of Philosophy

recommended for acceptance
by the Department of
Chemical and Biological Engineering

Adviser: Sujit S. Datta

May 2022

Abstract

The growth and spread of bacterial populations are processes of broad significance. The coupling between cells, the structures of their environment, and the chemical makeup of their environment underlies how bacteria survive and spread. For example, the environments bacteria inhabit often confine individual cells, modifying both their individual and collective motion in previously overlooked ways. Thus, in this thesis, I first use biophysical modeling and numerical simulations to uncover new features of cell motion that arise due to confinement within a heterogeneous medium. In particular, I develop a continuum model to better understand experimental observations of traveling bacterial fronts in highly-confining porous media. Using this model, I explore the influence of confinement on (i) the dynamics of bacteria spreading, (ii) the overall morphology of a migrating population, and (iii) the robustness of the population to morphological perturbations. Then, as a step toward similarly describing the dynamics of mixed communities—which are often composed of different species requiring different chemical conditions to thrive—I use biophysical modeling and numerical simulations to study the growth of aerobes and anaerobes in an environment of shared nutrient. In this case, the coupling between nutrient consumption, oxygen consumption, and growth leads to striking new dynamics, such as hysteresis/bistability and growth oscillations, amidst varying chemical conditions. Altogether, this work establishes a quantitative framework to predict, and potentially guide strategies to control, microbial behavior for diverse applications in biomedical science and the environment.

Contents

Citations to Previously Published Work

This dissertation is based on the following work:

Chapter 2:
"Chemotactic migration of bacteria in porous media",
Tapomoy Bhattacharjee*, **Daniel B. Amchin***, Jenna A. Ott,
Felix Kratz, and Sujit S. Datta, *Biophysical Journal* 120, 3483 (2021)
*Equal contribution.

Chapter 3:
"Influence of confinement on the spreading of bacterial populations",
Daniel B. Amchin, Jenna A. Ott, Tapomoy Bhattacharjee,
and Sujit S. Datta, in press *PLoS Computational Biology*, (2022).

Chapter 4:
"Chemotactic smoothing of collective migration",
Tapomoy Bhattacharjee*, **Daniel B. Amchin***, Ricard Alert*,
Jenna A. Ott, and Sujit S Datta, *eLife* 11, 71226 (2022)
*Equal contribution.

Chapter 5:
"Microbial mutualism generates multistable and oscillatory growth dynamics",
Daniel B. Amchin, Alejandro Martínez-Calvo, and Sujit S. Datta,
submitted, *Biophysical Journal* (2022).

Citations to other work co-authored during the course of the degree, not included in this thesis:

"Forced imbibition in stratified porous media: Fluid dynamics
and breakthrough saturation",
Nancy B. Lu*, **Daniel B. Amchin***, and Sujit S. Datta,
Physical Review Fluids 6, 114007 (2021) *Equal contribution.

"Infection Percolation: A Dynamic Network Model of Disease Spreading",
Christopher A. Browne*, **Daniel B. Amchin***, Joanna Schneider*,
and Sujit S. Datta, *Frontiers in Physics* 9, 645954 (2021) *Equal contribution.

"Forced Imbibition in Stratified Porous Media",
Nancy B. Lu, Amir A. Pahlavan, Christopher. Browne, **Daniel B. Amchin**,
Howard A. Stone, and Sujit S. Datta, *Physical Review Applied* 14, 054009 (2020).

"Controlling Capillary Fingering Using Pore Size Gradients in Disordered Media"
Nancy B. Lu, Christopher A. Browne, **Daniel B. Amchin**,
Janine K. Nunes, Sujit S. Datta, *Physical Review Fluids* 4, 084303 (2019).

To Emma Amchin, the love of my life, with whom I have traveled far and grown exponentially.

Acknowledgments

It is my pleasure to acknowledge H. A. Stone, N. S. Wingreen, P-T Brun, S. Y. Shvartsman, Y. L. Loo, B. Austin, T. Emonet, K. Lushi, for their invaluable thoughts and insightful comments on my work. In particular, thank you to Bob Austin and his lab for sharing their bacterial strains with me and my colleagues in the Datta Lab.

Thank you to Karen Oliver, Jacqueline Armstrong, Pam Raney, and the rest of the administrative staff of the CBE department.

Thank you to my mentors and advisors at The University of Southern California, Drexel University, and The National Institutes of Health, who helped guide me on my path to graduate school.

Thank you to my friends Jordan Shickman, Lydia Lo, Ray Lo, Trevor Jones, and Molly Jones.

Thank you to my Princeton colleagues Nick Caggiano, Yejoon Seo, Jason Liu, Average Phan, and my CBE cohort.

Thank you to my undergraduate mentees, Rhea Braun and Cristian Arens.

Thank you to the all the members of the Datta Lab for making our workplace a vibrant, supportive community that has benefited me greatly: Nancy Lu, Christopher Browne, Jenna Anne Ott-Moore, Joanna Schneider, Anna Hancock, Sebastian Gonzalez La Corte, Tapomoy Bhattacharjee, Nadine Ziegler, Felix Kratz, Jeremy Cho, Alejandro Martínez-Calvo, Carolina Trenado Yuste, Hongbo Zhao, Jean-François Louf, Galen Mandes, Navid Bizmark, Konane Bay, Babak Vajdi Hokmabad, Emily Chen, Selena Chiu, Caroline Adkins, Kimberly Lu, Brianna Royer, Yaxin Duan, Hao Nghi Luu, Richard Huang, Arrow (Arabella) Dill-Macky, Callie Zheng, Cecilia Quirk, MaryKate Neff, Malcolm Slutzky, Kevin Yeung, Aaron Bourque, Maggie O'Connell, Audrey Shih, Glenda Chen, Emily de Jong, Emmanuel Mintah, Rebekah Adams, Shalaka Madge, Anvitha Sudhakar, Maziar Derakhshandeh, Nathanael Ji, and Florence Odigie.

To my advisor Sujit Datta, thank you for teaching me to *bring the drama*, to accept praise, and to appreciate those I have the privilege of working alongside.

To my family: Lori, Jess, and Ron Amchin; Arielle, Louis, Eliana, and Jane Orazio; Doyle Harrelson; Richard and Janet Adler; and the dogs. Thank you for always being there for me and believing in me.

To my wife Emma, thank you for standing by me, standing up for me, standing up to me, and standing me back up... and for more than I could hope to put into words, but might fit into lyrics someday.

Finally, to Squid, thank you for being a very good boy while attending graduate school with me.

1

Introduction

1.1 Modeling bacteria spreading under confinement

The ability of bacterial populations to spread through their surroundings plays a pivotal role in our everyday lives. In some cases, their spread can be harmful, underlying the progression of infection in the body[1–8] and the spoilage of foods[9,10]. In other cases, it can be beneficial, enabling bacteria to deliver drugs to hard-to-reach spots in the body[11,12], move

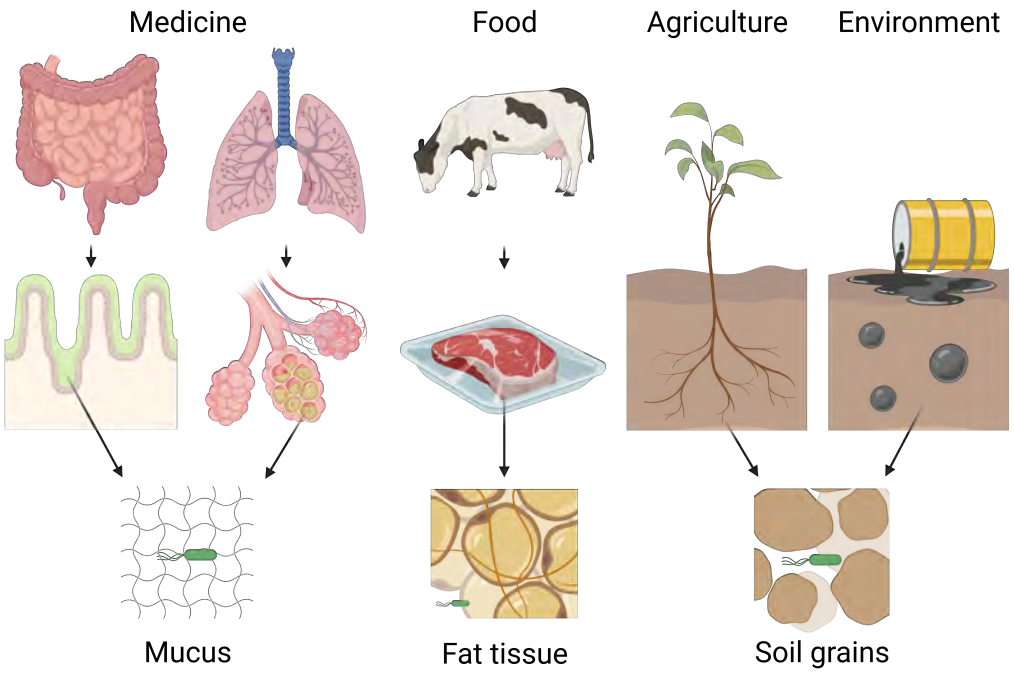

Figure 1.1: Important contexts for bacteria motion in complex environments. (Left) In the gut and lungs, how bacteria interact and move through mucus is crucial to human health and medicine. (Middle) Meat spoilage is impacted by the motion of cells through tissues. (Right) Agriculturally important interactions with plant roots and contaminant removal using bacteria for bioremediation are both critically impacted by cell motility through packed grains of soil. Graphic created with BioRender.com.

toward and protect plant roots in soil[13–17], and degrade environmental contaminants[18–22] (Fig. 1.1). In all these cases, bacteria typically inhabit crowded environments, such as soils, sediments, and biological tissues/gels, in which solid obstacles confine the cells and regulate their spreading. Therefore, the development of accurate models of bacterial spreading in a variety of environmental contexts is critically important for the prediction and control of bacterial populations in medicine, food, agriculture, and the environment. However, despite their potentially harmful or beneficial consequences, there is still limited understanding of how confinement in a porous medium alters the ability of bacteria to migrate: typical 3D media are opaque, precluding direct observation of cellular motion in situ. Thus, cur-

rent understanding of migration is based on studies performed in bulk liquid.

Many species of bacteria self-propel in fluid using multiple slender, actively moving $\sim$ 5 μm long appendages protruding from the their surface called flagella[23] (as shown in Fig. 1.2). A single bacteria cell rotates multiple helical flagella synchronously as a bundle that "pushes" surrounding fluid[24] and propels the cell forward along directed, ballistic "runs" of speed $\sim$ 25 μm/s. Runs last on average $\bar{\tau}_{\text{run}} \sim 2$ s making the average length traveled during a run $\bar{l}_{\text{run}} \sim 50$ μm. Runs end when a reorientation event called a "tumble" occurs. Tumbles are caused by one or more flagella rotating in the opposite direction, which forces the flagellar bundle to splay out and reorient the bacteria before bundling together once more and pushing the cell along another run in a random new direction. The tumbles last only ~ 0.1 s, making them effectively instantaneous compared to the duration of runs. Therefore, over large length and time scales, run-and-tumble motion can be modeled as a random walk with an active translational diffusion coefficient $D_b \sim \bar{l}^2_{\text{run}}/\bar{\tau}_{\text{run}} \sim 1000$ μm^2/s[25].

An important aspect of bacterial motion is the ability to sense and respond to chemical stimuli. While swimming in bulk liquid as described above, bacteria sense chemicals like amino acids, sugars, and oxygen. The chemicals transiently bind with cell-surface receptor complexes, triggering a network of processes within the cell that primarily modulate the frequency of tumbling events. Adjusting the tumble frequency enables bacteria to dynamically lengthen and shorten run lengths when moving toward regions of higher or lower

This chapter has been adapted from "Chemotactic migration of bacteria in porous media", by Tapomoy Bhattacharjee*, **Daniel B. Amchin***, Jenna A. Ott, Felix Kratz, and Sujit S. Datta, *Biophysical Journal* 120, 3483 (2021) *Equal contribution; "Influence of confinement on the spreading of bacterial populations", by **Daniel B. Amchin**, Jenna A. Ott, Tapomoy Bhattacharjee, and Sujit S. Datta, in press *PLoS Computational Biology*, (2022); "Chemotactic smoothing of collective migration", by Tapomoy Bhattacharjee*, **Daniel B. Amchin***, Ricard Alert*, Jenna A. Ott, and Sujit S Datta, *eLife* 11, 71226 (2022) *Equal contribution; and "Microbial mutualism generates multistable and oscillatory growth dynamics", by **Daniel B. Amchin**, Alejandro Martínez-Calvo, and Sujit S. Datta, submitted, *Biophysical Journal* (2022).

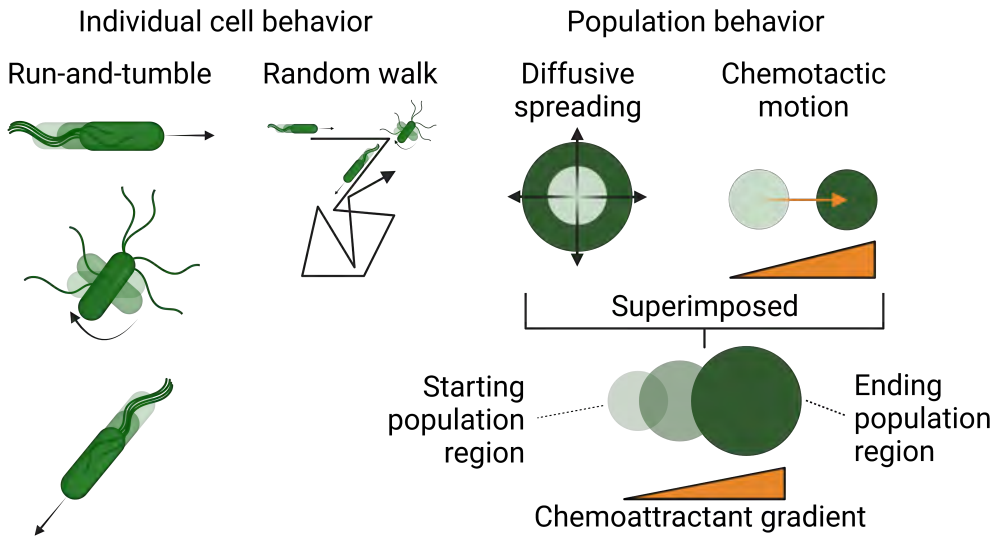

Figure 1.2: Motion of bacteria on the individual and population scales. (Left) An individual cell undergoing run-and-tumble motion is shown by the three leftmost graphics from top to bottom: a cell with bundled flagella propels forward, unbundling of the flagella reorients the cell, and re-bundling the flagella propels the cell in a new random direction. These representative components of run-and-tumble motion are shown in the context of a random walk pathway: tumbles mark the change in direction between straight line runs. (Right) Populations of bacteria undergoing run-and-tumble motion spread diffusively in all directions. Bacteria can also sense a chemoattractant gradient (orange) leading to directed motion along the gradient. The random and directed components of motion both occur simultaneously, leading to simultaneous spreading and overall population translation. Graphic created with BioRender.com.

concentration of chemoattractants, respectively. As a result, the random walk determined by run-and-tumble motion is biased[25]. The chemotactic coefficient χ describes the cell's ability to bias the random walk[26,27]. χ has the same units as the diffusion coefficient D_b; together χ and D_b describe the extent of directed and undirected motion, respectively, as shown in Fig. 1.2 for a population of cells (green circles) exposed to a nutrient gradient (orange triangle). χ specifically appears within the flux of bacteria due to chemotaxis given by bv_c, where b is the number density of cells and $v_c \equiv \chi \nabla f(c)$ is the chemotactic velocity; the function $f(c)$ describes the ability of bacteria to sense nutrient at a concentration c[28–31].

At the population scale, the process of chemotaxis can mediate directed collective mo-

tion, or migration. A striking example arises when cells consume a surrounding chemical that elicits a chemotactic response. In this case, cells collectively generate a local gradient of the surrounding attractant that they in turn bias their motion along, leading to the formation of a coherent front of cells that continually propagates[28,29,32–34]. This phenomenon can enable populations to escape from harmful environments or to colonize new terrain[28]. Chemotactic migration has therefore been extensively investigated under diverse conditions in bulk liquid[29,32,34]. Meanwhile, continuum-scale models have been developed that can successfully capture the key features of this chemotactic spreading in bulk liquids[26–29,35–37].

However, physical confinement in a tight porous medium imposes new constraints on the ability of cells to move with important consequences for how to capture their motility behavior in a model. For example, recent experiments have demonstrated that the paradigm of run-and-tumble motility does not describe isolated cells of *Escherichia coli* (*E. coli*) in a gradient-free porous medium; instead, the cells exhibit a distinct mode of motility in which they are intermittently and transiently trapped between "hops" through the pore space due to interactions with the surrounding solid matrix[38,39] (Fig. 1.3). Moreover, while cells in bulk liquid bias their motion in response to a perceived nutrient gradient primarily by modulating their reorientation frequency, experiments suggest that confinement in a tight porous medium can suppress the ability of cells to do so[38].

Indeed, studies of microswimmers that self-propel akin to bacteria suggest that collisions with the solid matrix can suppress, or even completely abolish, coordinated motion[40–43]; thus, is it unclear whether coordinated, multicellular migration can even occur in confined spaces. Nevertheless, studies in viscoelastic agar demonstrate that chemotactic migration can still arise in these complex media, although the presence of dispersed obstacles strongly

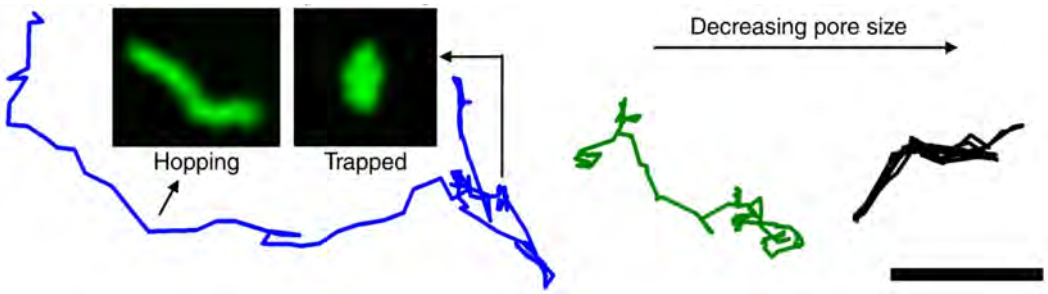

Figure 1.3: Bacteria undergoing a hop-and-trap random walk within 3D media of different pore sizes. Single-cell trajectories reveal two modes of motion: during hops, bacteria move through extended, directed paths through the pore space, and during traps, bacteria are confined for extended periods of time. Images with black backgrounds show a region of width ~ 15 μm depicting time projections of the cell body in the hopping and trapping states; trapped cells continually reorient their bodies until they escape and hop through the pore space once more. Decreasing pore size decreases hop lengths, indicated by the green and black trajectories (characteristic pore sizes are 3.6, 2.5, and 1.5 μm from left to right). Scale bar represents 10 μm. Repurposed from [38].

hinders spreading [44,45]. Thus, it remains unknown 1) how confinement modifies individual and collective bacterial motion and 2) how to model these effects.

In this dissertation, I address these gaps in knowledge by developing continuum models guided by experiments that capture collective bacterial migration under confinement. First, I describe how confinement in a porous medium strongly alters the chemotactic migration of *E. coli* through a transparent model porous medium, motivating key changes to existing continuum models to appropriately account for confinement (Chapter 2). By carefully exploring this continuum model, I then detail how increased confinement mediates a transition from chemotactic spreading of motile cells to growth-driven spreading *via* a slower, jammed front (Chapter 3).

1.2 Morphological robustness to perturbations in collective migration

In the previous subsection, I motivated my work describing how individual motion of cells is modified by confinement, giving rise to confinement-dependent properties of collec-

tive migration, as further detailed in Chapters 2 and 3. In this subsection, I will motivate my work building upon this understanding of the connection between individual and population-scale motion to elucidate a mechanism for migrating populations to withstand perturbations in overall morphology, as described further in Chapter 4.

The chemotactic migration of bacteria described in the prior subsection is an example of coordinated collective motion, a class of phenomena wherein numerous individuals organize their motion on a scale much larger than that of the individual. The flocking of birds, schooling of fish, herding of animals, and procession of human crowds are all other examples of collective migration. These phenomena also manifest more broadly at smaller scales, such as in populations of other prokaryotic and eukaryotic cells, as well as dispersions of synthetic self-propelled particles. In addition to being a fascinating example of emergent behavior, collective migration can be critically important—enabling populations to follow cues that would be undetectable to isolated individuals[46], escape from harmful conditions and colonize new terrain[28], and coexist[47]. Thus, diverse studies have sought to understand the mechanisms by which collective migration can arise.

Less well understood, however, is how collective migration persists after a population is confronted with perturbations. These can be external, stemming from heterogeneities in the environment[40–43,48–51], or internal, stemming from differences in the behavior of individuals[52–54]. Mechanisms by which such perturbations can *disrupt* collective migration are well documented. Indeed, in some cases, perturbations can abolish coordinated motion throughout the population entirely[40–43,49,50,52,53]. In other cases, perturbations couple to the active motion of the population to destabilize its leading edge, producing large-scale disruptions to its morphology[48,55–60]. Indeed, for one of the simplest cases of

collective migration—*via* chemotaxis, the biased motion of cells up a chemical gradient—morphological instabilities can occur due to the disruptive influence of hydrodynamic[61–63] or chemical-mediated[64–69] interactions between cells. By contrast, mechanisms by which migrating populations can *withstand* perturbations have scarcely been examined.

To address this gap in knowledge, I numerically solve the model developed in Chapter 2 in 2D to reveal how limitations in single-cell sensing of stimuli influence large-scale population morphology as observed experimentally (Chapter 4).

1.3 Growth of mixed microbial populations

Microbial communities often comprise different species having distinct functions, metabolic capabilities, and requirements for survival; nevertheless, they can stably coexist as a group, often in dynamic environments with strongly-fluctuating nutrient availability. How is this coexistence achieved?

As a necessary first step toward addressing this question, numerous studies have documented the varying ways in which different species in a community interact, ranging from mutually-harmful competition to mutually-beneficial cooperation. This network of interactions can give rise to fascinating emergent behaviors whose occurrence is remarkably consistent across diverse communities. For example, a common finding is that microbial communities can have *multiple stable states*, each characterized by its own unique composition of the different coexisting species, and each of which is stable under different environmental conditions[70–84]. In some cases, these states are *multistable*—i.e., multiple stable states can arise under identical conditions—leading, for example, to *hysteretic* behavior in which the state of the community depends not just on current conditions, but also on the

history of how they were established[71–73,78,85–95]. Multistability can also lead to dynamic behavior in which the community continually fluctuates between multiple states, often with periodic *oscillations*[77,82,84,88,88,96–102].

Competition for limited resources is typically inherent in multi-species communities; hence, much work has focused on understanding ways in which such behaviors can emerge in communities with purely competitive interactions[82,87,88,92–94,97,103–107]. However, a growing body of research is revealing that mutualistic interactions, such as cross-feeding of metabolites, also arise and play critical roles in many naturally-occurring microbial communities[76,80,108–133]. For example, microbial mutualism regulates the consumption of marine particulate organic matter[73,74,134,135], plant growth[136–138], how carbon and nitrogen are fixed in or released from the ground beneath our feet[139], and degradation of environmental contaminants[140]—with profound implications for biogeochemical processes in the world around us. Such interactions also play key roles in our own bodies. A prominent example is that of microbial communities in the gut, lung, and mouth, in which anaerobic bacteria can ferment large carbon-rich macromolecules that are inaccessible to nearby aerobes, releasing smaller byproducts that support the growth of the aerobes, which in turn help support anaerobic growth by consuming oxygen[71,141–144]—and collectively, such aerobe-anaerobe communities help maintain host health[145], or conversely, contribute to disease[141,146–150]. Similar mutualistic aerobe-anaerobe communities also arise and play crucial roles in many other ecological and biotechnological settings[139,151–157]. Understanding how mutualism influences the overall behavior of a microbial community is therefore both fundamentally interesting and practically important for predicting and controlling a variety of environmental, agricultural, biomedical, and industrial processes.

Given that mutualistic interactions are prevalent in microbial communities, and that such communities frequently exhibit multistability, hysteresis, and time-dependent behaviors, we asked the questions: Can mutualism generate these complex behaviors? And if so, are there simple biophysical principles that describe these behaviors and the conditions under which they arise? Prior experiments on model two-species communities of aerobes and anaerobes in bioreactors[71,72,96,158] provide useful guidance in addressing these questions. In particular, this prior work demonstrated experimentally that such communities can indeed exhibit multistability, hysteresis, and time-dependent behaviors. Moreover, it showed that many of these behaviors can be recapitulated using sophisticated models of the intricate network of metabolic interactions between cells, as reconstructed from genomic data[71,159–162]. However, such networks are made up of a multitude of vastly-differing interactions, ranging from competitive to cooperative; thus, the role played by mutualism in generating these behaviors is obfuscated, making the formulation of simple overarching biophysical principles challenging.

In Chapter 5, I address this challenge by mathematically modeling a two-species community of aerobes and anaerobes having a simplified set of mutualistic interactions between them. Specifically, inspired by the prior studies noted above, I consider the case in which the anaerobes break down non-metabolized complex carbohydrate to simple sugar that is shared by the entire community—but only under low-oxygen conditions that are established through aerobic consumption of oxygen. Remarkably, even in this highly-simplified community, I find that multistability, hysteresis, and time-dependent behaviors arise, mediated by carbon and oxygen fluxes just as in experiments. Moreover, the simplicity of the model enables me to distill out biophysical principles that quantify how oxygen depletion

and nutrient sharing jointly enable coexistence—highlighting the pivotal role of mutualism in enabling coexistence without needing to invoke antagonism. These principles quantitatively capture the conditions under which different community behaviors arise in the model, providing a foundation for future studies of more complex multi-species microbial communities in a broad range of settings.

Altogether, the work described in Chapters 2-4 provides a framework to predict and control the migration of bacteria and potentially other forms of active matter in general, in complex environments with physical confinement. Additionally, the work described in Chapter 5 provides a way to predict and control the growth behavior of more complex bacterial communities in response to nutrients. Future work could explore more sophisticated models that combine the frameworks developed in Chapters 2-5 to predict and control the behavior of bacterial communities more broadly, in environments with both physical and chemical complexities.

2

Chemotactic migration of bacteria in porous media

2.1 Introduction

As detailed in Chapter 1, current understanding of migration of bacteria is based on studies performed in bulk liquid, despite the fact that many bacteria inhabit tight porous media

such as soils, sediments, and biological gels. Thus, experiments performed by others in our lab directly visualized the chemotactic migration of *E. coli* populations in well-defined 3D porous media in the absence of any other imposed external forcing (e.g., flow). These experiments revealed that pore-scale confinement is a strong regulator of migration. Strikingly, our analysis of these data reveals that cells use a different primary mechanism to direct their motion in confinement than in bulk liquid, as detailed below. Furthermore, confinement markedly alters the dynamics and morphology of the migrating population—features that can be described by a continuum model we developed, as detailed below, but only when standard motility parameters are substantially altered from their bulk liquid values to reflect the influence of pore-scale confinement.

2.2 Results

2.2.1 Pore-scale confinement regulates, but does not abolish, chemotactic migration

Others in our lab prepare porous media by confining hydrogel particles, swollen in a defined rich liquid medium with *L*-serine as the primary nutrient and attractant at concentrations similar to those used in previous studies[28,45], at prescribed jammed packing fractions in transparent chambers. The media have three notable characteristics, as further detailed in the Materials and methods section in the online version of this work[163]. First, the pack-

This chapter has been adapted from "Chemotactic migration of bacteria in porous media", by Tapomoy Bhattacharjee*, **Daniel B. Amchin***, Jenna A. Ott, Felix Kratz, and Sujit S. Datta, *Biophysical Journal* 120, 3483 (2021) *Equal contribution. **Author Contributions:** T.B. and S.S.D. designed the experiments; T.B. performed all experiments; D.B.A., J.A.O., F.K., and S.S.D. designed the numerical simulations; D.B.A. performed all numerical simulations; T.B., D.B.A., and S.S.D. analyzed the data; S.S.D. designed and supervised the overall project. All authors discussed the results and implications and wrote the manuscript.

ings have interparticle pores that the cells swim through (Fig. 2.1A, top panel), with a mean pore size ξ that can be tuned in the range ~ 1 to 10 μm (Fig. S1 in the online version of this work[163]) —characteristic of many bacterial habitats.

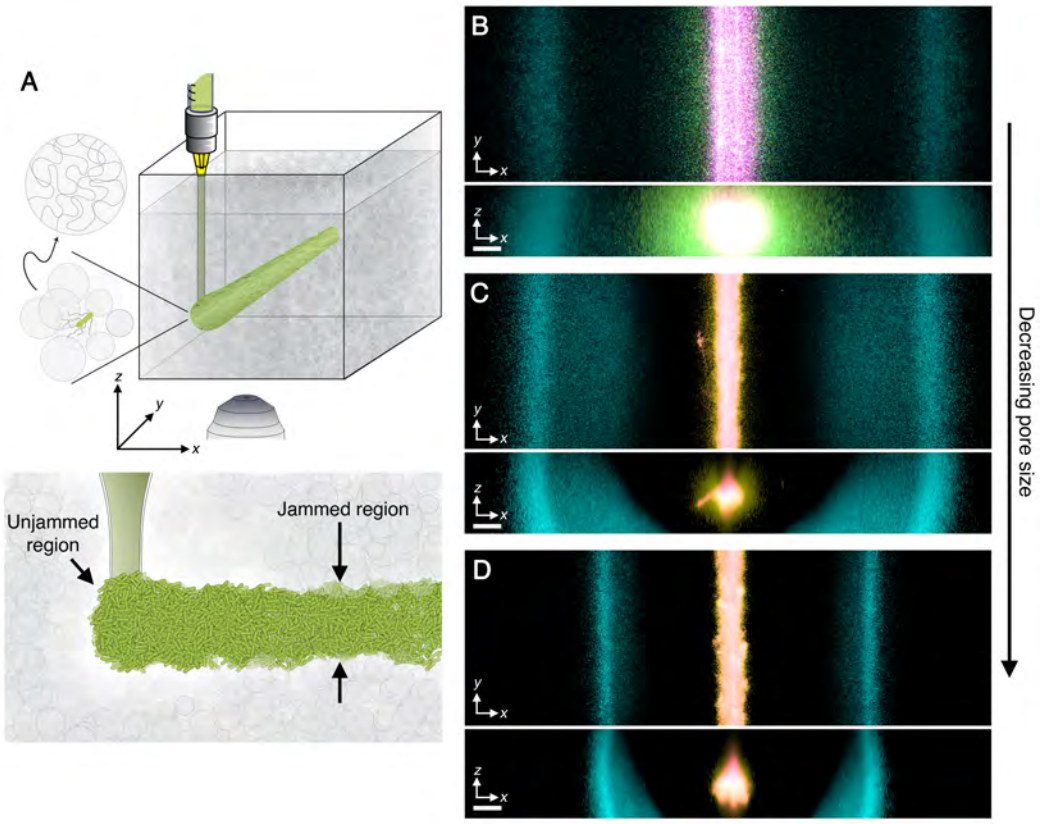

Figure 2.1: Propagating cellular fronts in porous media. (A) Schematic of a cylindrical population (green cylinder) 3D-printed within a porous medium made of jammed hydrogel particles (gray). The surrounding medium fluidizes as cells are injected into the pore space, and then rapidly re-jams around the cells, as shown in the lower schematic. Thus, the starting architecture of the 3D-printed population is defined by the path traced out by the injection nozzle. Each cylinder requires ~ 10 s to print, two orders of magnitude shorter than the duration between successive 3D confocal image stacks, ~ 10 min. (B) Top and bottom panels show bottom-up (xy plane) and end-on (xz plane) projections of cellular fluorescence intensity measured using 3D confocal image stacks. Images show a section of an initially cylindrical population at three different times (0, 1, 2.7 h shown in magenta, yellow, cyan) as it migrates radially outward in a porous medium. Panels (C–D) show the same experiment in media with smaller pores; (B), (C), (D) correspond to media with $\xi = 2.2, 1.7$, and 1.2 μm, respectively. Magenta, yellow, and cyan correspond to $0, 1.8$, and 10.3 h in (C) and $0, 1.3$, and 17.3 h in (D). All scale bars denote 200 μm; thus, a pixel corresponds to ~ 1 cell, indicating that the cells coherently propagate *via* multicellular fronts over length scales spanning thousands of cell body lengths.

The pores are sufficiently large to enable cells to swim through without deforming the medium, and thus, the packings act as rigid, static matrices. Moreover, because the hydrogel particles are highly swollen, they are freely permeable to oxygen and nutrient. As a result, the influence of geometric confinement on cellular migration can be isolated and systematically investigated without additional complications arising from the influence of confinement on the spatial distribution of nutrient. Second, the media are yield-stress solids (Fig. S1 in the online version of this work[163]) ; we can therefore use an injection nozzle mounted on a motorized translation stage to introduce cells into the pore space along a prescribed 3D path. As it moves through the medium, the nozzle locally rearranges the hydrogel packing and gently extrudes cells into the interstitial space; then, as the nozzle continues to move, the surrounding particles rapidly densify around the newly-introduced cells, re-forming a jammed solid matrix[164–166] that surrounds the population with minimal alteration to the overall pore structure[165] (Fig. 2.1A, bottom panel). This feature enables populations of bacteria to be 3D-printed in defined initial architectures within the porous media. Finally, these media are transparent, enabling tracking of fluorescent cells in 3D as they move over length scales ranging from that of single cells to that of the overall population. This platform thus overcomes three prominent limitations of common semi-solid agar assays: they do not have defined pore structures, they do not provide control over the spatial distribution of bacteria within the pore space, and their turbidity precludes high-fidelity and long-time tracking of individual cells.

To establish a defined initial condition akin to conventional agar inoculation assays, other members of our lab 3D-print a ~ 1 cm-long cylinder of densely-packed *E. coli*, constitutively expressing green fluorescent protein (GFP) throughout their cytoplasm, within a

medium with $\xi = 2.2$ μm (Fig. 2.1B, magenta). The radial symmetry simplifies analysis of how the cells subsequently move, and the cell concentrations tested mimic those in dense aggregates that frequently arise in environmental and biological settings[167–175].

After 3D-printing, the outer periphery of the population spreads slowly (Fig. 2.1B, magenta-yellow and Fig. 2.2A, magenta-green), with a radial position R_f that varies with time t as $\sim t^{1/2}$ (Fig. 2.2D, blue). Then, remarkably, this periphery spontaneously organizes into a coherent front of cells with an extended tail. This front continually propagates radially outward (Fig. 2.1B, cyan; Fig. 2.2A, blue to cyan), reaching a constant speed $v_{\mathrm{fr}} \approx$ 14 μm/min (Fig. 2.2D, blue) after an induction time $\tau^* \approx 2$ h—demonstrating that coordinated multicellular migration can indeed occur in porous media. The inner region of the population, by contrast, remains fixed at its initial position and eventually loses fluorescence (Fig. S2 in the online version of this work[163]), indicating that it is under oxygen-limited conditions.

Without nutrient, propagating fronts do not form at all, even though cells still retain motility (Fig. S3A-B in the online version of this work[163]). Additionally, reducing the concentration of cells in the initial population—which reduces the rate of overall nutrient consumption—increases the time required for front formation (Fig. S3C in the online version of this work[163]). Thus, front formation is mediated by bacterial consumption of nutrient, similar to chemotactic migration in liquid media. However, the propagation speed is over two orders of magnitude smaller than the unconfined cellular swimming speed, and over an order of magnitude smaller than the speed of unconfined fronts[29,34]: clearly pore-scale confinement regulates the dynamics of chemotactic migration.

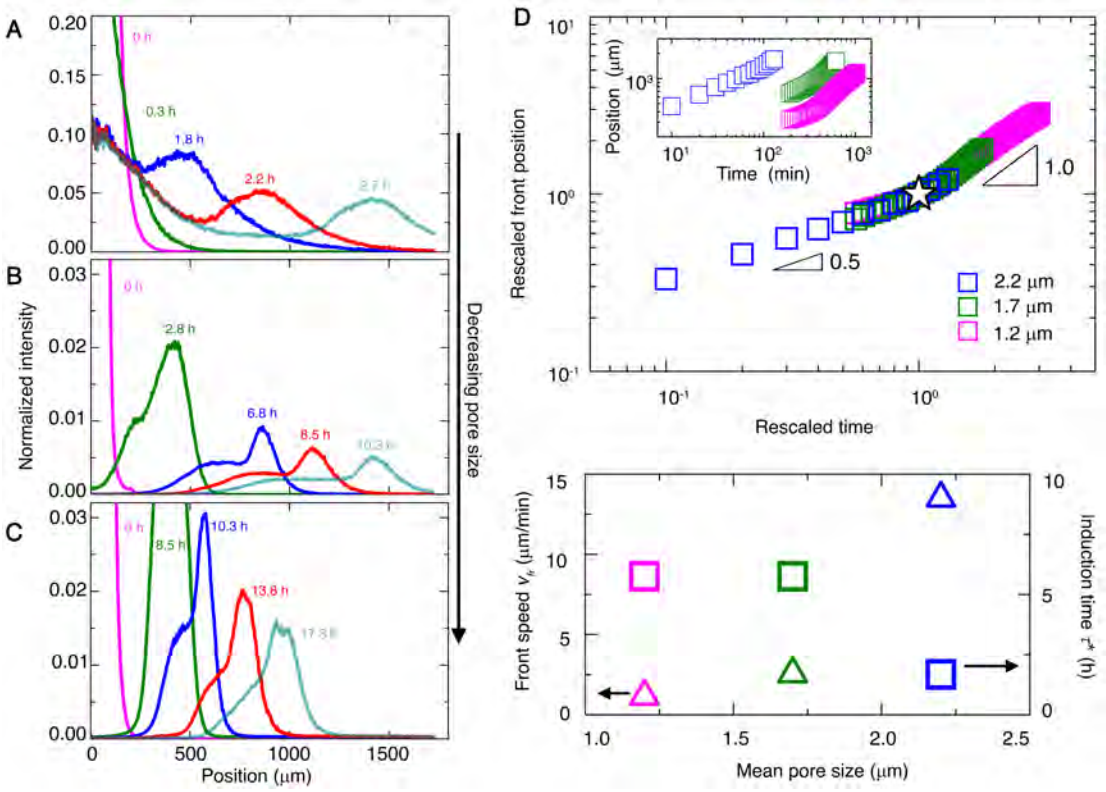

Figure 2.2: Propagation of cellular fronts is regulated by pore-scale confinement. (A–C) Azimuthally-averaged fluorescence intensity from cells obtained using 3D confocal stacks, normalized by its maximal initial value, for different radial positions and at different times. (A), (B), (C) show experiments performed in media with $\xi = 2.2, 1.7$, and 1.2 μm, respectively. In all cases, the population initially spreads outward, and then organizes into a front, indicated by the peak in the profiles, that propagates outward. (D) Upper panel shows leading-edge position R_f of the propagating front over time t; inset shows raw data, while main panel shows data rescaled by the lengths and times (star) of the deviation from the short-time slow $R_f \sim t^{1/2}$ scaling. Data for $\xi = 1.7$ and 1.2 μm begin at a later time to ensure a reliable calculation of the azimuthal average. Lower panel shows variation of front propagation speed (triangles), determined from the long-time variation of the leading-edge position, and induction time (squares), defined as the time at which the deviation from the short-time slow $R_f \sim t^{1/2}$ scaling is observed, with mean pore size. A replicate experiment for each pore size yields nearly identical results, as shown in Fig. S4 in the online version of this work[163], confirming the reproducibility of our observations. The uncertainty in front position in the top panel is determined by varying the intensity threshold value used to determine the front position by $\pm 10\%$. The uncertainty in the front speed v_{fr} is determined through the uncertainty in the linear fit of the measured position versus time data beyond the induction time τ^*; the uncertainty in τ^* itself is given by the temporal resolution of the imaging. In all cases, the error bars associated with the uncertainty in the measurements are smaller than the symbol size.

2.2.2 Individual cells bias their motion *via* a fundamentally different pri-

Although the fronts of cells continually propagate outward, the individual cells do not: single-cell tracking at the leading edge of a front reveals that the cells still continue to move in all directions (Fig. 2.3A-B). Our tracking focuses on cells at the leading edge to enable high-fidelity and long-time tracking while avoiding artifacts arising from the high cellular density in the crowded peak of the front. Moreover, it facilitates direct comparison with the macroscopic measurements shown in Fig. 2.2, which also focus on the motion of the leading edge; indeed, previous experiments performed in bulk liquid[29] have shown that the dynamics of cells at the leading edge of a chemotactic front are representative of the overall front dynamics.

Cells in the front exhibit hopping-and-trapping motility, much like isolated cells in porous media[38,39]. In particular, each cell moves along a straight path of length l_h within the pore space over a duration τ_h—a process known as hopping—until it encounters a tight spot and becomes transiently trapped. It then constantly reorients its body until it is able to unbundle its flagella after a duration τ_t, which enables it to escape and continue to hop through the pore space[38]. This mode of motility is distinct from the paradigm of run-and-tumble motility exhibited in bulk liquid; in bulk liquid, runs extend along straight-line paths ~ 40 μm long, while in a tight porous medium, a cell collides with an obstacle and becomes transiently trapped well before it completes such a run. Thus, hops are runs that are truncated by collisions with the surrounding solid matrix, with lengths that are set by the geometry of the pore space[39]. This process can be modeled as a random walk—in this case, with steps given by the hops, punctuated by pauses due to trapping (Fig. 2.3B).

How do these seemingly random motions collectively generate a directed, propagating

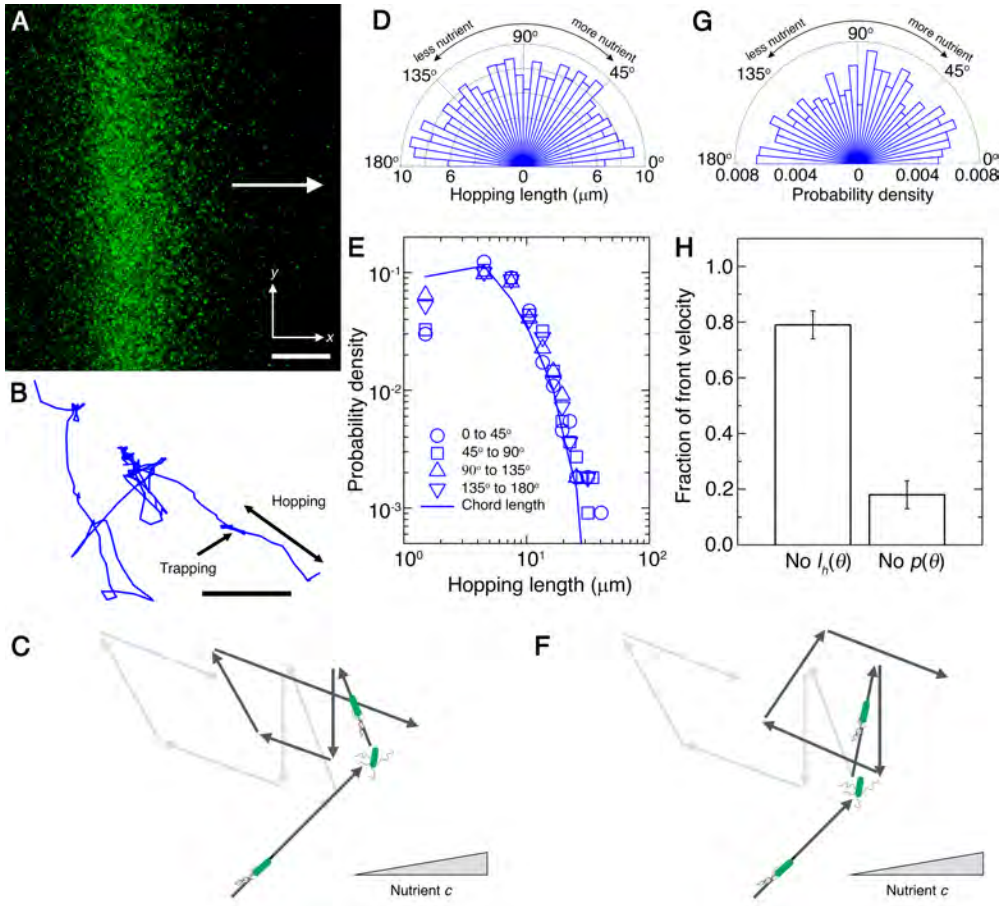

Figure 2.3: Biased motion of single cells in propagating fronts is altered by confinement. (A) Magnified bottom-up fluorescence intensity projection of a propagating front, showing individual cells. Scale bar denotes 200 μm. (B) Representative trajectory of a single cell at the leading edge of the front. Scale bar denotes 10 μm. (C) Schematic showing the primary mechanism by which cells bias their motion in bulk liquid: run length modulation. (D) Mean lengths of hops along different orientations $|\theta|$ with respect to the front propagation direction. We observe no marked directional bias. (E) Symbols show the probability density of hopping lengths along different orientations within the ranges indicated by the legend; curve shows measured chord length distribution function, which is determined by geometry, for the porous medium. The agreement between the symbols and the curve indicate that the distribution of hopping lengths is set solely by pore geometry, independent of orientation. (F) Schematic showing the primary mechanism by which cells bias their motion in porous media: hop orientation modulation. (G) Probability density of hopping along different orientations. We observe a slight directional bias: the bars are longer, indicating more hops, for orientations along the direction of front propagation, $0 \leq |\theta| \leq 90^\circ$. (H) Chemotactic migration velocity calculated using Eq. 2.1, replacing orientation-dependent hopping lengths with the mean (first bar) or replacing orientation-dependent hopping probability with a uniform distribution (second bar). Error bars show standard deviation of velocity calculated using different angle bin widths. All data are for $\xi = 2.2$ μm, from an additional replicate of the experiment presented in Fig. 2.2.

front? In bulk liquid, cells detect changes in nutrient along each run, and then primarily modulate the frequency of tumbling to bias their run length—resulting in longer runs along the direction of propagation and shorter runs in the opposite direction[23] (Fig. 2.3C). However, it is unlikely that a similar mechanism could mediate migration in porous media: cells cannot elongate their hops due to obstruction by the solid matrix, nor can they shorten hops because confinement by the matrix suppresses the flagellar unbundling required to stop mid-hop[38]. Single-cell tracking confirms this expectation: the mean hopping lengths $\bar{l}_h$ measured for hops along a given orientation θ relative to the direction of front propagation show no marked directional bias (Fig. 2.3D). The distribution of hopping lengths is instead set by pore geometry, independent of θ, as quantified by the chord length distribution—the probability that a straight chord of a given length l_c fits inside the pore space (Fig. 2.3E). Hence, another mechanism must be at play.

Another mechanism also arises, albeit weakly, for chemotactic migration in bulk liquid: cells modulate the number of flagella that unbundle, and thus the degree to which their bodies reorient, during tumbling to bias the orientation of their next run[40,176–178] (Fig. 2.3F). However, this mechanism only accounts for $\sim 30\%$ of the overall speed of front propagation in bulk liquid, with run length anisotropy accounting for $\sim 70\%$[34]. Hence, why *E. coli* also employ this secondary mechanism during chemotaxis has remained a puzzle thus far.

Given that cells cannot appreciably bias their hop lengths in a porous medium, we conjecture that this putatively secondary mechanism—biasing hopping orientation—is the primary driver of chemotactic migration in porous media. In this mechanism, cells detect local changes in nutrient, which arise due to consumption by the entire population, along

each hop. The cells then modulate their reorientation during trapping to bias the direction of their next hop along the nutrient gradient. Indeed, 90% of measured trapping events are shorter than 4 s (Fig. S5 in the online version of this work[163]) the mean duration over which *E. coli* "remember" exposure to nutrient[179], suggesting that this mechanism is plausible.

To directly test this hypothesis, we use our single-cell tracking to examine the probability of hopping along a given orientation, $p(\theta)$. Consistent with our expectation, we find that hops along the direction of front propagation ($0 \leq |\theta| < 90°$ in Fig. 2.3G) are slightly more frequent than hops in the opposite direction ($90 < |\theta| \leq 180°$). To quantify the relative importance of this bias in the hopping orientation, we use these data to directly compute the chemotactic migration velocity

$$v = \int_{0°}^{360°} \frac{p(\theta)\bar{l}_{\mathrm{h}}(\theta)\cos\theta}{\bar{\tau}_{\mathrm{h}} + \bar{\tau}_{\mathrm{t}}} d\theta \tag{2.1}$$

Replacing $\bar{l}_{\mathrm{h}}(\theta)$ by its orientation-averaged value only changes v by $\approx 20\%$ (first bar in Fig. 2.3H)—confirming that biasing hopping length is not the primary mediator of chemotaxis, in stark contrast to the case of bulk liquid. Strikingly, however, replacing $p(\theta)$ by a uniform distribution decreases v precipitously, by over 80% (second bar in Fig. 2.3H)—confirming that biasing hopping orientation is the primary driver of chemotactic migration in porous media.

To further explore the influence of pore-scale confinement, we repeat our experiments in two additional media having even smaller mean pore sizes, 1.7 and 1.2 μm. We again observe two regimes of expansion in time, with initial slow spreading followed by motion with

$R_f \sim t$ (Fig. 2.1C-D; Fig. 2.2B-C; Fig. 2.2D, green and magenta). Confinement is again a key regulator of these dynamics. With increasing confinement, the induction time increases while the front propagation speed considerably decreases (Fig. 2.2D, lower panel). The morphology of the front itself is also strongly altered by confinement: both the maximal cell density within the front, and the width of its tail, decrease with increasing confinement (Fig. 2.2B–C). Single-cell tracking again reveals that cells migrate by biasing hopping orientation—not by biasing hopping length, as is generally assumed, and that this bias consistently represents the primary contribution to the chemotactic migration velocity (Figs. 2.4–2.5). These effects are all missed by models of chemotactic migration in bulk liquid, in which front dynamics are determined solely by the intrinsic ability of cells to alter and respond to their chemical environment, without considering physical constraints imposed by the environment[26]. Other models consider environmental constraints by treating cellular motility parameters as fitting parameters or assuming their values using idealized models[45,180–182]. By contrast, our experiments provide a direct way to assess how current models can be extended and applied to describe chemotactic migration in tight porous media, as detailed below.

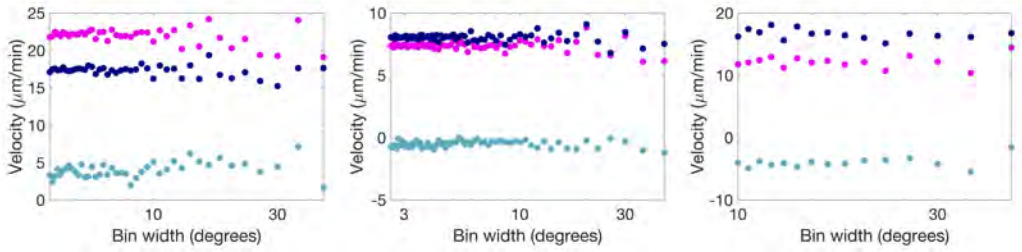

Figure 2.4: Bias in hopping orientation is the primary contributor to chemotactic migration. Plots show migration velocity calculated using the discrete sum version of Eq. 2.1, as described in the Methods subsection "Connecting single-cell motility to front propagation" in §2.4.1, incorporating all factors (magenta), replacing orientation-dependent hopping lengths with the mean (dark blue) or replacing orientation-dependent hopping probability with a uniform distribution (teal). From left to right, data for the largest, intermediate, and smallest pore sizes are shown for different choices of the bin width, showing that the result reported in Fig. 2.3 is not sensitive to the choice of bin width. The data show that removing the bias in hopping orientation makes the largest difference in the calculated migration velocity for all pore sizes—that is, the bias in hopping orientation is the primary contributor to chemotactic migration.

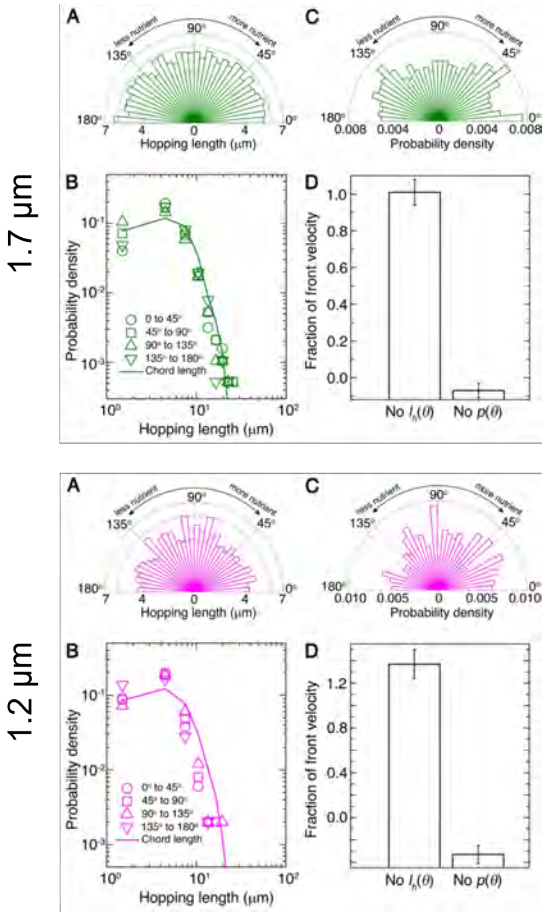

Figure 2.5: Biased motion of single cells in medium- and small-pore media. (A) Mean lengths of hops along different orientations $|\theta|$ with respect to the propagation direction. (B) Symbols show probability density of hopping lengths along different orientations within the ranges indicated by the legend; curve shows measured chord length distribution function for the porous medium. (C) Probability density of hopping along different orientations. We consistently observe a slight directional bias: the bars are longer, indicating more hops, for orientations along the direction of front propagation, $0 \leq |\theta| \leq 90°$. In particular, 51.6% and 52.2% of hops have an angle between $[0, 90°)$ while only 48.1% and 46.9% have an angle between $(90°, 180°]$ in media with $\xi = 1.7$ and 1.2 μm, respectively; the remaining 0.3% and 0.9%, respectively, occur at $90°$. (D) Chemotactic migration velocity calculated using Eq. 2.1, replacing orientation-dependent hopping lengths with the mean (first bar) or replacing orientation-dependent hopping probability with a uniform distribution (second bar). The second bar is slightly negative, indicating that measured hop lengths are on average slightly larger opposite the propagation direction–likely due to limited statistics. That front propagation would halt entirely or reverse without a bias in hopping orientation demonstrates that this bias is the primary driver of chemotactic migration. Error bars show standard deviation of velocity calculated using different angle bin widths.

2.2.3 A continuum description of chemotactic migration requires motility parameters to be strongly altered

Our experiments reveal a clear separation of length and time scales between the biased random walks of individual cells (Fig. 2.3A–B) and the directed propagation of the overall front over large length and time scales (Figs. 2.1–2.2)—hinting that the macroscopic features of front propagation can be captured using a continuum description. Thus, we test whether front dynamics can be described using the classic Keller-Segel model, which is conventionally applied to chemotactic migration in bulk liquid or viscoelastic media[26,28,29,34,45]. Specifically, we model the evolution of the nutrient concentration $c(r,t)$ and number density of bacteria $b(r,t)$ *via* the coupled equations:

$$\frac{\partial c}{\partial t} = D_c \nabla^2 c - b\kappa g(c) \tag{2.2}$$

$$\frac{\partial b}{\partial t} = D_b \nabla^2 b - \chi_0 \nabla \cdot [b \nabla f(c)] + b\gamma g(c) \tag{2.3}$$

as detailed in §2.4.2. Equation 2.2 relates the change in c to nutrient diffusion through the medium and consumption by the population; D_c is the nutrient diffusivity, κ is the maximal consumption rate per cell, and $g(c) = c/(c + c_{\text{char}})$ describes the influence of nutrient availability relative to the characteristic concentration c_{char} through Michaelis-Menten kinetics. Equation 2.3 in turn relates the change in b to undirected hopping-and-trapping

with diffusivity D_b, biased hopping with the chemotactic coefficient χ_0 and nutrient sensing function $f(c) = \log\left[(1 + c/c_-) \,/\, (1 + c/c_+)\right]$, where c_- and c_+ quantify the range of cellular sensing, and net growth with maximal rate γ. Hence, this model relies on two standard quantities to describe the motion of the population over large length and time scales: the diffusivity D_b, which characterizes undirected spreading, and the chemotactic coefficient χ_0, which characterizes the ability of cells to bias their motion in response to a sensed nutrient gradient. In bulk liquid, their values simply depend on intrinsic cellular processes: D_b is determined by the run speed and tumbling frequency[23], while χ_0 additionally depends on properties of cellular chemoreceptors and signal transduction[26]. In porous media, however, confinement inhibits the ability of cells to move; it is therefore unclear whether the Keller-Segel model can describe front propagation in these more complex settings, and if so, how it must be modified.

To answer these questions, we numerically solve Eqs. 2.2-2.3 using values for all parameters estimated from direct measurements, as detailed in §2.4.2 and §2.4.3—except χ_0, which we obtain by directly matching the asymptotic front propagation speed measured in our experiments. Importantly, we obtain D_b from direct measurements of bacterial hopping lengths and trapping durations as previously established[38], instead of treating it as an additional free parameter or assuming its value using idealized models as is often done[45,180–182]. Furthermore, to facilitate comparison to the experiments, we determine the cellular signal—the analog of the experimentally-measured fluorescence intensity in the numerical simulations—by incorporating the fluorescence loss observed in the experiments under starvation conditions. Finally, because confinement increases the local density of cells in the pore space, increasing the propensity of neighboring cells to collide as they

hop through the pore space, we explicitly account for possible cell-cell collisions that truncate both D_b and χ_0 at sufficiently large values of b. Indeed, the porous media are highly confining, with pore size is always < 8 μm (Fig. S1 in the online version of this work[163]), comparable to the size of a single cell body and its flagella. Thus, because the pore space is too small to fit multiple cells side-by-side, we expect that cell-cell interactions are necessarily restricted to end-on interactions. This feature of confinement in a tight porous medium is starkly different from the case of cells in bulk liquid, in which short-range side-by-side interactions promote alignment of cell clusters and result in cooperative motions at high cell densities. Single-cell imaging of cell-cell interactions in the pore space confirms this expectation, indicating that cell-cell collisions truncate the hopping lengths of moving cells (Movies S8 and S9 in the online version of this work[163]). Motivated by this observation, we adopt a simplified mean-field treatment of cell-cell interactions in which cells truncate each other's hops in a density dependent manner. Because both motility parameters D_b and χ_0 reflect the ability of cells to move through the pore space *via* a biased random walk with a characteristic step length l, we expect that they vary as $\propto l^2$, with l set by the mean chord length $\bar{l}_c$ in the absence of collisions. However, when the cell density is sufficiently large, the mean distance between neighboring cells, $\bar{l}_{cell}$, decreases below $\bar{l}_c$; in this case, motivated by the experimental observations, we expect that cell-cell collisions truncate l to $\approx \bar{l}_{cell}$. Therefore, wherever $0 \leq \bar{l}_{cell} < \bar{l}_c$, we multiply both the density-independent parameters D_b and χ_0 by the density-dependent correction factor $(\bar{l}_{cell}/\bar{l}_c)^2$. In this treatment, as the cellular density increases, and thus the mean spacing between cells decreases, they increasingly truncate each other's motion and the motility parameters D_b and χ_0 decrease – eventually becoming zero when the cells are so dense that they do not have space to move.

In this manner, we make the diffusivity and chemotactic parameters functions of cell density. The full details of the form of $D_b(b)$ and $\chi(b)$ are given in §3.2.3 and Eqs. 3.5, 3.6, and 3.7.

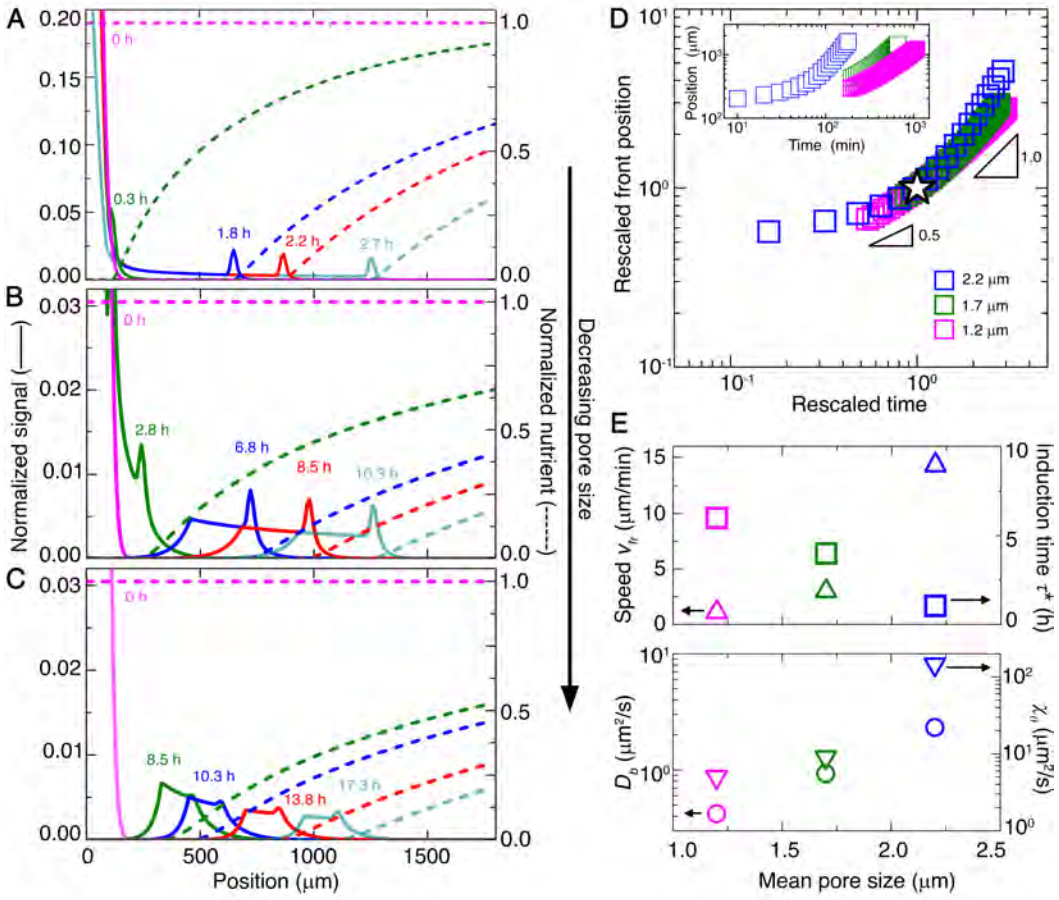

Figure 2.6: Continuum model captures dynamics of propagating cellular fronts in porous media. (A-C) Numerical simulations of cellular signal (solid lines) and nutrient concentration (dashed lines), normalized by maximal initial value, for different radial positions and at different times. Top to bottom panels show results for media with $\xi = 2.2, 1.7$, and 1.2 μm, respectively. In all cases, the population initially spreads outward, and then organizes into a front, indicated by the peak in the profiles, that propagates outward, as in the experiments. (D) Leading-edge position R_f of the propagating front over time t; inset shows raw data, while main panel shows data rescaled by the lengths and times (star) of the crossover from the short-time slow $R_f \sim t^{1/2}$ scaling to the long-time fast $R_f \sim t^1$ scaling. We observe slight deviations from the $R_f \sim t$ scaling for the $\xi = 2.2$ μm data at long times; these reflect the influence of boundaries in the system, as indicated by additional simulations (Fig. 2.7). (E) Upper panel shows variation of front propagation speed (upward triangles), determined from the long-time variation of the leading-edge position, and induction time (squares), defined as the time at which the crossover from the short-time slow $R_f \sim t^{1/2}$ scaling to the long-time fast $R_f \sim t^1$ scaling is observed, with mean pore size, as determined from the simulations. Lower panel shows variation of cellular diffusivity (circles), which is directly obtained from experiments, and chemotactic coefficient (downward triangles), which is determined from the simulations, with mean pore size. The uncertainty in front position in the top panel is determined by varying the threshold value used to determine the front position by $\pm 10\%$. The uncertainty in the front speed $v_{\rm fr}$ is determined by computing the standard deviation in the $v_{\rm fr}$ obtained by measuring the slope of the measured position versus time data for three successive 30 min periods at the end of the simulation, while the uncertainty in τ^* is again given by the temporal resolution of the simulation. In all cases, the error bars associated with the uncertainty in the measurements are smaller than the symbol size.

This model indeed yields fronts of cells that form and propagate outward (solid curves in Fig. 2.6A-C), driven by their self-generated nutrient gradient (dashed curves); in the absence of growth, fronts still form and propagate, but their motion is hindered in a confinement-dependent manner (Fig. 2.7).

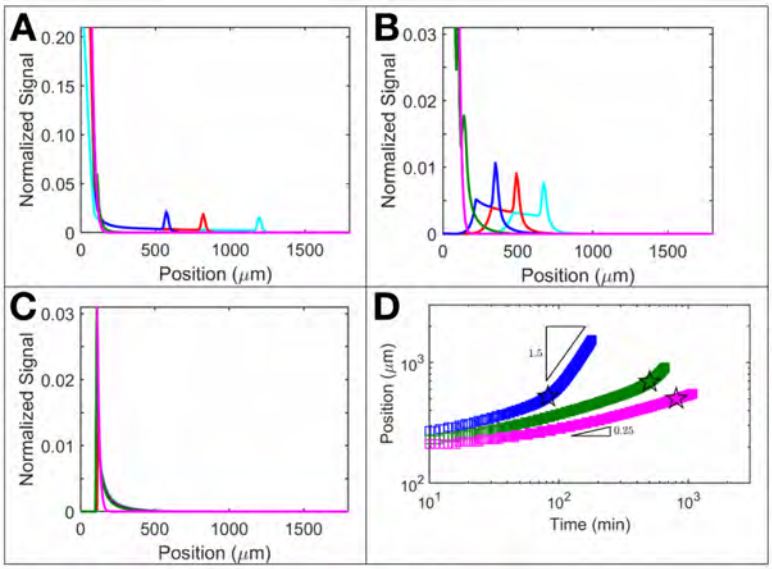

Figure 2.7: In the absence of growth, fronts still form and propagate, but are hindered in a confinement-dependent manner. Additional simulations of chemotactic migration without bacterial growth; panels A-C correspond to the same simulations as in Fig. 2.6A-C, but with $\gamma = 0$; colors correspond to the same times as in Fig. 2.6A-C. In the media with largest pores (A), front propagation appears to be similar to the case of non-zero growth, indicating that chemotaxis plays a dominant role in driving front propagation in these media; compare panel A to Fig. 2.6A. In the media with intermediate sized pores (B), front propagation is slower without growth; compare panel B to Fig. 2.6B. In the media with smallest pores (C), propagating fronts do not appreciably form over the simulation time scale, indicating that growth plays a dominant role in driving front propagation in these media; compare panel C to Fig. 2.6C. The resultant dynamics of the position of the leading edge of the front are shown in (D).

The numerical solutions thus obtained capture the main features observed in the experiments: for all three pore sizes, the population first spreads slowly, driven by the initially steep gradient in bacterial density, and then transitions to motion with $R_f \sim t$ (Fig. 2.6D; Fig. 2.8) once this gradient has smoothed out (Fig. 2.9). Moreover, with increasing confinement, the induction time increases, while the front speed, the maximal cell density, and the width of the tail all decrease considerably (Fig. 2.6A-C, E)—consistent with the experimental results. As expected, the dynamics and morphologies of the fronts depend strongly on the motility parameters D_b and χ_0. However, unlike the case of bulk liquid, for which these parameters are set solely by intrinsic cellular processes, in tight porous media, confinement reduces these parameters by up to three orders of magnitude (Fig. 2.6E, bottom panel)[28,29]. Furthermore, confinement-induced cell-cell collisions play a key role in regulating chemotactic migration: when the influence of crowding-induced collisions is not accounted for, the simulated fronts do not exhibit the transition to motion with $R_f \sim t$ observed in the experiments for any of the media tested, nor do they have the same shapes as those seen in the experiments (Fig. 2.8). Together, these results indicate that the Keller-Segel model can indeed describe front propagation in porous media at the continuum scale, but only when the motility parameters are substantially altered in a confinement-dependent manner.

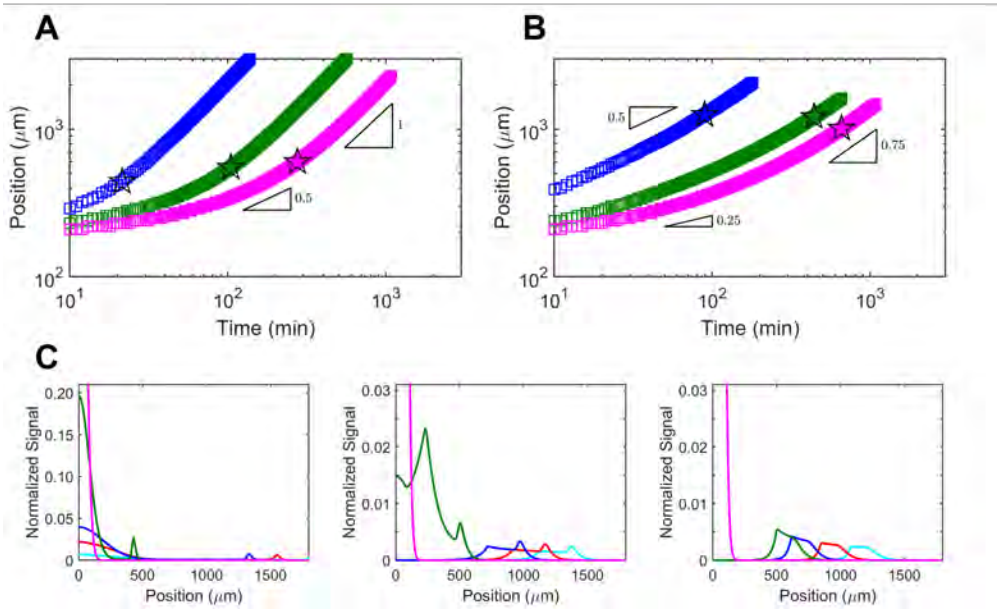

Figure 2.8: Further simulations of front propagation. (A) Front propagation in rectilinear coordinates. Leading-edge position R_f motion of the propagating front over time t for simulations performed in rectilinear coordinates; colors correspond to those in Fig. 2.6. Stars indicate the crossover from slower to faster $R_f \sim t$ motion. In this case, we observe closer agreement to the crossover from slower to faster $R_f \sim t$ motion observed in the experiments than simulations performed in cylindrical coordinates. We conjecture that this agreement reflects the influence of boundaries in the experiment: while the experiments initially have cylindrical symmetry, with the initial 3D-printed cylinder placed far from all boundaries, as fronts propagate, they begin to approach the bottom boundary of the imaging chamber. Specifically, the simulations indicate that the region of nutrient depletion reaches the bottom boundary after ~ 0.5-1 h; in this case, the symmetry of the fronts is no longer cylindrical in the experiments, but has a rectilinear component. (B) Without collisions, simulations do not exhibit the transition to $R_f \sim t$ motion observed in the experiments. To assess the importance of cell-cell collisions in the model, we perform the same simulations as in Fig. 2.6, but without the corrections to the motility parameters that incorporate cell-cell collisions; colors correspond to those in Fig. 2.6. We fit the chemotactic parameter such that the speed over the last 30 minutes of the simulation matches the experiment, similar to our method for the other simulations in this chapter, except here we impose no effects of cell-cell collisions. The values of chemotactic parameter obtained are 10, 0.9, and 0 $\mu m^2/s$ for the pore sizes in decreasing order, notably smaller than the values obtained by considering collisions. Moreover, none of the simulations achieve ballistic scaling in the absence of collisions. We note that for the case of $\chi_0 = 0$ $\mu m^2/s$, propagating fronts still occur—in this case, however, driven by cellular growth. In particular, nutrient diffusing inward to the leading edge of the population enables continual growth, driving outward spreading. (C) Profiles of simulated cellular signal, normalized by maximal initial value, for different radial positions and at different times, for simulations in panel B. Left to right panels show results for media with $\xi = 2.2, 1.7$, and 1.2 μm, respectively; colors show different times as indicated in Fig. 2.6. Without cell-cell collisions, the simulated front profiles have different shapes from the experiments. In particular, the peak heights are further reduced, and for the smallest pore size, the peak of the front is not at its leading edge but rather is toward the back — again highlighting that cell-cell collisions arising from crowding are necessary for an improved agreement with the experiments.

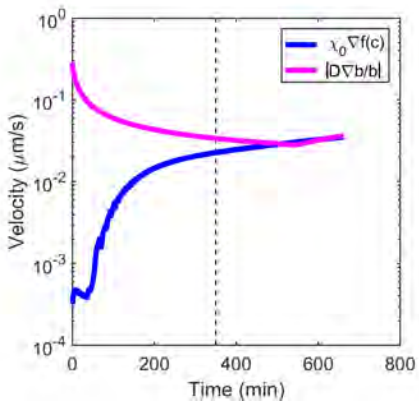

Figure 2.9: Simulations shed light on the physics underlying the observed transition in front dynamics. An example for the case of intermediate pore-size media shows the variation of the maximum local chemotactic velocity (blue) and maximum local diffusive velocity (magenta) over time. At early times, the cell gradient is steep due to the sharp boundary of cells in the initial geometry of the population. This steep cell gradient drives diffusive flux, but decreases with time, as shown by the magenta curve. Meanwhile, chemotaxis begins low because (i) consumption must first reduce nutrient to within sensing levels and (ii) collisions halt the chemotactic response of cells within the dense starting region. Then, as the population spreads out, the chemotactic flux increases, and at the induction time (dashed line), the two velocities become comparable and eventually reach a steady state. We note that the diffusive process considered here is not thermal diffusion—which our previous experiments using non-motile cells established to be negligible for these conditions[38]—but is active diffusion arising from the random walks performed by motile cells as they "hop" through the pore space, punctuated by transient "traps".

2.2.4 Continuum model describes long-range sensing by bacterial populations

Why can bacteria coordinate their migration in porous media, while many other microswimmers seemingly cannot? These classes of microswimmers rely on short-range interactions to coordinate their motion [183]. By contrast, chemotactic migration relies on the coupling between a population-generated nutrient gradient—which extends over long distances spanning hundreds of cell lengths (dashed curves, Fig. 2.6A-C)—and biased cellular motion along this gradient. Hence, solely through nutrient consumption, different bacteria can collectively influence and coordinate each other's motion across long distances—even when strongly confined. For example, when the separation between two populations is smaller than the length scale ≈ 500 μm over which nutrient is depleted, they "smell" each other, and fronts only propagate away from, not toward, each other in both simulations and experiments (Fig. 2.10A-B, top row). By contrast, when the separation is much larger, fronts propagate both toward and away from each other (bottom row). Thus, the framework developed here provides principles to both predict and *direct* chemotactic migration.

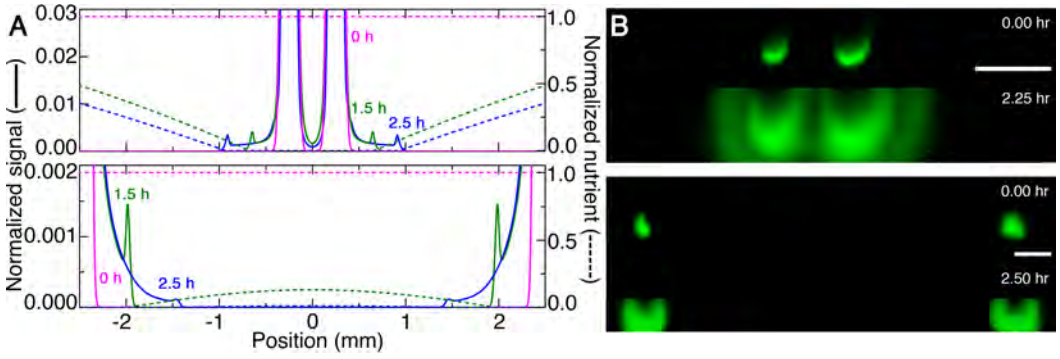

Figure 2.10: Nutrient depletion directs front propagation over long ranges. (A) Numerical simulations and (B) end-on (xz) fluorescence intensity projections for experiments showing front propagation from two initially cylindrical populations with axes separated by 500 μm (upper row) or 5 mm (lower row). Cells diffuse, but fronts do not propagate between the closely-separated cylinders, as shown by the cell-depleted region between the two at all times; by contrast, fronts do propagate between the further-separated cylinders. Scale bars denote 500 μm.

2.3 Conclusion

Studies of motility are typically performed in bulk liquid—even dating back to the discovery of bacteria, "all alive in a little drop of water", in 1676. However, many bacteria inhabit tight and tortuous porous media. Our work demonstrates that chemotactic migration can be fundamentally different in porous media than in bulk liquid. The paradigm of *E. coli* chemotaxis is that individual cells bias their motion primarily by modulating the frequency of reorientations, possibly with a small additional contribution due to biased reorientation amplitude. Why cells also employ this second mechanism has remained a puzzle thus far. Through direct tracking of cells performing chemotactic migration, our experiments reveal that this second mechanism can, in fact, be the primary driver of chemotaxis in tight porous media. Thus, cells employ different mechanisms that enable them to bias their motion and forage for nutrients in different environments[178]—motivating future studies of motility in a variety of complex settings.

Our experiments also provide a direct test of the applicability of the classic Keller-Segel model in describing chemotactic migration in highly-confining porous media. While this continuum model is broadly used for migration in bulk liquid or viscoelastic media[28,29,34,45], whether it provides a suitable description of migration in tight spaces has thus far remained unknown. Consequently, applications either utilize the Keller-Segel model[26,45,180,182] by treating both motility parameters D_b and χ_0 as fitting parameters, estimating them using *ad hoc* approximations, or instead turn to agent-based models that explicitly simulate the different cells, which provides tremendous insight but does not provide a continuum description[184]. The comparison between our experiments and simulations demonstrates that

the Keller-Segel model indeed describes chemotactic migration in porous media, but only when two modifications are incorporated: (i) the cell density-independent motility parameters are reduced by several orders of magnitude from values obtained using conventional liquid assays, reflecting the hindered motion of individual cells in the tight pore space, and (ii) these motility parameters are further corrected to incorporate the influence of density-dependent cell-cell collisions, which arise more frequently in a tight pore space. Thus, pore-scale confinement is a key factor that regulates chemotactic migration, and should not be overlooked. Indeed, because the framework developed here describes migration over large length and time scales, we expect it could help more accurately describe the dynamics of bacteria in processes ranging from infections, drug delivery, agriculture, and bioremediation. Furthermore, many other active systems—ranging from other prokaryotes, cancer cells, white blood cells, amoeba, enzymes, chemically-sensitive colloidal microswimmers, and chemical robots[185–191]—also exhibit chemotaxis, frequently in complex environments and following similar rules as *E. coli*. Thus, the principles established here could be used more broadly to describe collective migration for diverse forms of active matter.

Our extension of the Keller-Segel model represents a key first step toward describing the full spatiotemporal features of chemotactic migration at the continuum scale, capturing the transition from slow to faster motion, as well as the variation of the induction time, the front speed, the maximal cell density in the front, and the width of the tail of the front with pore size observed in the experiments. However, we observe slight differences in the dynamics of the leading edge and in the shapes of the simulated fronts than those observed experimentally. These may reflect the mean-field treatment of cell-cell collisions in the model, which simplifies the details of these collisions and does not treat more sophisticated

collective dynamics that arise at high local cell densities in bulk liquid[192–196]. Developing a more detailed treatment of these dynamics in porous media will be a useful direction for future work. Furthermore, because our hydrogel porous media are permeable to oxygen and nutrient—similar to many biological gels, as well as many microporous clays and soils—they enable us to isolate the impact of geometric confinement on cellular migration. However, many other porous media are composed of solid matrices that are impermeable to oxygen and nutrient, resulting in more complex spatial profiles of nutrient that may also alter how cells bias their motion. Moreover, these settings often have fluid flow, which can further alter oxygen, nutrient, and cellular profiles in interesting ways. Exploring the added influence of such complexities will be an interesting extension of our work.

2.4 Methods

2.4.1 Imaging and analysis of cell motion

Analysis of cell motion in propagating fronts

After the 3D printed populations form propagating fronts, we image the motion of individual cells at the leading edge of the front. We chose to analyze cells at the leading edge of the front to facilitate comparison with the macroscopic measurements, which also track the leading edge of the front (as shown in Fig. 2.2). Indeed, studies in bulk liquid[29] show that the local chemotactic drift of individual cells at the leading edge matches well with the drift velocity of most of the entire front and the overall propagation speed of the entire front. Thus, chemotaxis of cells at the leading edge of the front is likely to be most representative of the overall behavior of the front. However, quantifying any systematic variation of

bacterial dynamics with position in the front would be an interesting direction for future work.

Other members of our lab acquire successive fluorescence micrographs from a slice of thickness 79 μm every 51 ms, and track between 171 and 282 cells inside each porous medium for a minimum of 5 s. Other members of our lab differentiate between hopping and trapping using an instantaneous speed threshold of 12 μm/s. To quantify possible directional biases, only the hopping and trapping events longer than three time points (153 ms) are included in the analysis. The angle, θ, between the direction of front propagation and the hopping direction is measured as $\theta \equiv \tan^{-1}[\vec{v}_f \times \vec{v}_b / \vec{v}_f \cdot \vec{v}_b]$ where $\vec{v}_f$ is the vector direction of front propagation and $\vec{v}_b$ is the vector connecting the start and end point of a hop.

Connecting single-cell motility to front propagation

Our single-cell imaging reveals that bacteria in a propagating front exhibit hopping-and-trapping motility, much like isolated cells in gradient-free porous media. Treating this process as a random walk then yields the chemotactic migration velocity v given by Eq. 2.1; θ represents the hopping angle with respect to the direction of macroscopic front propagation and thus $l_\mathrm{h}\cos\theta$ represents the projected length of a hop.

Specifically, each hop identified using imaging of single cells at the leading edge of the front yields a measurement of θ, $l_\mathrm{h}(\theta)$, and τ_h, while each trapping event yields a measurement of τ_t. We directly calculate $p(\theta)$ using all measurements of θ, and we calculate $\bar{\tau}_\mathrm{h}$ and $\bar{\tau}_\mathrm{t}$ by averaging over all hopping and trapping measurements. We calculate $\bar{l}_\mathrm{h}(\theta)$ by averaging the measured l_h over all hops having θ within a bin spanning $(\theta - \delta\theta, \theta + \delta\theta)$. Then,

we calculate v as a discrete sum: $v = \int_{0^\circ}^{360^\circ} \frac{p(\theta)\bar{l}_\mathrm{h}(\theta)\cos\theta}{\bar{\tau}_\mathrm{h}+\bar{\tau}_\mathrm{t}} d\theta = \sum_{\theta_i} \frac{p(\theta_i)\bar{l}_\mathrm{h}(\theta_i)}{\bar{\tau}_\mathrm{h}+\bar{\tau}_\mathrm{t}} \frac{\sin(\theta_i+\delta\theta)-\sin(\theta_i-\delta\theta)}{2\delta\theta}$ where the sum is over all bins $(\theta_i - \delta\theta, \theta_i + \delta\theta)$ and $p(\theta_i) \equiv \int_{\theta_i-\delta\theta}^{\theta_i+\delta\theta} p(\theta_i) d\theta_i$ represents the fraction of all hops having orientations within a specified bin. To ensure our choice of bin width $2\delta\theta$ has no effect on the results, we vary the bin width from 45 degrees to the smallest value for which each bin contains at least 20 data points, corresponding to 4, 2.61, and 10 degrees for the media with mean pore size 2.2, 1.7, and 1.2 μm, respectively. The velocity results for different bin widths are shown in Fig. 2.4. The calculated velocity overshoots the actual front velocity due to limitations in tracking very long trap times, thus artificially lowering the average trap time in the discrete sum and raising the velocity. However, these plots demonstrate that the order of the three conditions tested—uniform $p(\theta)$, uniform $\bar{l}_\mathrm{h}$, or both $p(\theta)$ and $\bar{l}_\mathrm{h}$ being θ-dependent—is consistent across all bin widths. The variation in velocity for different bin widths is reported in the standard deviation shown in the bar charts of Fig. 2.3. Replacing $p(\theta)$ by a uniform distribution decreases v precipitously, confirming that biasing hopping orientation—presumably by modulating the number of flagella that unbundle during trapping, and thus the amplitude of cell body reorientation, as has been analyzed previously[34,167–169]—is the primary driver of chemotactic migration in porous media. The results thus obtained are not sensitive to the presence of hops spanning the boundary of the field of view; removing hops beginning in a buffer region $\bar{l}_\mathrm{h}$ wide on all boundaries, yet keeping hops that end in this region, still yields similar results to those presented here. A similar analysis performed for cells at varying positions throughout the front will be an interesting direction for future work; our analysis only focuses on cells at the leading edge of the front to facilitate comparison with the macroscopic tracking of the leading edge shown in Fig. 2.2. Furthermore, as suggested by others for experiments in bulk

media[29], the local chemotactic drift of individual cells near the leading edge matches well with the drift velocity of most of the entire front and indeed, the overall speed of the entire front.

2.4.2 Formulation of continuum model

To mathematically model front propagation, we build on previous work[26–29,34–37,197–199] to describe the evolution of the nutrient concentration $c(r,t)$ and number density of bacteria $b(r,t)$ *via* Eqs. 2.2-2.3. The continuum model, which is conventionally applied to chemotactic migration in bulk liquid or viscoelastic media, relies on two standard quantities to describe the motion of the population over large length and time scales: the diffusivity, which characterizes undirected spreading, and the chemotactic coefficient, which characterizes the ability of cells to bias their motion in response to a sensed nutrient gradient. Our single-cell tracking in the absence of a nutrient gradient provides a direct determination of the diffusivity, which we then use directly as an input to the model. Our single-cell tracking at the leading edge of the chemotactic front also demonstrates the importance of cellular reorientation bias in driving chemotaxis; however, the single-cell data do not yield a direct determination of the chemotactic coefficient, because this quantity also depends on properties of cellular chemoreceptors and signal transduction, as well as the exact nutrient conditions, all of which are unknown. Therefore, as is conventionally done, we determine this parameter by directly fitting the long-time speed predicted by the continuum model to the experimentally-determined front speed. The continuum model does not explicitly incorporate the exact mechanism by which cells bias their motion; it simply requires a bias in cellular motion, as confirmed by the single-cell tracking.

Choice of $c(r, t)$

The medium contains 10 mM *L*-serine as the most abundant nutrient source and attractant[200]. Moreover, *E. coli* consume *L*-serine first in mixed media[31] and are known to respond most strongly to serine as a chemoattractant compared to other components of the media we use[33,201–204] as well as compared to oxygen[203]. Thus, unlike other work exploring mixtures of different nutrients and attractants[28], in our experiments *L*-serine acts as the primary nutrient source and attractant. When the primary nutrient and primary attractant are different chemical species, metabolically active cells continue to grow and divide in the wake of the propagating front[28]—unlike in our experiments, for which the inner region of the population remains fixed and eventually loses fluorescence, indicating that it is under nutrient-limited conditions[199]. We therefore focus on *L*-serine in the continuum model, represented by the concentration field $c(r, t)$.

We note that while *L*-serine can exhibit toxicity at high concentrations[205], consumption by the cells reduces the local nutrient levels by over one to two orders of magnitude within the propagating fronts themselves (indicated in Fig. 2.6A-C); thus, we do not expect or see any indication of possible toxicity of *L*-serine in the experiments.

Our numerical simulations focus on the nutrient concentration $c(r, t)$; however, incorporating oxygen concentration as an additional field variable, initially at 250 μM throughout[206], that diffuses[207] with diffusivity 2500 $\mu m^2/s$ and is consumed by the bacteria at a maximal rate of 1.2×10^{-12} $mM(cell/mL)^{-1}s^{-1}$ and with a characteristic Michaelis-Menten level[29] of 1 μM reveals that the oxygen profile is remarkably similar to that of the nutrient (Movie S15 in the online version of this work[163]) : oxygen becomes depleted in the same region as the nutrient, consistent with the idea that the front contains aerobically metaboli-

cally active cells while behind the front cells are deprived of both nutrient and oxygen.

We note that the nutrient levels of our liquid medium are nearly two orders of magnitude larger than the levels under which *E. coli* excrete appreciable amounts of their own chemoattractant[208]. Moreover, chemoattractant excretion results in the collapse of cells into pointlike aggregates[208–210], which are not observed in our experiments. Thus, under the nutrient-rich conditions explored in our work, it is unlikely that bacteria in the front excrete appreciable levels of their own chemoattractant.

For all of these reasons, our model incorporates a single nutrient and attractant through the field $c(r, t)$ for simplicity.

Nutrient diffusion

Molecules of *L*-serine (size $\sim$ 1 nm) are nearly two orders of magnitude smaller than the hydrogel particle mesh size $\sim$ 40-100 nm. Moreover, the *L*-serine isoelectric point is 5.7, lower than our pH of 7.4, and the polymers making up the hydrogel are negatively charged under our experimental conditions; we therefore do not expect that attractive electrostatic interactions or complexation arise. Thus, we do not expect that steric or electrostatic interactions with the hydrogel matrix impede *L*-serine diffusion, and we take the nutrient diffusivity D_c to be equal to its previously measured value in pure liquid, 800 $\mu m^2/s$.

Nutrient consumption

The total rate of nutrient consumption is given by $b\kappa g(c)$, where κ is the maximum consumption rate per cell and $g(c) = c/(c + c_{\text{char}})$ describes the influence of nutrient availability through Michaelis-Menten kinetics i.e. it quantifies the reduction in consumption

rate when nutrient is sparse as established previously[28,45,211–213], with $c_{\text{char}} = 1$ μM as determined previously[214]. We use a value of $\kappa = 1.6 \times 10^{-11}$ mM(cell/mL)$^{-1}$s^{-1} comparable to values determined previously[45] that yields values of v_{fr} that match the experimental values and yields front peak heights that match experimental values of the cellular signal. These are the values of c_{char} and κ used in Chapters 2 and 4, although in Chapter 3 we present an improved method of extracting these values from the experimental profile of a traveling front directly (§3.2.6) that yields better agreement in profile width, in particular.

Cellular diffusivity

Porous confinement alters both the undirected and directed components of cell motion. Our previous work[38] showed that isolated cells move in an undirected manner *via* hopping-and-trapping motility, with a cellular diffusivity D_b that characterizes motion over time scales much larger than $\tau_{\text{t}} \sim$ 1-10 s. To determine D_b for each porous medium, we use experimental measurements of the hopping lengths l_{h} and trapping durations τ_{t} of isolated cells in gradient-free conditions in each porous medium, and calculate $D_b \approx 0.3 \times \bar{l}_{\text{h}}^2/3\bar{\tau}_{\text{t}}$, where the factor of 0.3 is an empirical correction determined previously[38]. We finally obtain $D_b = 2.32$, 0.93, and 0.42 μm^2/s for porous media with $\xi = 2.2$, 1.7, and 1.2 μm, respectively.

Cellular chemotaxis

We employ an advective term $-\nabla \cdot (bv_{\text{c}})$ to describe biased motion along a chemoattractant gradient, where the chemotactic velocity $v_{\text{c}} \equiv \chi_0 \nabla f(c)$ quantifies the abilities of individual cells to logarithmically respond to the local nutrient gradient. Specifically, the

function $f(c) = \log\left[(1 + c/c_-) \,/\, (1 + c/c_+)\right]$ established previously[28] quantifies the ability of the cells to sense nutrient levels[215–221], where $c_- = 1$ μM and $c_+ = 30$ μM are the upper and lower bounds of logarithmic sensing, and the chemotactic coefficient χ_0 quantifies the ability of bacteria to bias motion in response to the sensed nutrient gradient. Although heterogeneity in χ_0 may be present within the population[29], we focus our analysis on the effect of pore size by assuming all individual bacteria have identical chemotactic capabilities. Since our experiments demonstrate that the ability to bias motion is dependent on pore-scale confinement, we use χ_0 as the pore size-dependent fitting parameter. We vary χ_0 to match the numerically-simulated long-time front speed with that of the experiment. We finally obtain $\chi_0 = 145$, 9, and 5 μm^2/s for porous media with $\xi = 2.2$, 1.7, and 1.2 μm, respectively.

Cell growth

To obtain the cell doubling time τ_2, we measure the first division time for isolated cells within a gradient-free small-pore medium that inhibits cellular motion. Specifically, we measure the duration between the first cell division and the second cell division for 13 cells to find the average cell division time to be $\tau_2 = 60$ minutes. The rate at which cells grow is then given by $b\gamma g(c)$, where $\gamma = \ln(2)/\tau_2$ is the maximal doubling rate per cell and $g(c)$ again describes describes the influence of nutrient availability through Michaelis-Menten kinetics i.e. it quantifies the reduction in growth rate when nutrient is sparse. Because c and b are coupled in our model, we do not require an additional "carrying capacity" of the population to be included, as is often done[28,45]: we track nutrient deprivation directly through the radially-symmetric nutrient field $c(r, t)$.

Loss of cellular signal

We experimentally observe that while the periphery of a 3D-printed population forms a propagating front, the inner region remains fixed and eventually loses fluorescence, indicating that it is under nutrient-limited conditions. Specifically, the fluorescence intensity of this fixed inner population remains constant for $\tau_{\text{delay}} = 2$ h, and then exponentially decreases with a decay time scale $\tau_{\text{starve}} = 29.7$ min (Fig. S2 in the online version of this work[163]). We incorporate this feature in our numerical simulations to determine the cellular signal, the analog of measured fluorescence intensity in the numerical simulations. Specifically, wherever $c(r', t')$ drops below a threshold value, for times $t > t' + \tau_{\text{delay}}$, we multiply the cellular density $b(r', t)$ by $e^{-(t-t')/\tau_{\text{starve}}}$, where t' is the time at which the position r' became nutrient-depleted. This calculation yields the cellular signal plotted in Figs. 2.6–2.10, for which delayed fluorescence loss yields the ziggurat-like shape of the propagating front.

2.4.3 Implementation of numerical simulations

To numerically solve the continuum model, we use an Adams-Bashforth-Moulton predictor corrector method where the order of the predictor and corrector are 3 and 2, respectively. Since the predictor corrector method requires past time points to inform future steps, the starting time points must be found with another method; we choose the Shanks starter of order 6 as described previously[222,223]. For the first and second derivatives in space, we use finite difference equations with central difference forms. Time steps of the simulations are 0.01 s and spatial resolution is 10 μm. Because the experimental chambers are 3.5 cm in diameter, we use a radial distance of 1.75×10^4 μm for the size of the entire simulated

system.

To match the symmetry of a single 3D printed cylinder, we use a one-dimensional axisymmetric coordinate system with variation in the radial coordinate. To simulate two 3D printed lines (Fig. 2.10), we instead use a one-dimensional Cartesian coordinate system ("slab" geometry) that avoids the unnecessary use of two spatial coordinates while still demonstrating the key features of the experiment. No flux boundary conditions are used for symmetry in the center and at the walls of the simulated region for both field variables b and c.

The initial cylindrical distribution of cells 3D-printed in the experiments has a diameter of 100 ± 10 μm; so, in the numerical simulations, we use a Gaussian with a 100 μm full width at half maximum for the initial bacteria distribution $b(r, t = 0)$, with a peak value that matches the 3D-printed cell density in the experiments, 0.95×10^{12} cells/mL. The initial condition of nutrient is 10 mM everywhere, characteristic of the liquid media used in the experiments. The initial nutrient concentration is likely lower within the population initially due to nutrient consumption during the 3D printing process; however, we find negligible effects of this initial condition on the characteristics of front propagation.

To assess convergence of the numerical solutions, we perform simulations with varying spatial and temporal resolution. Even for the case of the largest pore size medium, which has the largest value of χ_0/D_b and thus requires the finest resolution, we find the long-time front speed obtained with spatial resolution of 10 μm is within $\sim 14\%$ that obtained with a resolution of 5 μm—in close agreement—and the bacterial profiles $b(r, t)$ have similar characteristics. For the intermediate pore size medium, we find that the long-time front speed obtained with spatial resolution of 10 μm and temporal resolution of 0.01 s is within $\sim$

5% the value obtained with spatial resolution of 5 μm and temporal resolution of 0.001 s, and the bacterial profiles $b(r,t)$ have similar characteristics (Fig. 2.11), confirming that the resolution is sufficiently fine so that our results are not sensitive to the choice of resolution.

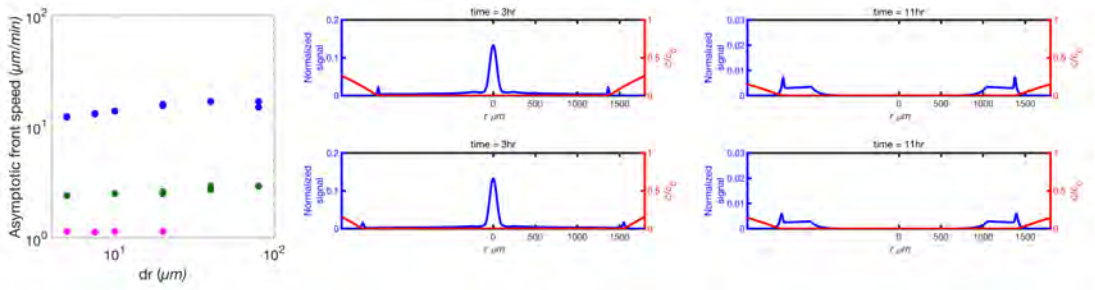

Figure 2.11: Choice of discretization in numerical simulations does not influence results. (Left panel) Long-time front speed for simulations representing chemotactic migration in porous media with $\xi = 2.2$, 1.7, and 1.2 μm (blue, green, magenta, respectively). We use two values of temporal discretization dt for each value of spatial discretization dr to ensure a sufficient time resolution was chosen; top and bottom rows show $dr = 5$ and 10 μm and $dt = 0.001$ and 0.01 s, respectively. Simulations showing normalized cell signal (blue) and normalized nutrient concentration (red) for $\xi = 2.2$ and 1.7 μm (middle and right panels, respectively) show minimal variation between choices of discretization indicated.

2.4.4 Comparison between simulations and experiments

The goal of our modeling is to identify the essential physics needed to extend the classic Keller-Segel model to the case of complex porous media, with minimal alteration to the input parameters. We therefore do not expect perfect quantitative agreement between the experiments and simulations. Instead, we hope that our work will motivate future extensions of the model that provide an even better match to the experiments, as further detailed below.

Overall, we find good agreement between the simulations and experiments. Specifically, in all cases we observe a comparable crossover from slower to faster motion, with comparable induction times, front speeds, and front peak heights, indicating that our simplified

extension of the Keller-Segel model provides an essential first step toward capturing the dynamics of chemotactic migration in porous media at the continuum scale. However, we do observe discrepancies between the model and the experiments. These discrepancies likely reflect (i) the influence of boundaries in the experiments, (ii) the simplified treatment of cell-cell collisions, (iii) differences in the values of the exact parameters input to the simulations, as detailed further below.

(i) The influence of boundaries in the experiments. While the experiments initially have cylindrical symmetry, with the initial 3D-printed cylinder placed far from all boundaries, as fronts propagate, they begin to approach the bottom boundary of the imaging chamber. Specifically, the simulations indicate that the region of nutrient depletion reaches the bottom boundary after $\sim$ 0.5-1 h for experiments in the largest pore size media; in this case, the symmetry of the fronts is no longer cylindrical in the experiments, but has a rectilinear component. We conjecture that this feature gives rise to the deviation in the long-time scaling in the simulations performed for the largest pore size media, indicated by the blue squares in Fig. 2.6D. To test this conjecture, we have repeated the simulations, but in rectilinear coordinates; the leading-edge position of the propagating front over time for simulations performed in rectilinear coordinates is shown in the top panel of Fig. 2.8; colors correspond to those in Fig. 2.6. Stars indicate the crossover from slower to faster motion. In this case, we observe closer agreement to the scaling $R_f \sim t$ observed in the experiments than simulations performed in cylindrical coordinates, confirming our conjecture.

(ii) The simplified treatment of cell-cell collisions. Because confinement increases the local density of cells in the pore space—increasing the propensity of neighboring cells to collide as they hop through the pore space—in the model, we explicitly account for possi-

ble cell-cell collisions that truncate both motility parameters at sufficiently large values of the cell density. We do this using a mean-field treatment, in which both motility parameters are truncated by a density-dependent geometric correction factor. A key finding of our work is that incorporating cell-cell collisions is essential in the model; neglecting them entirely, as is conventionally done, yields fronts that do not achieve the measured $R_f \sim t$ scaling for any of the porous media tested and have shapes that differ from those seen in the experiments (as shown in Fig. 2.8B–C). However, this mean-field treatment simplifies the details of these collisions, assuming that they simply truncate hops and do not alter trapping, and also does not treat more sophisticated collective dynamics that arise at high local cell densities in bulk liquid, such as swarming. Developing a more detailed treatment of these dynamics in porous media will be a useful direction for future work.

(iii) Differences in the values of the exact parameters input to the simulations. While our simulations use values for all input parameters estimated from our and others' direct measurements, the values used may not exactly match those corresponding to the experiments, given the uncertainty inherent in determining these parameters (e.g., the maximal nutrient consumption rate, the characteristic nutrient level in the Michaelis-Menten function). Thus, the simulations may not perfectly reproduce the experiments. For simplicity, we fix the values of these parameters using previous measurements and focus instead on the variation of the motility parameters with pore size. We anticipate that our findings will help to motivate future work that better constrains the values of the input parameters to the Keller-Segel model.

3

Influence of confinement on the spreading of bacterial populations

3.1 Introduction

As detailed in Chapter 2, we developed an extended version of the classic Keller-Segel model to explain our experimental observations of chemotactic migration through a porous medium.

In this Chapter, we explore this model in greater depth. The novelty of the model is in describing bacterial spreading *via* both motility and growth, and explicitly incorporating the influence of confinement on spreading by considering both cell-solid and cell-cell collisions. We identify key dimensionless parameters emerging from this extended model that describe bacterial spreading. Furthermore, by numerically solving the model, we show how confinement fundamentally alters the dynamics and morphology of spreading bacterial populations. In particular, with increasing confinement, we find that cell-cell collisions increasingly hinder the initial formation and the long-time propagation speed of chemotactic pulses. (In this chapter, we use the word "pulse" to distinguish peaked profiles from those without a clear peak.) Moreover, also with increasing confinement, growth plays an increasingly dominant role in driving population spreading compared to cellular motility—eventually leading to a transition from chemotactic spreading to growth-driven spreading *via* a slower, jammed front. Thus, our work provides a foundation for future investigations of the influence of confinement, and yields quantitative principles that could guide the prediction and control of bacterial spreading in crowded and complex environments.

This chapter has been adapted from "Influence of confinement on the spreading of bacterial populations", by **Daniel B. Amchin**, Jenna A. Ott, Tapomoy Bhattacharjee, and Sujit S. Datta, in press *PLoS Computational Biology*, (2022). **Author Contributions:** D.B.A. and S.S.D. developed the theory, assisted by discussions with T.B.; D.B.A., J.A.O., and S.S.D. designed the numerical simulations; D.B.A. performed all numerical simulations with assistance from J.A.O.; D.B.A. and S.S.D. analyzed the data; S.S.D. designed and supervised the overall project. D.B.A. and S.S.D. discussed the results and implications and wrote the manuscript.

3.2 Methods

3.2.1 Classic Keller-Segel model, also incorporating growth

Two forms of the Keller-Segel model have been explored in the prior literature to describe two distinct biophysical processes: one describes cellular aggregation and pattern formation in response to chemoattractant produced by the cells themselves[208,209,224], while the other describes cellular spreading in response to an exogenous chemoattractant that is not produced, but just consumed, by the cells[26–29,35–37]. Here, we focus on the latter case. Before considering confinement, we first describe how chemotactic spreading is typically modeled using this form of the classic one-dimensional Keller–Segel model—which does not incorporate the influences of growth and confinement, but can successfully capture the key features of experiments on dilute populations of bacteria in bulk liquid[26–29,34–37,45]. We also introduce growth into this model.

To directly connect the model to many experiments[29,32,45,163], we consider a sole nutrient that also acts as the chemoattractant—as is conventionally done[26,27,32]—represented by the continuum variable $c(x,t)$, where x is the position coordinate and t is time. The number density of bacteria, in turn, is given by the continuum variable $b(x,t)$. Furthermore, given the experimental conditions, we assume that the cells do not excrete their own chemoattractant or other diffusible signals, as is sometimes the case in low-nutrient conditions and for specific strains. Recent extensions of this model have also considered the case in which nutrient and attractant are separate chemical species, which leads to fundamentally different behavior that would be interesting to explore using our framework in future work[28,225].

As the nutrient diffuses through space with thermal diffusivity D_c, it is consumed by

the cells at a rate $b\kappa g(c)$; here, κ is the maximum consumption rate per cell and the Monod function $g(c) \equiv c/(c + c_{\text{char}})$, with the characteristic concentration c_{char}, quantifies the reduction in consumption rate when nutrient is sparse[28,45,211–214,226]. Therefore, the nutrient dynamics are given by

$$\frac{\partial c}{\partial t} = D_c \nabla^2 c \; - \; b\kappa g(c). \tag{3.1}$$

The bacterial dynamics have two contributions: a motility-driven flux $\vec{J}_m$ and cellular proliferation. The flux arises from the combination of the undirected spreading of cells, a diffusive process with an active diffusivity D_{b0}[23], and directed chemotaxis with a drift velocity $\vec{v}_c \equiv \chi_0 \nabla f(c)$ that quantifies the ability of the bacteria to logarithmically respond to the local nutrient gradient[27,35,36]. The well-established function $f(c) \equiv \log[(1 + c/c_-)/(1 + c/c_+)]$ quantifies the ability of the cells to sense nutrient with characteristic bounds c_- and c_+[28–31,215–221], while the chemotactic coefficient χ_0 quantifies the ability of the cells to bias their motion in response to a sensed nutrient gradient. Therefore, the motility-driven flux $\vec{J}_m = -D_{b0} \nabla b + b v_c$. Proliferation, on the other hand, is given by $b\gamma g(c)$, where γ is the maximal growth rate per cell and $g(c)$ reflects the reduction in growth rate when nutrient is sparse—circumventing the need to introduce an *ad hoc* "carrying capacity" of a logistically-growing population, as is sometimes done. Therefore, the bacterial dynamics are given by

$$\frac{\partial b}{\partial t} = \underbrace{D_{b0} \nabla^2 b - \nabla \cdot (b v_c)}_{-\nabla \cdot \vec{J}_m} + b\gamma g(c). \tag{3.2}$$

Together, Equations 3.1–3.2 represent the classic Keller-Segel model that describes the

coupled dynamics of nutrient and bacteria, also including the added influence of cellular growth. In particular, they successfully capture the key features of chemotactic spreading in unconfined liquid, in which cells collectively generate a local gradient of nutrient that they in turn bias their motion along—leading to the formation of a coherent pulse of bacteria that continually propagates, sustained by its continued consumption of the surrounding attractant[29,32–34].

3.2.2 Characteristic dimensionless parameters

Non-dimensionalizing Equations 3.1–3.2 yields useful dimensionless parameters for characterizing population spreading. We rescale $\{c, b, t, x\}$ by the characteristic quantities $\{c_\infty, b_0, t_{c,0}, \zeta\}$, where c_∞ is the initial nutrient concentration taken to be constant everywhere, b_0 is the maximal initial cell density, $t_{c,0} \equiv c_\infty / (b_0 \kappa)$ is a characteristic time scale of nutrient consumption, and $\zeta_0 \equiv \sqrt{D_{b0} t_{c,0}}$ is the characteristic extent of cellular diffusion over the duration $t_{c,0}$. This process yields the non-dimensional equations

$$\frac{\partial \tilde{c}}{\partial \tilde{t}} = \delta_0 \tilde{\nabla}^2 \tilde{c} \; - \tilde{b}\tilde{g} \tag{3.3}$$

$$\frac{\partial \tilde{b}}{\partial \tilde{t}} = \tilde{\nabla}^2 \tilde{b} \; - \alpha_0 \tilde{\nabla} \cdot (\tilde{b} \tilde{\nabla} \tilde{f}) \; + \beta_0 \tilde{b} \tilde{g}, \tag{3.4}$$

where the tildes indicate non-dimensionalized variables. Three dimensionless parameters emerge:

- The diffusion parameter $\delta_0 \equiv D_c / D_{b0}$ compares the thermal diffusion of nutrient

to the active diffusion of bacteria. When $\delta_0 \ll 1$, variations in nutrient are localized to the leading edge of the bacterial population, whereas when $\delta_0 \gg 1$, nutrient levels vary over large spatial extents.

- The directedness parameter $\alpha_0 \equiv \chi_0 / D_{b0}$ compares the influence of chemotaxis to active diffusion in driving cellular spreading. When $\alpha_0 \ll 1$, diffusion dominates and cells do not appreciably direct their motion in response to a nutrient gradient, whereas when $\alpha_0 \gg 1$, motile cells strongly direct their motion in response to a gradient.

- The yield parameter $\beta_0 \equiv \gamma / (b_0 \kappa / c_\infty)$ compares the rates of cell growth and nutrient consumption, γ and $t_{c,0}^{-1}$, respectively. It therefore quantifies the yield of new cells produced as a population consumes nutrient. When $\beta_0 \ll 1$, nutrient consumption is much faster than proliferation, whereas when $\beta_0 \gg 1$, many new cells are produced in the time required to consume the available nutrient.

The quantity $\Lambda_0 \equiv \alpha_0 / (\beta_0 \delta_0) = \gamma^{-1} \cdot \chi_0 / (D_c t_{c,0})$ therefore characterizes the interplay between chemotatic and growth-driven spreading of bacterial populations. In particular, $\left[\chi_0 / (D_c t_{c,0})\right]^{-1}$ is a characteristic time scale needed to spread *via* chemotaxis over the nutrient diffusion length $\sqrt{D_c t_{c,0}}$, while γ^{-1} is the time scale over which cells grow. Previous studies in bulk liquid focused solely on chemotactic spreading, which is characterized by the limit $\Lambda_0 \gg 1$[27,29,34,36,37]. Other studies of non-chemotactic cells focused solely on growth-driven spreading, characterized by the opposite limit $\Lambda_0 = 0$[227–232]. However, experiments performed in semi-solid agar[45] as well as in defined packings of particles[163] indicate that confinement in such crowded media introduces new cell-cell and cell-medium in-

teractions that are not incorporated in the classic Keller-Segel model. Hence, in this paper, we describe a first step toward incorporating these complexities, which not only tune Λ_0 over a broad range, but also fundamentally alter spreading dynamics—as described hereafter.

3.2.3 Keller-Segel model incorporating confinement

As a model system, we consider bacterial populations confined in media with close-packed, rigid, and immovable obstacles surrounding a free space that is sufficiently large for cells to move through. This form of confinement alters bacterial spreading dynamics in three ways:

(i) Collisions with the surroundings impede cellular spreading[38,39,233,234], reducing the transport parameters D_{b0} and χ_0, as quantified in recent experiments in 3D porous media[38,163] as well as in semi-solid agar[45];

(ii) The presence of surrounding obstacles reduces the free space available to cells to move through, increasing cellular crowding and promoting cell-cell collisions that further truncate the motility parameters, observed experimentally using *in situ* microscopy[163];

(iii) When the number density of cells is sufficiently high, this reduction in free space causes the cells to be jammed; hence, they are able to spread only through proliferation, which pushes cells outward, as quantified in experiments using single cell visualization[235,236].

Notably, (ii)-(iii) are absent from the classic Keller-Segel model, which treats cells as non-contacting, and require modifications beyond simply changing the transport parameters

D_{b0} and χ_0.

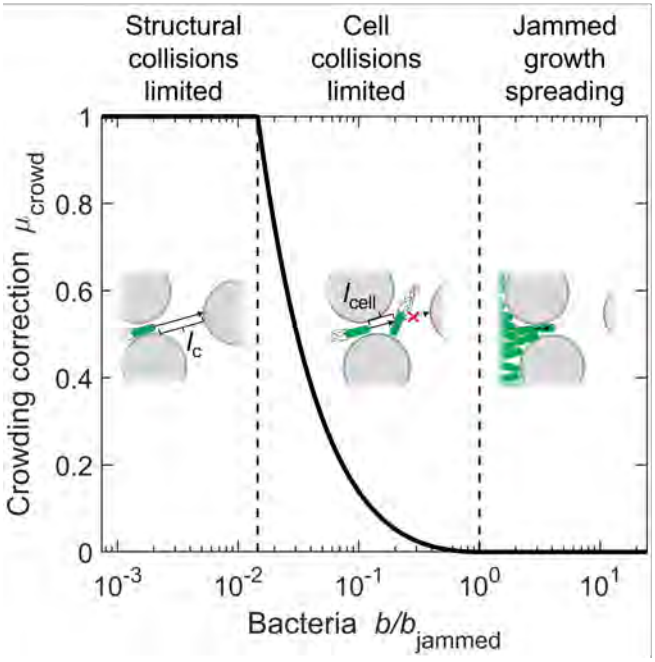

Figure 3.1: Summary of the cell density-dependent crowding correction μ_{crowd}, which we use in the model to incorporate the influence of confinement on cell-cell collisions. In particular, the cellular transport parameters are multiplied by μ_{crowd}, this case shown for the prototypical case of intermediate confinement. (Left) At low densities, spreading of cells (green) is impeded only by collisions with surrounding solid obstacles (grey), not with neighboring cells, so $\mu_{\text{crowd}} = 1$. This impeded spreading is quantified by the transport parameters D_{b0} and χ_0, whose values are regulated by the characteristic chord length $\bar{l}_c$ characterizing the amount of free space between obstacles. (Middle) When the local density of cells is so large that the characteristic separation between neighboring cells $\bar{l}_{\text{cell}}$ is less than the characteristic chord length $\bar{l}_c$, cell-cell collisions further truncate the transport parameters. This effect is quantified by $\mu_{\text{crowd}} < 1$. (Right) At the maximal density $b = b_{\text{jammed}}$, the cells are jammed and have no free space to move. Therefore, $\mu_{\text{crowd}} = 0$, and the population spreads solely through growth and division of cells. Note that our definition of the number density of bacteria b is as the number of cells per unit total volume of space, which includes the volume of surrounding obstacles.

(i) *Impeded spreading of isolated cells.* Bacterial spreading is typically modeled as a random walk with directed steps of characteristic length l and characteristic duration τ that are punctuated by reorientation events[23]. Consequently, both transport parameters D_{b0}, which describes the unbiased component of the random walk, and χ_0, which describes

the biased component, are set by $\sim l^2/\tau$. In bulk liquid, the directed steps are known as *runs*, which extend along straight-line paths $l \sim 50$ μm long, punctuated by rapid *tumbles*. In tight confinement, however, a cell collides with an obstacle and becomes transiently trapped well before it completes such a run. Therefore, as established in recent experiments [38,39], runs are truncated by collisions with surrounding obstacles, and the directed steps of the random walk are instead set by the geometry of the available free space; thus, for isolated cells, $l \sim \bar{l}_c$, the mean length of straight line *chords* [2,37] that fit in the free space [39]. Moreover, because the trapping process induced by collisions with obstacles occurs over a duration τ_t that is longer than that of the truncated runs, $\tau \approx \tau_t$. As a result, for cells confined in tight media, both transport parameters D_{b0} and χ_0 are instead $\propto \bar{l}_c^2/\tau_t$—and because increasing confinement both decreases $\bar{l}_c$ and increases τ_t [39], it concomitantly decreases both D_{b0} and χ_0, as confirmed experimentally [16,3]. Within the context of prior work investigating diffusion in porous media [2,38], we note that while the volume fraction of free space (porosity) φ is known to influence diffusion, it alone does not determine the diffusion coefficient because the geometry of the free space plays a key role as well. Thus, in our model, φ influences cellular transport (active diffusion and chemotaxis) indirectly through its effect on the chord length $\bar{l}_c$, which characterizes the length scale associated with straight paths that fit within the free space—and therefore determines the length scale over which cells can move in a directed manner.

(ii) *Crowding-induced collisions between cells*. Confinement also reduces the free space available to cells. Our definition of the number density of bacteria b quantifies the number of cells per unit total volume of space, which includes the volume of surrounding obstacles; hence, the local density of cells is given by b/φ, where $\varphi < 1$ is the volume fraction of free

space that is reduced by the presence of obstacles. This increase in the local density of cells increases the propensity of neighboring cells to collide as they move, further truncating l. Single-cell imaging in a porous medium confirms this expectation [163]: when the available free space is so tight that multiple cells cannot fit side-by-side, cells are necessarily restricted to end-on collisions between each other as they move, also inducing reorientations akin to those induced by collisions with surrounding obstacles. Therefore, as a first step toward incorporating this behavior into the model described in §3.2.1, we adopt a mean-field treatment of cell-cell interactions in which cells truncate each other's directed steps in a density dependent manner, inducing transient trapping events again of duration τ_t akin to collisions with obstacles.

In particular, wherever the local density b/φ is larger than a threshold value b^*/φ such that the mean separation between the surfaces of neighboring cells, $\bar{l}_{\text{cell}}$, decreases below the mean chord length $\bar{l}_c$, we expect that cell-cell collisions truncate l from $\bar{l}_c$ to $\bar{l}_{\text{cell}}$ (schematized in the middle inset of Fig. 3.1). Because the diffusion and chemotactic coefficients both vary as $\propto l^2$, we therefore multiply both density-independent parameters D_{b0} and χ_0 that characterize isolated cells by the density-dependent correction factor $\mu_{\text{crowd}}(b) = \left(\bar{l}_{\text{cell}}/\bar{l}_c\right)^2$, where the cell separation is approximated as the mean value $\bar{l}_{\text{cell}} \equiv (3\varphi/4\pi b)^{1/3} - d$; here, $d \approx 1\,\mu$m is the characteristic size of a cell, and therefore $b^* \equiv 3\varphi/[4\pi(\bar{l}_c + d)^3]$. As b increases further, it eventually reaches the jamming density $b_{\text{jammed}} \equiv 3\varphi/(4\pi d^3)$ at which cells cannot move at all, and $\bar{l}_{\text{cell}} = 0$; in this case, both transport parameters are zero, and the bacterial population can only spread *via* growth. Therefore, in Eq. 3.2, D_{b0} and χ_0 are

replaced by the corrected values

$$D_b(b) = D_{b0} \times \mu_{\text{crowd}}(b) \tag{3.5}$$

$$\chi(b) = \chi_0 \times \mu_{\text{crowd}}(b) \tag{3.6}$$

where the crowding correction factor $\mu_{\text{crowd}}(b)$ is piecewise defined as

$$\mu_{\text{crowd}}(b) = \begin{cases} 1 & \text{when } b \leq b^* \\ \left[\frac{\left(\frac{3\varphi}{4\pi b}\right)^{1/3} - d}{l_c} \right]^2 & \text{when } b^* < b < b_{\text{jammed}} \\ 0 & \text{when } b \geq b_{\text{jammed}} \end{cases} \tag{3.7}$$

as shown in Fig. 3.1; the limits b^* and b_{jammed} are indicated by the left and right vertical dashed lines, respectively. This way of correcting the diffusive term in Eq. 3.2 represents a simplifying approximation; strictly speaking, one cannot simply commute the divergence operator with the diffusion coefficient, given that D_b depends on $b(x, t)$ *via* the crowding correction factor. However, as we describe further in §3.2.4, this simplification does not appreciably influence our results and conclusions. We term cases with low cell density ($b < b^*$) the *obstacle collisions limited* regime described in (i) above; cases with intermediate cell density ($b^* \leq b < b_{\text{jammed}}$) the *cell collisions limited* regime; and cases with the highest possible density of cells ($b = b_{\text{jammed}}$) the *jammed growth spreading* regime described in (iii) below. Because we take the cells and surrounding obstacles to be incompressible, b cannot

exceed b_{jammed}.

(iii) *Jammed growth spreading.* When they are jammed, cells form a contact network that holds them in place and prevents motion by active propulsion. However, these cells can continue to proliferate if supplied with nutrient; based on the experiments in [163], we assume that the maximal growth rate γ is not affected by confinement. Thus, in this case, their high body stiffness enables growing cells to push outward on their neighbors; the bacterial population can then be treated as an incompressible "fluid" in which the added stress due to cellular growth relaxes rapidly *via* spreading, as is conventionally done in models of growing immotile populations [227,239–241] and supported by experiments [235,236]. Because we treat the obstacles comprising the medium as being rigid and immovable, and the interstitial free space large enough for cells to move through without being deformed, this process leads to jammed growth spreading. We incorporate this behavior into the Keller-Segel model following previous work modeling the growth of immotile biofilms [228]. In particular, at each time step $\delta_0 t$, we first identify the smallest x_i at which $b(x_i, t + \delta t)$ exceeds b_{jammed}; we then set $b(x_i, t + \delta t) = b_{\text{jammed}}$ and instead relocate the newly-formed cells $\delta b(x_i) \equiv b(x_i, t + \delta t) - b_{\text{jammed}}$ to the nearest location $x_j > x_i$ at which $b(x_j, t) < b_{\text{jammed}}$. We then repeat this process for all successive positions $x > x_i$ such that at time $t + \delta t$, the upper limit on cell density b_{jammed} is globally satisfied.

3.2.4 Details for simplification of diffusion term

Strictly speaking, one cannot simply commute the divergence operator with the diffusion and chemotactic coefficients, given that they depend on $b(x, t)$ *via* the crowding correction factor. Instead, the density-dependent diffusion and chemotactic coefficients given in Eq.

3.5–3.6, $D_b = D_{b0} \times \mu_{\text{crowd}}(b)$ and $\chi = \chi_0 \times \mu_{\text{crowd}}(b)$, respectively, must be incorporated into the flux $\vec{J}_m = -D_b \nabla b + b\chi \nabla f(c)$ before taking the divergence to obtain Eq. 3.2. This procedure would lead to diffusive and chemotactic terms $\nabla \cdot (D_b \nabla b)$ and $-\nabla \cdot (\chi b \nabla f(c))$ in Eq. 3.2, respectively. While we do indeed use the latter form for the chemotactic term, we use a simpler approximate form of the diffusive term, $D_b \nabla \cdot \nabla b = D_b \nabla^2 b$, moving forward in this chapter. In fact, utilizing the mathematically-correct form of the diffusive term in our model leads to nearly-identical results as with the simplified approximate form, as we show below, and thus does not change the key results and conclusions in this chapter. Hence, we choose to use the simplified approximate form in this chapter because it provides a straightforward way of incorporating the influence of confinement and crowding in modulating the diffusion coefficient.

In particular, the diffusive term can be expanded as:

$$\nabla \cdot (D_b \nabla b) = \nabla D_b \cdot \nabla b + D_b \nabla^2 b = \underbrace{D_{b0} \nabla \mu_{\text{crowd}} \cdot \nabla b}_{(i)} + \underbrace{D_b \nabla^2 b}_{(ii)}, \tag{3.8}$$

where term (ii) represents our simplified approximate form and (i) represents an additional correction required to make this approximation exact. In our one-dimensional coordinate (x) system, the correction term (i) can be written as $D_{b0} \frac{\partial \mu_{\text{crowd}}}{\partial x} \frac{\partial b}{\partial x} = D_{b0} \frac{\partial \mu_{\text{crowd}}}{\partial b} \left(\frac{\partial b}{\partial x}\right)^2$. This expression is non-zero only for $b^* < b < b_{\text{jammed}}$, where the constants $b^* \equiv 3\varphi/[4\pi(\bar{l}_c + d)^3]$ and $b_{\text{jammed}} \equiv 3\varphi/(4\pi d^3)$, since for values of b outside this range, $\mu_{\text{crowd}}(b)$ is a constant and thus $\partial \mu_{\text{crowd}}/\partial b = 0$. And within this range, $\partial \mu_{\text{crowd}}/\partial b$ decreases monotonically from its value evaluated at $b = b^*$ to zero at $b = b_{\text{jammed}}$, as can be seen from Fig. 3.1—precisely the same range in which $\partial b/\partial x \approx 0$, as can be seen from the density profiles in Figs. 3.5,

3.7, 3.9. Thus, we expect that the correction term $(i) \approx 0$, and the diffusive term can be reasonably approximated using the simpler expression $D_b \nabla^2 b$. Indeed, consistent with this expectation, performing all of our numerical simulations using the full expression Eq. 3.8 yields population spreading dynamics that are nearly identical to those presented in this chapter, as indicated by Fig. 3.2.

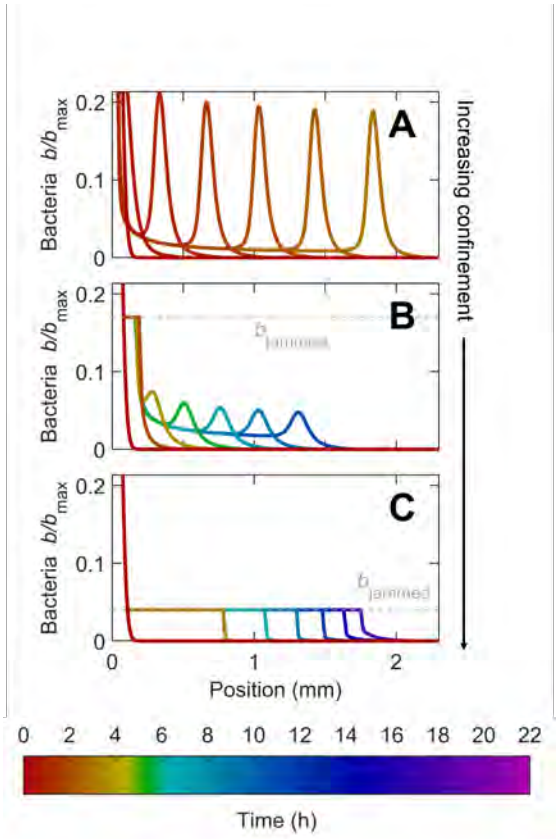

Figure 3.2: Simulations corresponding to Fig. 3.9A-C, but using the full diffusive term (Eq. 3.8) in our model; we observe nearly identical results, supporting our simplifying choice.

Beginning with density dependent diffusivity in the flux term the governing equation for

cell density is

$$\frac{\partial b}{\partial t} = -\nabla \cdot \big(- D_{b0}\mu_{\text{crowd}}(b)\nabla b + (bv_{\text{c}})\big) \; + \; b\gamma g(c). \tag{3.9}$$

Applying the product rule to the divergence term we obtain

$$\frac{\partial b}{\partial t} = D_{b0}\nabla \cdot \big(\mu_{\text{crowd}}(b)\big)\nabla b - D_{b0}\mu_{\text{crowd}}(b)\nabla \cdot (\nabla b) - \nabla \cdot \big(bv_{\text{c}}\big) \; + \; b\gamma g(c). \tag{3.10}$$

Applying the definition of divergence and gradient in rectilinear coordinates in one dimension x and applying the chain rule to $\frac{\partial \mu_{\text{crowd}}(b)}{\partial x} = \frac{\partial \mu_{\text{crowd}}(b)}{\partial b}\frac{\partial b}{\partial x}$ we get

$$\frac{\partial b}{\partial t} = D_{b0}\frac{\partial \mu_{\text{crowd}}(b)}{\partial b}\left(\frac{\partial b}{\partial x}\right)^2 + D_{b0}\mu_{\text{crowd}}(b)\frac{\partial^2 b}{\partial x^2} - \frac{\partial (bv_{\text{c}})}{\partial x} + b\gamma g(c). \tag{3.11}$$

The first term, $D_{b0}\frac{\partial \mu_{\text{crowd}}(b)}{\partial b}\left(\frac{\partial b}{\partial x}\right)^2$, has been ignored in our model, a consequence of applying cell density dependence later. To evaluate if this simplification to the model influences the results of our simulations, we perform the same simulations as in Fig. 3.9A-C now including this term shown in Fig. 3.2. Comparing the two figures, the results are nearly indistinguishable.

3.2.5 Implementation of numerical simulations

To explore the influence of confinement, we perform numerical simulations of Eqs. 3.1–3.2, modified as described in §3.2.3. Motivated by its simplicity and amenability to the

addition of our discrete jammed expansion rule, we implement a forward Euler method to solve these equations; specifically, we discretize the spatial coordinate x using a forward difference form for first derivatives and a central difference form for second derivatives. The update equations for nutrient concentration and bacterial cell density, corresponding to Eqs. 3.1–3.2 respectively, are then:

$$c_i^{n+1} = c_i^n + \delta t \left[\frac{D_c}{\delta x^2} (c_{i-1}^n - 2c_i^n + c_{i+1}^n) - \kappa b_i^n g(c_i^n) \right]$$

$$b_i^{n+1} = b_i^n + \delta t \left[\frac{D_{b0} \mu(b_i^n)}{\delta x^2} (b_{i-1}^n - 2b_i^n + b_{i+1}^n) - \frac{1}{\delta x} (b_{i+1}^n v_{c_{i+1}}^n - b_i^n v_{c_i}^n) + \gamma b_i^n g(c_i^n) \right]$$

where time points advance in discrete steps of δt and are indexed by n, and spatial positions are separated by discrete steps of δx and are indexed by i. The spatial resolution δx is 10 μm and the time step δt is 0.01 s; as shown in Fig. 3.3, these choices are sufficiently fine so that our results are not sensitive to the choice of resolution. We note that implicit methods (such as backwards Euler) or semi-implicit methods would likely improve the efficiency of the numerical simulations—an important consideration for those seeking to extend our work e.g., to higher spatial dimensions.

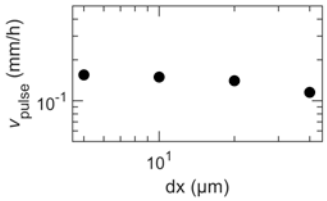

Figure 3.3: To assess the sensitivity of our results to numerical discretization, we repeat the simulation shown in Fig. 3.5, which has spatial resolution of $dx = 10$ μm, with varying values of dx; the time step dt is correspondingly varied as $dt = 0.01\text{ s} \times (dx/10\text{ μm})^2$. As shown in the figure, the final pulse velocity v_{fr} obtained from the simulations is not strongly sensitive to the choice of numerical discretization.

To connect our results to an experimental system, we use input parameters and initial conditions that mimic the experiments described in [163] (Chapter 2), which explored the chemotactic spreading of *E. coli* populations in 3D porous media composed of densely-packed hydrogel particles. Although the experimental system was cylindrical, we found that rectilinear coordinates capture the essential features of the system. Thus, we use a Cartesian rectilinear coordinate system extending to a maximum distance of 1.75×10^4 μm, matching the length of the experimental system. Because our system is one-dimensional, vectors (e.g. fluxes) oriented in the $+$ or $-x$ directions are represented by positive or negative quantities, respectively, with the vector notation suppressed. Both boundaries have no flux conditions. In these experiments, *L*-serine was considered to act as the primary nutrient and chemoattractant for cells. Because the hydrogel particles are polymer networks swollen in liquid, they are permeable to the nutrient, similar to many other naturally-occurring media such as biological gels and microporous clays/soils. Therefore, we take the nutrient diffusivity D_c to be equal to its value in bulk liquid, 800 $\mu m^2\ s^{-1}$ [242], and the nutrient is initially saturated at $c_\infty = 10$ mM throughout the simulation domain. For all the simulations, we use direct measurements of individual cells [28,45,163] to choose fixed values of the cellular parameters c_-, c_+, and γ given by 1 μM, 30 μM, and 0.69 h^{-1}, respectively; furthermore, as detailed in §3.2.6, we use the data from experiments on spreading populations [163] to directly determine c_{char} and κ, given by 10 μM and 1.3×10^{-12} mM $(\text{cells/mL})^{-1}\ s^{-1}$, respectively.

Each experiment used a long 3D-printed cylinder of close-packed cells not containing hydrogel particles ($\varphi = 1$) as the initial inoculum, embedded within and surrounded by the 3D porous medium. The cells then continued to spread radially outward through the pore space. Thus, as the initial condition in all the simulations, we consider a Gaussian

profile of $b(x, t = 0)$ centered at $x = 0$ with a full width at half maximum of 100 μm and a peak number density of $b_0 = b_{\max} \equiv 3/(4\pi d^3) = 2.4 \times 10^{11}$ cells/mL, where $b_{\max}$ is defined as the number density of close-packed cells and is therefore the maximum possible value of b_0—with the exception of the lower-density simulations presented in Figs. 3.7–3.8, which employ a lower value of b_0. Hence, for all simulations except those in Figs. 3.7–3.8, the initial inoculum has a maximal cell density $b_{\max} > b_{\text{jammed}}$, where b_{jammed} instead corresponds to the maximal possible density of cells in confinement ($\varphi < 1$). For simplicity, wherever $b(x, t = 0) > b_{\text{jammed}}$, we still apply the jammed growth spreading rule described in §3.2.3(iii), but with b_{jammed} replaced by $b(x, t = 0)$.

The experiments tuned cellular confinement by using porous media with varying porosities φ and mean chord lengths $\bar{l}_c$ [39], resulting in varying values of the transport parameters D_{b0} and χ_0 [38,163]. In particular, as determined from the experiments, D_{b0} and χ_0 both decrease with increasing confinement as cellular mobility is increasingly hindered. Hence, in our simulations, we tune confinement by varying these parameters, using the values of D_{b0} obtained from single-cell imaging [163] and extracting χ_0 from experimental measurements of population spreading, as detailed in §3.2.6.

3.2.6 Determining κ, c_{char}, and χ_0 parameters from experimental data

The parameter values for κ, c_{char}, and χ_0 are crucial for fitting to experimentally observed pulse propagation speeds. In our previous work [163] (Chapter 2), we chose values of κ and c_{char} based on previous measurements [28,45], and therefore only χ_0 was treated as a fitting parameter. While the previous simulations based on these choices reasonably captured the formation and propagation of bacterial pulses observed in experiments, as well as the

experimentally-observed dependence of pulse skewness, height, and speed on confinement, the widths of the simulated pulses differed noticeably from the experiments. Because the goal of this present paper is to more closely investigate pulse shape and dynamics, here we develop a new protocol to determine all three parameters κ, c_{char}, and χ_0 from the experimental data. The experiment is summarized in §3.2.5. The primary dataset we use for fitting (shown in Fig. 3.4 and taken from [163]) is obtained from a late time experimental profile for cells in intermediate confinement (corresponding to §3.3.1).

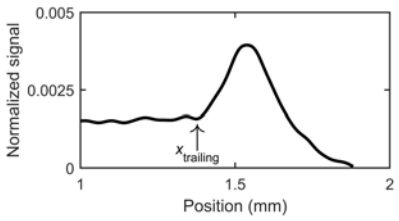

Figure 3.4: Experimental cellular signal of traveling front under intermediate confinement from [163]. Experiments begin with a dense packed cylindrical inoculum of *E. coli* embedded within a porous media with mean pore size 1.7 μm. A pulse forms and propagates outward; the dataset shows the final time point of 10.75 h. The experiment used confocal microscopy of cells constitutively expressing green fluorescent protein; we take the fluorescence data thereby obtained from the mid-plane of the bacterial cylinder and normalize it by the brightest region of the initial inoculum. This normalized cellular signal is then converted to cell density by multiplying with $b_{\text{max}} = 0.95 \times 10^{12}$ cells/mL. Arrow indicates location identified as trailing behind the pulse, x_{trailing}, and the corresponding cellular density is $b_{\text{trailing}} = 1.5 \times 10^9$ cells/mL.

Determining κ. At long times, given that the pulse is nearly unchanging in time, we take $\partial c/\partial t = -v_{\text{fr}}\partial c/\partial \omega$ and $\partial b/\partial t = -v_{\text{fr}}\partial b/\partial \omega$. Applying these definitions in Eqs. 3.1–3.2 and integrating over all space, with the boundary conditions $b(\omega = \infty) = 0$, $c(\omega = \infty) = c_\infty$, $b(\omega = 0) = b_{\text{trailing}}$, and $c(\omega = 0) = 0$ yields the steady-state relationship between nutrient influx into the pulse to the cells being shed at the rear, $\kappa = c_\infty \gamma / b_{\text{trailing}}$. Here, c_∞ was fixed in the experiments to be 10 mM and γ was directly measured to be $0.69\ \text{h}^{-1}$. Thus, using the $b_{\text{trailing}} = 1.5 \times 10^9$ cells/mL directly obtained from the experimental profile, we

obtain $\kappa = 1.3 \times 10^{-12}$ mM (cells/mL)$^{-1}$ s^{-1}. This value, which we use for all the simulations reported here, is in excellent agreement with previously reported values[28,45].

Determining c_{char} and χ_0. Having obtained κ, we next use the experimental data to determine c_{char} and χ_0. To do so, we first re-run the simulation of §3.3.1 but with c_{char} chosen to be either 1, 5, 10, 50, or 100 μM—values that span the range reported in previous experiments[28,29,45]. For each choice of c_{char}, we then determine the value of χ_0 for which the simulation v_{fr} best matches the experimental value. Then, having fit v_{fr}, we pick the value of c_{char} for which the simulated pulse width best matches the experimental data. Together, this iterative procedure yields the unique combination of $\{c_{\text{char}}, \chi_0\}$ that best matches the experimental long-time pulse speed and width. We thereby obtain $c_{\text{char}} = 10$ μM and $\chi_0 = 94$ μm^{2}s^{-1} for cells in intermediate confinement. Because c_{char} is an intrinsic cellular property, and thus does not depend on confinement, we then use this value of c_{char} for other simulations testing weak and strong confinement as well. For each of these, we again obtain χ_0 by fitting the long-time v_{fr} between simulations and the experiments. We obtain $\chi_0 = 3700$ μm^{2}s^{-1} and $\chi_0 = 16$ μm^{2}s^{-1} for weak and strong confinement, respectively.

3.2.7 Parameters

The confinement-dependent parameters are summarized in Table 3.1. The corresponding dimensionless parameters characterizing the Keller-Segel model (§3.2.2) are also summarized in Table 3.1:

- The diffusion parameter $\delta_0 \equiv D_c/D_{b0}$ increases with confinement as cellular mobility is increasingly hindered. For all conditions tested here, however, δ_0 is always much greater than one, reflecting fast diffusion of nutrient; thus, we expect that

nutrient levels vary over large spatial extents, as confirmed in the simulations that follow.

- For all conditions tested here, the directedness parameter $\alpha_0 \equiv \chi_0 / D_{b0}$ is always much greater than one, indicating that motile cells strongly direct their motion in response to the nutrient gradient established through consumption. Intriguingly, the α_0 determined from the experimental parameters decreases with increasing confinement, indicating that confinement more strongly hinders directed versus undirected motion—consistent with previous reports that confinement fundamentally alters the mechanism by which cells perform chemotaxis[163]. Further investigating the determinants of α_0 in confinement will be a useful direction for future experiments.

- Because the maximal growth rate is not affected by confinement[163], the yield parameter $\beta_0 \equiv \gamma / (b_0 \kappa / c_\infty)$ is independent of confinement for all of our simulations. For all simulations employing $b_0 = b_{\max}$, β_0 is much less than one, reflecting the fact that nutrient consumption by a maximally dense population is faster than cellular proliferation; conversely, for the lower-density simulations presented in Figs. 3.7–3.8, β_0 is much greater than one, indicating the dominant role of proliferation in this case.

Parameter	Weak confinement	Intermediate confinement	Strong confinement
φ	0.36	0.17	0.04
$\bar{l}_c\,(\mu m)$	4.6	3.1	2.4
$D_{b0}\,\left(\mu m^2 s^{-1}\right)$	2.3	0.93	0.42
$\chi_0\,\left(\mu m^2 s^{-1}\right)$	3700	94	16
$\bar{b}/b_{max}$	0.10	0.027	0.026
$\delta_0 \equiv D_c/D_{b0}$	340	860	1900
$\delta \equiv D_c/D_b(\bar{b})$	2.8×10^4	1.2×10^4	4.3×10^5
$\alpha = \alpha_0 \equiv \chi_0/D_{b0}$	1600	100	38
$\beta_0 \equiv \gamma/\left(b_0\kappa/c_\infty\right)$	0.0063	$0.0063\,(b_0 = b_{max}), 630\,(b_0 = 10^{-5} b_{max})$	0.0063
$\beta \equiv \gamma/\left(\bar{b}\kappa/c_\infty\right)$	0.06	0.23	0.25
$\Lambda_0 \equiv \alpha_0/\left(\beta_0\delta_0\right)$	750	$18\,(b_0 = b_{max}), 1.8 \times 10^{-4}\,(b_0 = 10^{-5} b_{max})$	1.3
$\Lambda \equiv \alpha/\left(\beta\delta\right)$	0.95	0.037	3.6×10^{-4}

Table 3.1: Parameters used to describe bacteria in weak, intermediate, and strong confinement, as defined in the text. All parameters are defined in the text and their values are obtained from experiments as detailed in §3.2.5 and the SI, with the exception of $\bar{b}$, which is determined directly from the simulation. We note that the values of α_0 are taken directly from the experiments in [163], which indicate that this parameter surprisingly decreases with increasing confinement. Thus, while we expect that both transport parameters χ_0 and D_{b0} are tuned by confinement in a similar way, with both proportional to $\bar{l}_c^2/\tau_t$, it appears from the experiments that the ratio of the proportionality constants for each is also confinement-dependent. That is, experiments suggest that confinement more strongly hinders directed (quantified by χ_0) versus undirected (quantified by D_{b0}) spreading. While more work needs to be done to fully unravel why this is the case, in absence of a theoretical model for the confinement-dependence of α_0, we directly use the experimental values in our work. Furthermore, in the absence of any experimental data assessing the influence of cell density on α, we make the simplest possible assumption that cell-cell collisions hinder both χ_0 and D_{b0} through the same crowding correction factor $\mu_{crowd}(b)$, which quantifies the reduction in free space available to the cells. Thus, we take $\alpha = \alpha_0$. Future experiments could further probe this density dependence and motivate the introduction of additional extensions to our model.

Therefore, for our simulations testing the influence of confinement on bacterial spreading, the parameter $\Lambda_0 \equiv \alpha_0/(\beta_0\delta_0)$ varies over a broad range, decreasing over nearly three orders of magnitude as confinement increases. We note that because the different parameters $\delta_0, \alpha_0, \beta_0$ do not incorporate the influence of density-dependent cellular crowding, we do not expect this transition to occur precisely at $\Lambda_0 \approx 1$. We therefore define a new version of this parameter, $\Lambda \equiv \alpha/(\beta\delta)$, where now $\delta \equiv D_c/D_b(\bar{b})$, $\alpha \equiv \chi(\bar{b})/D_b(\bar{b}) = \alpha_0$, and $\beta \equiv \gamma/(\bar{b}\kappa/c_\infty)$ (Table 3.1); $\bar{b}$ is defined as the long-time mean cell density within each propagating pulse, and is directly calculated from each simulation as described further below. Thus, the newly-defined Λ explicitly incorporates density-dependent crowding. As summarized in Table 3.1, our simulations explore the transition from weak confinement ($\Lambda = 0.95$) to strong confinement ($\Lambda = 3.6 \times 10^{-4}$); consistent with our expectation, this range reflects a transition from chemotactic to growth-driven spreading, as demonstrated directly by the simulations presented below.

3.3 Results

3.3.1 Intermediate confinement

As a prototypical starting case, we first examine bacterial spreading from a dense-packed Gaussian-shaped inoculum under intermediate confinement ($\Lambda = 0.037$), shown by the initial profile for $t = 0$ in Fig. 3.5A. The simulation incorporates both motility and growth. The cells rapidly deplete nutrient locally *via* consumption over a time scale $\sim c_\infty/(\kappa b_{\max}) \approx 30$ s, establishing a steep nutrient gradient at the leading edge of the population. This gradient extends over a large distance ahead of the population (Fig. 3.5B and inset)—as expected from our calculation of the diffusion parameter $\delta_0 \gg 1$. Cells at this leading edge

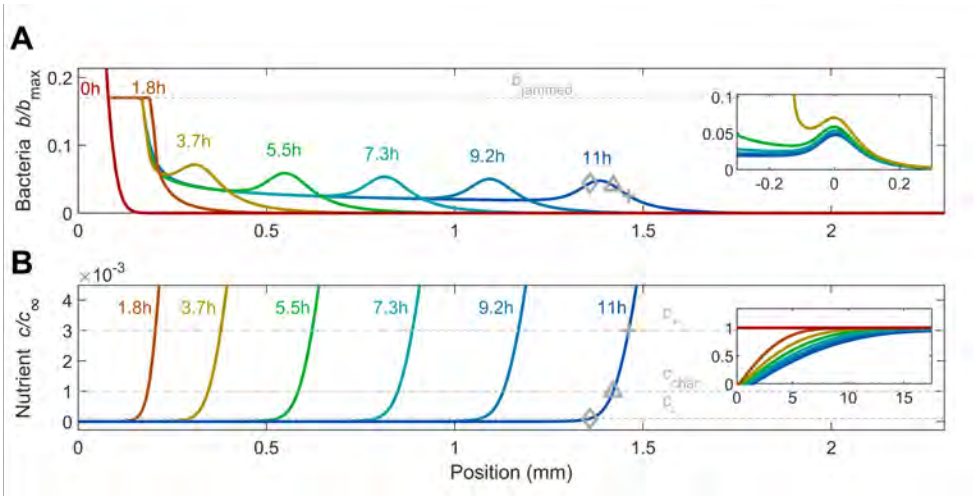

Figure 3.5: Results from a numerical simulation of population spreading in intermediate confinement. The simulation incorporates both motility and growth. (A) shows the dynamics of the cells while (B) shows the corresponding dynamics of the nutrient, quantified by the normalized density $b/b_{\max}$ and concentration c/c_∞, respectively. As noted in §3.2.5, the initial inoculum is composed purely of dense-packed cells with liquid between them ($\varphi = 1$), with the entire inoculum surrounded by the obstacle-filled medium ($\varphi = 0.17$); hence, the initial inoculum has $b = b_{\max}$, which is larger than b_{jammed}, the jamming density of cells in confinement. Different colors indicate different times as listed. The dense inoculum initially centered about the origin spreads outward, first as a jammed front (jamming density shown by the dashed grey line in A), then detaching as a coherent lower-density pulse that propagates continually *via* chemotaxis. At long times, this pulse appears to approach an unchanging shape and speed, as suggested by the collapse of the profiles in the upper inset (showing the same data, but shifted horizontally to center the peaks). The cellular dynamics arise in response to consumption of the nutrient, which is initially saturated everywhere, but is rapidly depleted and forms a gradient that is propagated with the pulse (inset shows the same data but with both axes zoomed out). In B, the three dashed grey lines show the characteristic concentrations of sensing c_+ and c_- and the characteristic Monod concentration c_{char}; the corresponding positions are shown by the pluses, diamonds, and triangles, respectively, in A-B.

then continue to grow outward as a jammed front with $b = b_{\text{jammed}}$, shown by the flat region at $t = 1.8$ h in Fig. 3.5A. Eventually, a lower-density, coherent pulse of cells detaches from this jammed region ($t = 3.7$ h), continues to propagate the nutrient gradient along with it, and thus continues to spread outward ($t > 3.7$ h), as shown by the outward-moving peak in Fig. 3.5A.

Indeed, this pulse spans the extent over which nutrient varies between the upper and lower bounds of sensing, c_+ and c_- (pluses and diamonds shown for the $t = 11$ h profiles,

respectively)—reflecting the central role of chemotaxis in driving its propagation. The forward face of the pulse is also exposed to sufficient nutrient for cells to proliferate (with $c \geq c_{\text{char}}$, the characteristic Monod concentration, shown by the triangles on the $t = 11$ h profiles)—suggesting that cellular growth contributes to population spreading over long time scales, as well. The overall width of this pulse, $W \approx 200$ μm, is set by the length scale over which nutrient is depleted by consumption; at its rear, the nutrient concentration and nutrient gradient are both low, causing both growth and chemotaxis to be hindered. As a result, cells are shed at a near-constant density $b_{\text{trailing}} \approx 0.02 b/b_{\text{max}}$ (see 0.5 mm $< x <$ 1.2 mm in Fig. 3.5A). This coherent pulse of cells continues to move apparently without an appreciable change in shape, as suggested by the inset to Fig. 3.5A, at a speed $v_{\text{fr}} \approx 0.15$ mm/h. However, given the limited duration of the simulation, our results do not enable us to definitively conclude that the simulated pulse develops into a traveling wave with an unchanging shape; building on our simulation to explore longer length and time scales to test this possibility will be a useful direction for future work. The nutrient profile concomitantly propagates with the pulse, as shown in Fig. 3.5B. Notably, similar spreading behavior was observed in experiments[163]; as shown in Fig. 3.4, in both simulation and experiment, we observe similarly-shaped bacterial pulses with comparable widths, trailing densities (compared to the peak densities), and final positions at $t \approx 11$ h.

Initial dynamics

To further characterize these spreading dynamics, we track the position X_f of the leading edge of the population over time t, as shown in Fig. 3.6A. Specifically, motivated by a similar definition used in prior experiments[163], we define X_f as the position at which b falls

below the threshold value $b/b_{\max} = 10^{-4}$. Initially, population spreading is hindered ($X_f \sim t^{\nu}$ with $\nu \ll 1$ e.g., red point), but as the coherent pulse forms and propagates, it eventually approaches constant speed spreading ($\nu \approx 1$ e.g., blue point). A similar transition from hindered to constant speed spreading was observed in experiments [163], although the underlying reason has thus far remained unclear. Here, we use our model to clarify the origin of this transition.

In particular, we examine the two different contributions to the motility-driven flux of cells—active diffusion and chemotaxis—for the population at early and late times (Fig. 3.6B–C, respectively); for simplicity, we do not consider the added influence of growth, which only plays an appreciable role for long times $t \gg \gamma^{-1}$, until the next subsection. The magnitude of the active diffusive flux $-D_b(b)\nabla b = -D_{b0}\mu_{\text{crowd}}(b)\nabla b$ as it varies across the population is shown by the dashed lines in the bottom panels of Fig. 3.6B–C, while the magnitude of the chemotactic flux $bv_c = b\chi_0\mu_{\text{crowd}}(b)\nabla f(c)$ is shown by the dash-dotted lines instead. At early times, the gradient in cell density is steep, as set by the sharp initial profile of cells and the limited extent of subsequent population spreading (Fig. 3.6B, top). As a result, spreading is primarily due to active diffusion, which dominates over chemotaxis, as shown in the lower panel of Fig. 3.6B. By contrast, as cells spread outward, the gradient in cell density becomes less steep. As a result, at late times, spreading is primarily due to chemotaxis, which dominates over active diffusion, as shown in the lower panel of Fig. 3.6C. This behavior is also reflected by the bottom set of circles and squares in Fig. 3.6D, which represent the maximal diffusive and chemotactic fluxes across the population (exemplified by the circles and squares in Fig. 3.6B–C) over time. Initially, the diffusive flux dominates over the chemotactic flux; however, as the population continues to spread and

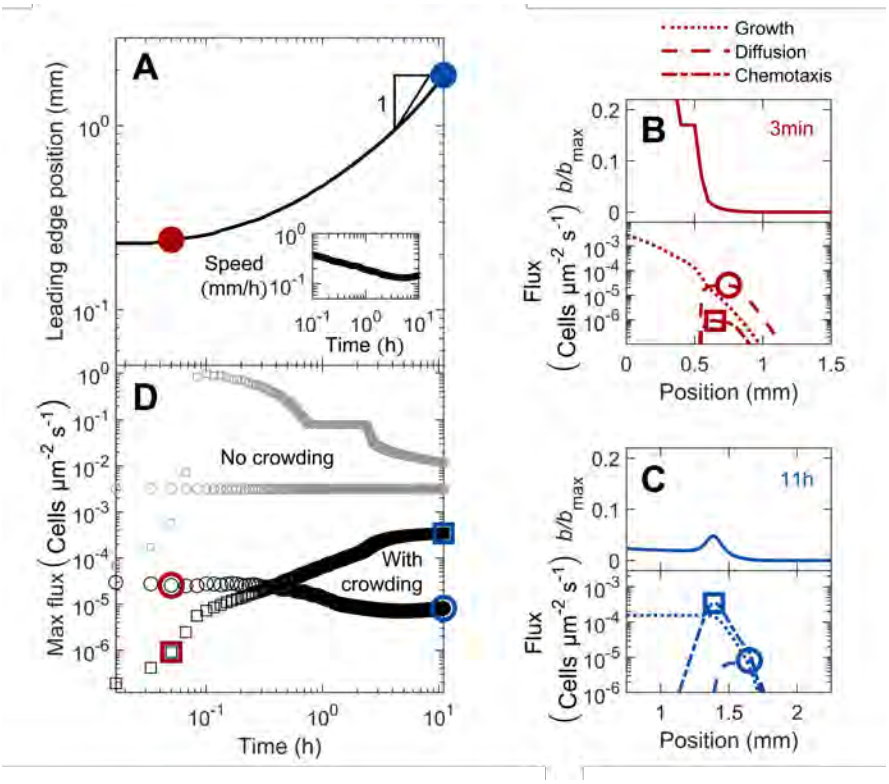

Figure 3.6: Population dynamics, morphology, and fluxes driving spreading for the simulation of bacteria in intermediate confinement (Fig. 3.5). The simulation incorporates both motility and growth. (A) Increase in the position of the leading edge of the population is initially hindered (red), but approaches constant-speed motion indicated by the triangle at long times (blue). The corresponding instantaneous speed v_{fr} is shown in the inset. (B) At a short time corresponding to the red point in A, the population expands as a jammed front (top panel). Lower panel shows that cellular growth and diffusion are the primary contributors to the expansion of this front. (C) At a long time corresponding to the blue point in A, the population spreads as a coherent pulse (top panel). Lower panel shows that chemotaxis is the primary contributor to pulse propagation. Positions of the maximal diffusive and chemotactic fluxes are indicated by the circles and squares, respectively, in B-C; note the slight upward kink in the diffusive flux in C indicated by the circle. (D) Variation of the maximal diffusive and chemotactic fluxes, indicated by the circles and squares in B-C, over time. The initial population dynamics are dominated by cellular diffusion (circles), while at longer times chemotaxis dominates (squares). To illustrate the role played by cellular collisions, we show the same data with and without the crowding correction μ_{crowd} in the upper (grey) and lower (black) datasets; crowding hinders population spreading, as shown by the vertical offset in the curves, but plays a less appreciable role at long times, as shown by the curves approaching each other.

consume nutrient, the diffusive flux decreases and the chemotactic flux increases, with both eventually approaching constant values at long times.

Another key factor that hinders the initial population spreading is cellular crowding. To assess the influence of crowding, we compare the maximal diffusive and chemotactic fluxes across the population, but with or without the crowding correction factor $\mu_{\text{crowd}}(b)$ (corresponding to the "with crowding" and "no crowding" datasets, respectively, in Fig. 3.6D). In both cases, the active diffusive flux dominates over the chemotactic flux initially, but chemotaxis eventually dominates as the population continues to spread and establish the nutrient gradient (e.g. top set of squares for $t \leq 0.1$ h). The spreading of the population remains hindered, however; due to the high initial density of cells, crowding continues to limit the chemotactic flux of cells, only enabling a small fraction at the leading edge of the population to spread outward—as exemplified by the first two profiles in Fig. 3.5A, the sharp decrease in both diffusive and chemotactic fluxes for $x < 0.5$ mm in Fig. 3.6B, and the large difference between the two sets of squares in Fig. 3.6D. Eventually, as this leading edge continues to spread, crowding in the forward face of the population becomes sufficiently low, enabling the coherent pulse of cells to detach from the population—as exemplified by the $t = 3.7$ h profile in Fig. 3.5A and the "kink" in the top set of squares at $t \approx 3$ h in Fig. 3.6D. Hindrance due to crowding continues to decrease over time, as shown by the diminishing difference between the two sets of squares in Fig. 3.6D for $t > 3$ h, and eventually approaches a constant value.

Hence, population spreading is initially slow due to the time required for cellular consumption to establish a sufficiently strong nutrient gradient to drive chemotactic spreading. Cellular crowding near the initial inoculum then continues to hinder spreading until

enough of the forward face of the population has spread outward—enabling cells to detach as a coherent pulse that continues to move outward, eventually approaching a constant speed.

Long-time behavior

Having established how the spreading population forms a moving pulse, we now seek to clarify the factors that continue to drive its propagation. As previously described (Fig. 3.6), active diffusion plays a negligible role at these longer times. Instead, as noted previously when describing the $t = 11$ h profiles in Fig. 3.5, we expect that chemotaxis and growth are the principal contributors to population spreading. In particular, the outward-moving pulse spans the extent over which nutrient varies between the upper and lower bounds of nutrient sensing—reflecting the central role of chemotaxis in driving its propagation. The forward face of the pulse is also exposed to sufficient nutrient for cells to proliferate—suggesting that cellular growth contributes to spreading, as well. Indeed, the time scale over which this pulse propagates over its width $\sim W/v_{\mathrm{fr}} = 1.3$ h is comparable to the time scale of cellular proliferation, $\gamma^{-1} = 1.4$ h, further indicating that growth may contribute to population spreading. However, the relative influence of chemotaxis versus growth in driving population spreading remains unclear.

Hence, we examine the long-time behavior of the pulse by considering a coordinate system that moves with the pulse, $\omega \equiv x - tv_{\mathrm{fr}} + \omega_0$; ω_0 is a constant shift factor chosen such that $\omega = 0$ is located at the rear of the pulse, at which $b \approx b_{\mathrm{trailing}}$. Here, both the bacterial and nutrient gradients are negligible, eliminating diffusive and chemotactic fluxes of cells, as shown in Fig. 3.6C. Within a time increment dt, the moving pulse leaves behind $N_{\mathrm{loss}} \approx$

$b_{\text{trailing}} v_{\text{fr}} A_c dt$ cells, where A_c is the transverse cross sectional area. Simultaneously, growth generates $N_{\text{grown}} \approx A_c dt \int_{\omega=0}^{\infty} b(\omega')\gamma g(\omega') d\omega'$ new cells within the pulse. Therefore, $N_{\text{loss}} \approx N_{\text{grown}}$ to preserve what we assume for simplicity to be a nearly-unchanging pulse of cells (Fig. 3.5A, inset).

More generally, at locations further ahead ($\omega \geq 0$), $N_{\text{motile}} \approx \vec{J}_m A_c dt$ cells also travel with the pulse through their motility-driven flux $\vec{J}_m = -D_b \nabla b + b v_c$; here, b, ∇b, D_b, and v_c are all ω-dependent quantities. Thus, an unchanging profile of cells requires the more general flux balance $N_{\text{loss}} - N_{\text{motile}} \approx N_{\text{grown}}$, where now $N_{\text{loss}} \approx b v_{\text{fr}} A_c dt$ and $N_{\text{grown}} \approx A_c dt \int_{\omega}^{\infty} b(\omega')\gamma g(\omega') d\omega'$; that is,

$$\underbrace{b v_{\text{fr}}}_{\text{Loss}} + \underbrace{D_b \nabla b}_{\text{Diffusion}} - \underbrace{b v_c}_{\text{Chemotaxis}} \approx \underbrace{\int_{\omega}^{\infty} b\gamma g d\omega'}_{\text{Growth}} \tag{3.12}$$

where all quantities except for the constants v_{fr} and γ are position-dependent. This equation quantifies the intuition that the cells that cannot keep up with the moving pulse through their motility must be replaced by growth so as to prevent a net loss of cells from the region ahead of ω. Therefore, for a given position ω, the right hand side of Eq. 3.12 represents the additional contribution to the overall spreading of the pulse due to cellular growth at $\omega \geq 0$. We therefore term this quantity the *growth flux* and compare it to the chemotactic flux $b v_c$.

Both fluxes are shown for the final profile in Fig. 3.6C; the growth flux is shown by the dotted line and the chemotactic flux is shown by the dash-dotted line, both plotted on a logarithmic scale. A version showing these fluxes on linear scales is shown in Fig. 3.10E.

For this case of intermediate confinement, both fluxes are appreciable, with the maximal

chemotactic flux (3.4×10^{-4} cells $\mu m^{-2} s^{-1}$) slightly larger than the maximal growth flux (1.5×10^{-4} cells $\mu m^{-2} s^{-1}$), indicating that chemotaxis plays a greater role in driving population spreading. To further quantify this behavior, we evaluate Eq. 3.12 at two distinct positions: the rear of the pulse ($\omega = 0$) and the peak of chemotactic flux, which we denote ω_{peak} (indicated by the square in Fig. 3.6C). At both locations, the gradient in cell density is approximately zero, eliminating diffusive flux and simplifying our analysis. The chemotactic flux is also approximately zero at the rear of the pulse ($x \approx 1.2$ mm in Fig. 3.6C). Moreover, at both locations, the growth flux is approximately the same—reflecting the fact that only the forward face of the pulse is exposed to sufficient nutrient for cells to proliferate. Hence, equating both of these implementations of Eq. 3.12 yields an expression for the long-time pulse speed:

$$v_{fr} \approx v_c(\omega_{peak}) + v_{fr} \frac{b_{trailing}}{b_{peak}}, \tag{3.13}$$

where we have defined $b_{peak} \equiv b(\omega_{peak})$. Therefore, the ratio $b_{trailing}/b_{peak} = 40\%$ approximates the fraction of the overall pulse speed attributable to growth, while the remaining 60% is due to chemotaxis.

This analysis also provides a way to extend a previous scaling estimate[28] of the long-time pulse speed v_{fr}, which did not incorporate the influence of confinement in regulating spreading. First, we note that the chemotactic velocity scales as $v_c(\omega_{peak}) \sim \chi\left(b_{peak}\right)/W$, where W is the pulse width. Next, we relate the mean number density of cells $\bar{b} \equiv W^{-1} \int_0^\infty b d\omega'$ to v_{fr} through a flux balance of cells at long times, when the shape of the pulse is unchanging over time. In particular, as described earlier, the rate at which cells are left behind the pulse, $b_{trailing} v_{fr} A_c$, is balanced by the rate at which growth generates new

cells in the pulse, $A_c \int_0^\infty b\gamma g d\omega' = A_c \bar{b} W \gamma \bar{g}$, where we have defined the cell-weighted mean $\bar{g} \equiv \int_0^\infty g(c(\omega'))bd\omega' / \int_0^\infty bd\omega' = \int_0^\infty g(c(\omega'))bd\omega' / (\bar{b}W)$. This flux balance yields $W = b_{\text{trailing}} v_{\text{fr}} / \left(\bar{b}\gamma\bar{g}\right)$, and therefore, $v_c(\omega_{\text{peak}}) \sim \chi\left(b_{\text{peak}}\right) \bar{b}\gamma\bar{g} / \left(b_{\text{trailing}} v_{\text{fr}}\right)$. Substituting this expression into Eq. 3.13,

$$v_{\text{fr}} \approx \chi\left(b_{\text{peak}}\right) \frac{\bar{b}\gamma\bar{g}(c)}{b_{\text{trailing}} v_{\text{fr}}} + v_{\text{fr}} \frac{b_{\text{trailing}}}{b_{\text{peak}}}. \tag{3.14}$$

Multiplying both left and right hand sides by v_{fr}, grouping terms to solve for v_{fr}^2, and multiplying the resulting solution by $\frac{b_{\text{peak}} b_{\text{trailing}}}{b_{\text{peak}} b_{\text{trailing}}}$ then yields our ultimate scaling estimate:

$$v_{\text{fr}}^2 \approx \chi\left(b_{\text{peak}}\right) \gamma\bar{g}(c) \frac{\bar{b} b_{\text{peak}}}{b_{\text{trailing}}(b_{\text{peak}} - b_{\text{trailing}})}. \tag{3.15}$$

This estimate thus extends a previous calculation [28] by explicitly incorporating the influence of confinement. To evaluate the accuracy of this estimate, we use the long-time simulation data to directly determine all the parameters on the right hand side of Eq. 3.15 and thereby obtain v_{fr}. We find reasonable agreement between the predicted (*via* Eq. 3.15) and simulated speeds to within a factor of two: the predicted value is 0.08 mm/h, while the simulation yields 0.15 mm/h. This agreement also extends to the case of weak confinement, discussed further in §3.3.2, for which the predicted value is 0.3 mm/h, while the simulation yields 0.8 mm/h, within a factor of 2.5. Hence, Eq. 3.15 provides a straightforward way to approximately relate the long-time shape of a pulse to its propagation speed, even in confinement.

Finally, we note that the fluxes associated with chemotaxis and growth also determine

the overall shape of the spreading population; for simplicity, we neglect the diffusive flux, given that it is at least one order of magnitude smaller than the chemotactic and growth fluxes (Fig. 3.6C). In particular, as quantified in Eq. 3.12, the cellular profile $b(\omega)$ is given by the sum of the chemotactic and growth fluxes, scaled by the constant v_{fr}. Our results confirm this expectation: as shown in Fig. 3.6C, the location of the bacterial pulse nearly coincides with the peak in the chemotactic flux, while the steady increase in growth flux from the leading edge to the rear coincides with the additional asymmetry in the bacterial profile arising from the trail of cells shed from the moving pulse. Taken together, these results therefore demonstrate that the interplay between chemotaxis and growth determines both the long-time speed and shape of the spreading population.

Influence of initial cell density

Our analysis thus far considered a dense initial inoculum, for which cellular crowding hinders the formation and detachment of a pulse; at much longer times, this less-crowded pulse no longer resembles the initial inoculum, but instead is shaped by the interplay of chemotaxis and growth (Fig. 3.6). We therefore expect that for a lower-density inoculum, a similar pulse also emerges at long times, but with initial dynamics that are limited instead by the time required for cellular consumption to establish a sufficiently strong nutrient gradient. To test this expectation, we repeat the simulation shown in Fig. 3.5, but using an initial peak number density of cells that is 10^5 times smaller ($b_0 = 10^{-5} b_{\mathrm{max}}$).

In the previously-considered case of a dense inoculum, the cells deplete nutrient rapidly *via* consumption, and the population subsequently spreads from its leading edge as a growing jammed front (first two curves in Fig. 3.5). By contrast, with a more dilute in-

oculum, nutrient depletion takes much longer. Instead, the population continually grows and spreads as a whole (red to blue curves in Fig. 3.7A inset), not just at its leading edge, without appreciably depleting nutrient. It eventually reaches a maximal density $b' = b_0 e^{\gamma t'}$ for which the time scale of subsequent nutrient depletion $t_{\text{dep}} \sim c_\infty / (\kappa b')$ is comparable to the time scale of subsequent growth $t_g \sim \gamma^{-1}$; equating these time scales yields $t' = \gamma^{-1} \ln\left(\frac{c_\infty \gamma}{b_0 \kappa}\right)$. Therefore, we expect that nutrient is fully depleted at the initial inoculum after $t' + t_{\text{dep}} \sim \gamma^{-1}\left[\ln\left(\frac{c_\infty \gamma}{b_0 \kappa}\right) + 1\right] \approx 11$ h. The simulation results are consistent with this estimate, which neglects spatial variation in nutrient availability through the entire population and thus serves as a lower bound, showing that nutrient is fully depleted at the initial inoculum after ~ 14 h (red to blue curves in Fig. 3.7B inset). The nutrient gradient again extends over a large distance ahead of the population, as expected from our calculation of the diffusion parameter $\delta_0 \gg 1$.

Unlike the case of a dense inoculum, the population does not subsequently spread as a jammed front. Instead, once the nutrient gradient is sufficiently strong, a coherent pulse of cells again detaches *without* the prior formation of a jammed front, continues to propagate the nutrient gradient with it, and continues to spread outward ($t > 15$ h in Fig. 3.7). Consistent with our expectation, this pulse is noticeably similar to that which arises in the dense inoculum case: it has a nearly-identical shape and also appears to move without an appreciable change in shape, eventually reaching approximately a similar constant speed $v_{\text{fr}} \approx 0.1$ mm/h (compare late-time profiles in Figs. 3.5 and 3.7). Evaluating the speed by instead tracking the position of the peak, instead of the leading edge, also yields a comparable value of $v_{\text{fr}} \approx 0.16$ mm/h.

To further characterize the population spreading dynamics, we again plot the leading

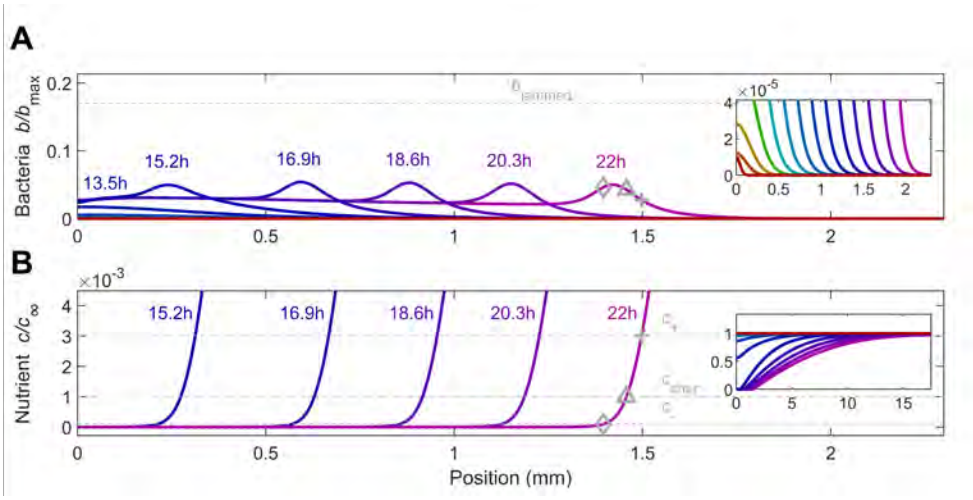

Figure 3.7: Results from a numerical simulation of population spreading in intermediate confinement starting from a more dilute inoculum. The simulation incorporates both motility and growth. (A) shows the dynamics of the cells while (B) shows the corresponding dynamics of the nutrient, quantified by the normalized density $b/b_{\max}$ and concentration c/c_∞, respectively. Different colors indicate different times as listed. The dilute inoculum (jamming density shown by the dashed grey line in A) initially centered about the origin first grows exponentially and spreads diffusively until nutrient is locally depleted (upper inset shows the same data, but zoomed in to the vertical axis); only then does a coherent pulse detach and propagate continually *via* chemotaxis in response to the nutrient gradient (lower inset shows the same data but with both axes zoomed out). Even though the short-time behavior is different from the case of a more dense inoculum shown in Fig. 3.5, the long-time behavior of this pulse is identical. To facilitate comparison with Fig. 3.5, in B, the three dashed grey lines again show the characteristic concentrations of sensing c_+ and c_- and the characteristic Monod concentration c_{char}; the corresponding positions are shown by the pluses, diamonds, and triangles, respectively, in A-B.

edge position X_f as a function of time t. As in the case of a dense inoculum, $X_f \sim t^\nu$ with $\nu \ll 1$ at early times, transitioning to $\nu \approx 1$ at later times (Fig. 3.8A); however, these seemingly similar dynamics reflect fundamentally different underlying processes at early times. With a more dilute inoculum, slower nutrient depletion causes the diffusive flux to initially dominate over chemotaxis (Fig. 3.8B) *without* any influence of cellular crowding—indicated by the overlap of the early-time points with/without the crowding correction in Fig. 3.8D. As cells continue to grow and consume nutrient, they eventually establish a sufficiently strong gradient and spread as a coherent pulse *via* chemotaxis—as indicated by

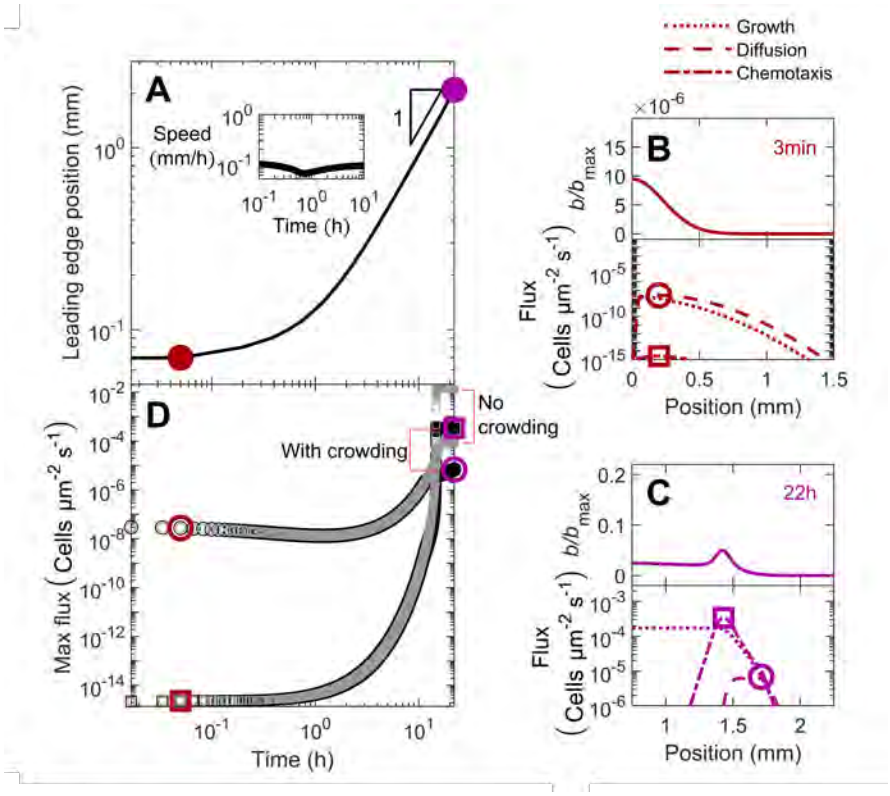

Figure 3.8: Population dynamics, morphology, and fluxes driving spreading for the simulation of bacteria in intermediate confinement, but from a more dilute initial inoculum (Fig. 3.7). The simulation incorporates both motility and growth. (A) Increase in the position of the leading edge of the population is initially hindered (red), but approaches constant-speed motion indicated by the triangle at long times (purple). The corresponding speed v_{fr} is shown in the inset. (B) At a short time corresponding to the red point in A, the population grows exponentially (top panel) and spreads primarily through growth and diffusion (lower panel). (C) At a long time corresponding to the purple point in A, the population spreads as a coherent pulse (top panel). Lower panel shows that chemotaxis is the primary contributor to pulse propagation. Positions of the maximal diffusive and chemotactic fluxes are indicated by the circles and squares, respectively, in B-C; note the slight upward kink in the diffusive flux in C indicated by the circle. (D) Variation of the maximal diffusive and chemotactic fluxes, indicated by the circles and squares in B-C, over time. The initial population dynamics are dominated by cellular diffusion (circles), while at longer times chemotaxis dominates (squares). To illustrate the role played by cellular collisions, we show the same data with (black) and without (grey) the crowding correction μ_{crowd} in the datasets indicated by the red lines; the data are identical except at long times, when crowding slightly hinders population spreading.

the dominant role of the chemotactic flux at long times (Fig. 3.8C-D). At these later times, the different contributions to the bacterial flux are nearly identical to those that drive pulse propagation in the case of a dense inoculum (compare Figs. 3.8C and 3.6C). Indeed, the fractions of the overall pulse speed attributable to chemotaxis and growth, as quantified by Eq. 3.13, are $\approx 58\%$ and 42%, respectively—nearly identical to the case of a dense inoculum. Hence, while the initial dynamics of population spreading are sensitive to the initial cell density—consistent with experiments[163]—the properties of the pulse that forms and continues to drive spreading at long times are not, instead being set solely by the interplay between chemotaxis and growth.

3.3.2 Influence of confinement

For the case of intermediate confinement explored thus far, we have established that chemotaxis and growth both drive population spreading at long times. How does this behavior change with confinement? As quantified in Figs. 3.6D and 3.8, confinement-induced crowding limits the chemotactic flux; therefore, we expect that with reduced or increased confinement, chemotaxis or growth plays a more dominant role in driving spreading, respectively. To test this expectation, we perform the same simulation with a dense inoculum as in Figs. 3.5–3.6, but with different values of the confinement-dependent parameters as summarized in Table 3.1. In particular, our simulations explore $\Lambda = 0.95$, 0.037, and 3.6×10^{-4}, representing weak, intermediate, and strong confinement (top, middle, and bottom rows in Figs. 3.9–3.10), respectively.

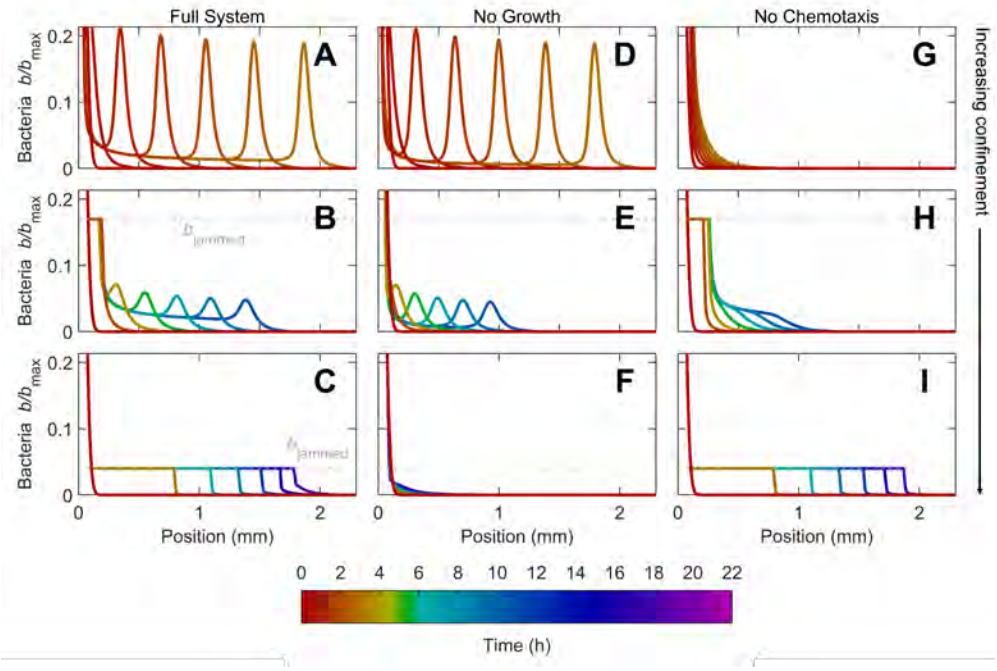

Figure 3.9: Increasing confinement causes a transition from fast chemotactic pulse propagation to slower jammed growth expansion. Panels show results from numerical simulations of population spreading from the same dense inoculum initially centered about the origin in weak, intermediate, and strong confinement, shown by top, middle, and bottom rows respectively. First column shows the results of the full model, while second and third columns show the same simulations with growth or chemotaxis omitted, respectively. We only show the normalized cellular density $b/b_{\max}$ for clarity. As noted in §3.2.5, the initial inoculum is composed purely of dense-packed cells with liquid in between them ($\varphi = 1$), surrounded by the obstacle-filled medium ($\varphi < 1$); hence, the initial inoculum has $b = b_{\max}$, which is larger than b_{jammed}, the jamming density of cells in confinement. Different colors indicate different times as listed in the color scale. In weak confinement, a coherent pulse rapidly detaches and continually propagates; this pulse is driven primarily by chemotaxis, and thus, omitting growth barely changes the dynamics while omitting chemotaxis abolishes the propagation altogether. Conversely, in strong confinement, the population spreads slowly as a jammed front, driven primarily by growth. In intermediate confinement, both growth and chemotaxis drive population spreading. The dashed grey line shows the jamming density, which varies depending on confinement (and is larger than the vertical scale in the top row).

In all cases, the cells first rapidly deplete nutrient locally *via* consumption, generating a nutrient gradient that again extends over a large distance and drives subsequent spreading at the leading edge of the population. However, consistent with our expectation, and with experimental observations[163], the nature of this spreading is strongly confinement-dependent.

Weak confinement

In the case of weak confinement, cells detach and spread as a lower-density, coherent, propagating pulse *without* first growing outward as a jammed front (Fig. 3.9A), unlike the case of intermediate confinement (Fig. 3.9B). This pulse is notably sharper and faster, with the long-time pulse speed and peak height ≈ 5.4 and 3.9 times larger than in intermediate confinement (also compare Panels A–B and D–E in Fig. 3.10)—reflecting the dominant role of chemotaxis in driving spreading, as expected from the larger value of Λ. Quantification of the different fluxes driving spreading corroborates this expectation (Fig. 3.10D); indeed, following our previous analysis summarized by Eqs. 3.12–3.13, we find that $\approx 93\%$ of the overall pulse speed is attributable to chemotaxis in the case of weak confinement.

As a final confirmation of this point, we re-run the simulations, but with either growth or chemotaxis removed—shown by the second and third columns of Fig. 3.9, respectively—thereby isolating the contributions of chemotactic and growth-driven spreading. In the prototypical case of intermediate confinement, both chemotactic and growth-driven spreading play appreciable roles; compare Panels E and H to B in Fig. 3.9, as well as the different curves in Fig. 3.10B and E. However, in the case of weak confinement, chemotactic spreading dominates, as expected; the simulation without growth (Fig. 3.9D) is nearly identical

to that incorporating all factors (Fig. 3.9A), while the simulation without chemotaxis (Fig. 3.9G) yields a population that barely spreads—also seen by comparing the different curves in Fig. 3.10A and D. Therefore, chemotactic propagation dominates under lesser confinement, enabling the population to spread faster as a sharp, coherent pulse.

Strong confinement

Population spreading is markedly different in strong confinement. In this case, cells do not form a coherent pulse at all; instead, they continually grow outward as a jammed front (Fig. 3.9C), unlike the case of intermediate confinement (Fig. 3.9B). Notably, this front does *not* have a well-defined speed at long times, in stark contrast to the cases of weaker confinement explored previously. Instead, the leading edge position progresses as $X_f \sim t^{\nu}$ with $\nu \approx 0.5$ at long times, as shown by the solid curve in Fig. 3.10C—and thus, the population spreads less effectively. This diffusive scaling of X_f is at odds with the prediction of the classic Fisher–KPP model, commonly used to describe growth-driven spreading, that the population spreads at a constant speed as a traveling wave[28,225]. Instead, our finding is consistent with the results of agent-based simulations of a growing population of jammed, incompressible cells[227], which also found $\nu \approx 0.5$ in the limit of fast nutrient consumption. In this case, front propagation *via* growth of the jammed population lags behind nutrient diffusion—leading to the diffusive scaling of X_f observed in our simulations as well as those of[227]. This difference with the prediction of the classic Fisher–KPP model suggests that the logistic form of growth used therein does not adequately describe jammed growth spreading. We are not aware of any experiments testing this prediction; performing such a study would be a valuable direction for future research.

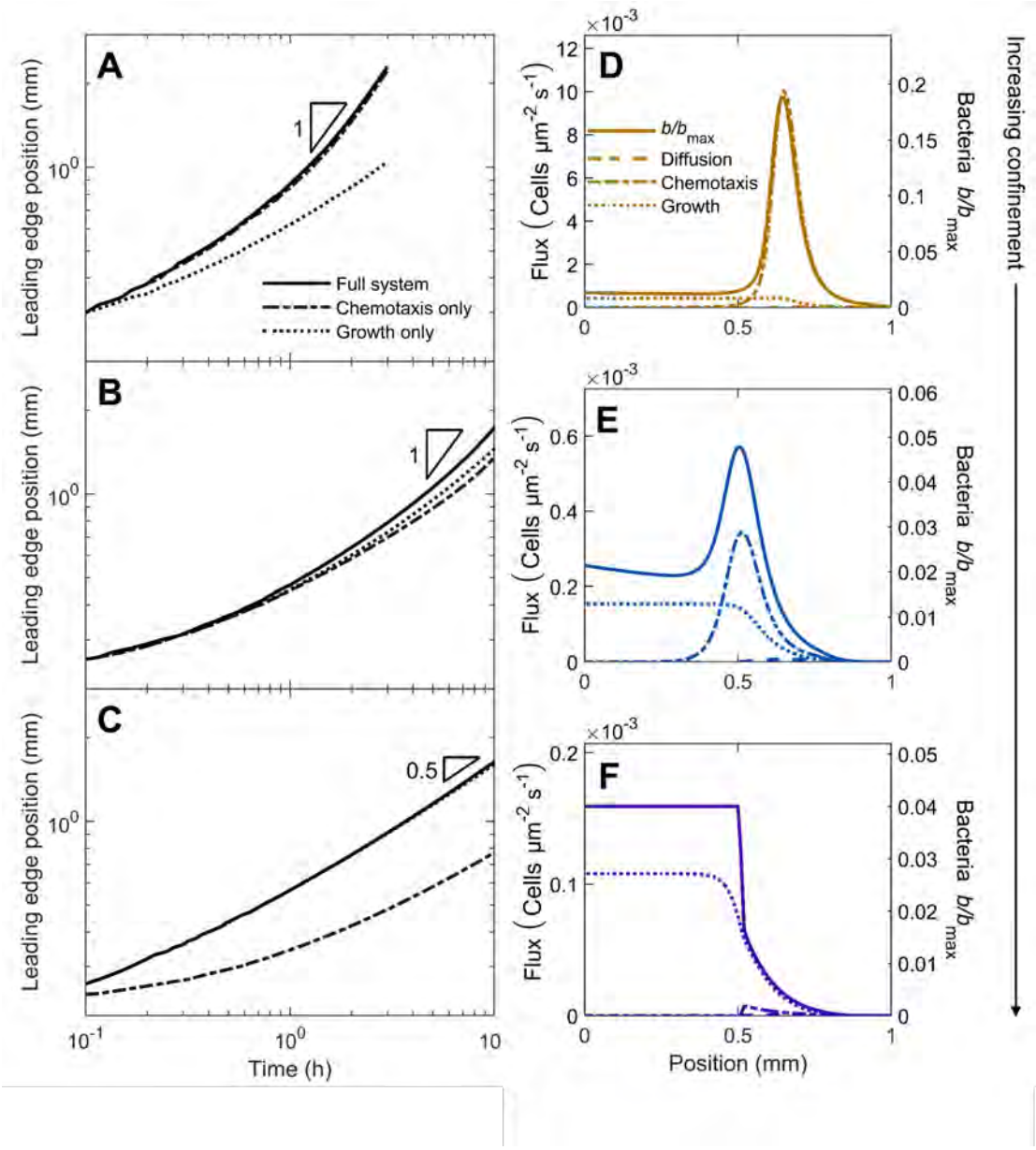

Figure 3.10: Population dynamics, morphology, and fluxes driving spreading for simulations of bacteria in weak, intermediate, and strong confinement (Fig. 3.9) as shown by the top, middle, and bottom rows, respectively. (A-B) Increase in the position of the leading edge of the population is initially hindered, but approaches constant-speed motion indicated by the triangle at long times. In strong confinement (C), however, the long-time behavior approaches diffusive-like scaling instead. (D-E) At long times, the population spreads as a coherent pulse (solid line) driven primarily by chemotaxis in weak confinement, and by both chemotaxis and growth in intermediate confinement. (F) In strong confinement, however, the population spreads slowly as a jammed front, driven primarily by growth.

This dominant role of growth in driving spreading in the case of strong confinement is expected from the smaller value of Λ; it is also corroborated by quantification of the different fluxes driving spreading (Fig. 3.10F). Removing growth or chemotaxis from the simulation provides a final confirmation of this point; the simulation without growth (Fig. 3.9F) yields a population that barely spreads, while that without chemotaxis (Fig. 3.9I) is nearly identical to that incorporating all factors (Fig. 3.9C)—also seen by comparing the different curves in Fig. 3.10C and F. Hence, growth-driven spreading dominates under stronger confinement, enabling the population to spread diffusively as a jammed front.

3.4 Conclusion

Ever since the discovery of bacteria over 300 years ago, lab studies of their spreading have typically focused on cells in unconfined environments such as in liquid cultures or near flat surfaces. However, in many real-world settings, bacteria must navigate complex and highly-confining environments. Thus, motivated by experimental observations of bacterial motility[38,39,45,163,233,234] and growth[235,236] in confined settings, in this paper, we have presented an extended version of the classic Keller-Segel model that incorporates the influence of confinement on bacterial spreading through both motility and growth. Versions of the Keller-Segel model describing cellular aggregation and pattern formation in response to *cell-generated* chemoattractant have in some cases considered cell density-dependent motility[224], but do not explicitly consider confinement, and do not also incorporate cellular growth. Moreover, to our knowledge, there is no version of the Keller-Segel model of bacterial spreading in response to *external* chemoattractant that treats the density- and confinement-dependence of motility in an experimentally-motivated manner, and also

incorporates cellular growth. The model described here provides a first step toward filling these gaps in knowledge, and in doing so, enabled us to examine the confinement-dependent interplay between motility-mediated and growth-mediated spreading.

In particular, our extended model treats cellular collisions with rigid surrounding obstacles, cellular collisions with each other, and growth-mediated spreading of jammed populations of cells. As such, it helps to bridge the classic Keller-Segel model of chemotactic spreading—which does not treat these effects and is therefore only appropriate to describe the spreading of dilute populations in unconfined settings—and models of growth-driven spreading (e.g.,[227,228,241])—which do not treat motility-based spreading and are therefore only appropriate to describe the spreading of highly-concentrated/confined and non-motile populations. Indeed, non-dimensionalizing our extended model revealed the parameter Λ that quantifies the confinement-mediated transition between chemotactic spreading (in weak confinement with $\Lambda \gtrsim 1$) and growth-driven spreading (in stronger confinement with $\Lambda < 1$). Our analysis also provided a straightforward way to estimate, in general, the relative contributions of chemotaxis and growth to the speed with which a population spreads.

While our prior experiments[163] motivated and helped to parameterize and validate the model used in this study, our prior work did not provide a full computational analysis of the vastly different confinement-dependent spreading behaviors encoded by the model, and how they can jointly influence bacterial population dynamics. Accomplishing this task was the central goal of the present manuscript. To this end, numerical simulations of the model enabled us to examine the implications of the confinement-mediated transition in behaviors for the full dynamics of bacterial spreading. As expected, in weak confinement, a dense inoculum of bacteria rapidly depletes nutrient locally, causing a coherent pulse of cells to

detach and continually propagate outward *via* chemotaxis—as predicted by the classic Keller-Segel model[26–29,35–37]. However, with increasing confinement, cellular crowding increasingly hinders both the initial formation of this pulse as well as its long-time propagation speed. Moreover, with increasing confinement, growth plays an increasingly dominant role in driving population spreading—eventually leading to a transition from fast chemotactic spreading to slow, growth-driven spreading of a jammed front[227]. Therefore, confinement is a key regulator of population spreading.

While chemotactic pulse propagation is well-characterized in unconfined settings[29,32–34], and conversely, jammed growth expansion has been investigated in some highly-confined settings[235,236], the interplay between these two behaviors has scarcely been studied. Hence, we anticipate that our numerical characterization of this confinement-mediated transition from chemotactic- to growth-driven spreading will help guide future experimental investigations of confined populations. Moreover, because our model describes spreading over large length and time scales, we expect it could help more accurately describe the spreading dynamics of bacteria in processes ranging from infections, drug delivery, agriculture, and bioremediation. To this end, it would be interesting to extend our one-dimensional simulations to higher dimensions, which could result in additional rich dynamics e.g., as recently explored in[243], and to media with spatially-varying confinement.

Our model represents a first step toward capturing the essential biophysical processes underlying these complex dynamics, and necessarily involved some simplifying assumptions and approximations. For example, based on recent experiments[163], we treated the influence of cell-cell collisions using a mean-field approach in which the transport parameters D_{b0} and χ_0 are truncated in a cell density-dependent manner; incorporating more sophisti-

cated collective dynamics[192–194,196] will be an important extension of our work. Similarly, we described jammed growth expansion by treating the population as an incompressible "fluid", similar to other models of growing immotile populations[227,239,240] and motivated by some experiments[235,236], implemented in a discrete manner. An alternate continuum description of growth could e.g., track the local growth velocity defined from the spatial gradient of a pressure field within the growing population that originates from cell growth. For the purposes of this paper, in which our central goal was to characterize the dynamics of population spreading, we needed to only track the motion of the outer boundary of the jammed region—which is readily accomplished using our discrete representation of growth expansion. Developing a more detailed treatment of these growth dynamics using either continuum or discrete approaches, such as by incorporating cellular deformations[227] and possible changes in cellular behavior that may result[244], will be a useful direction for future work. Furthermore, a simplifying assumption made in our model is that the solid obstacles that induce confinement are rigid and immovable; incorporating deformations of the surrounding medium will likely give rise to even more complex dynamics that will be interesting to study. Finally, while our model assumes that nutrient diffusion is unimpeded by the solid medium—which is likely to be the case in highly-permeable media such as biological gels and microporous clays/soils—incorporating hindered nutrient diffusion that may arise in other media will likely result in more complex dynamics that future extensions of our work could explore.

4

Chemotactic smoothing of collective migration

4.1 Introduction

Having used our model to explore the influence of confinement on outward (one-dimensional) motion in Chapters 2 and 3, we now apply the model to study shape change transverse to

the outward direction. Thus, we demonstrate a mechanism by which collectively migrating populations of *E. coli* autonomously smooth out large-scale perturbations in their overall morphology. We show that chemotaxis in response to a self-generated nutrient gradient provides both the driving force for collective migration and the primary smoothing mechanism for these bacterial populations. Using experiments on 3D printed populations with defined morphologies (performed by others in the lab), we characterize the dependence of this active smoothing on the wavelength of the perturbation and on the ability of cells to migrate. Furthermore, using continuum simulations, we show that the limited ability of cells to sense and respond to a nutrient gradient causes them to migrate at different velocities at different positions along a front—ultimately driving smoothing of the overall population and enabling continued collective migration. Our work thus reveals how cellular signal transduction enables a population to withstand large-scale perturbations, and provides a framework to predict and control chemotactic smoothing for active matter in general.

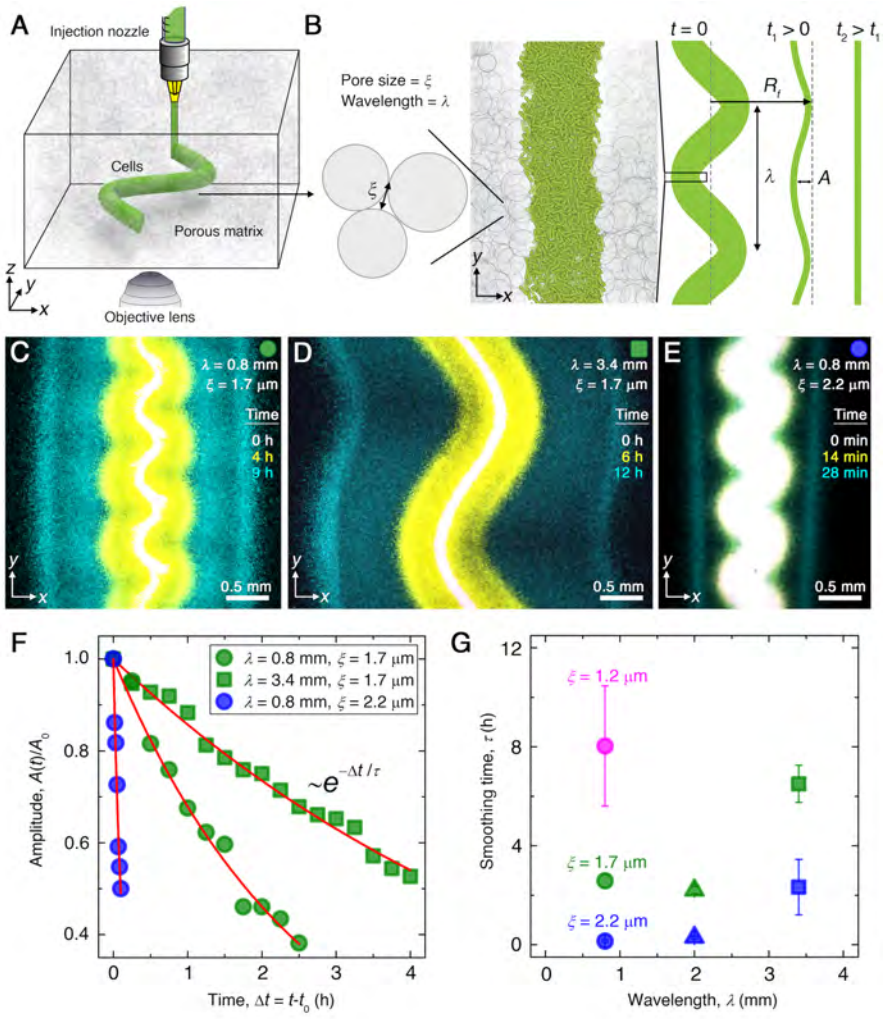

Figure 4.1: Experiments reveal that migrating *E. coli* populations autonomously smooth large-scale morphological perturbations. (A) Schematic of an undulated population (green cylinder) 3D-printed within a porous medium made of jammed hydrogel particles (gray). Each undulated cylinder requires ~ 10 s to print, two orders of magnitude shorter than the duration between successive 3D confocal image stacks, ~ 10 min. The surrounding medium fluidizes as cells are injected into the pore space, and then rapidly re-jams around the dense-packed cells. (B) Two-dimensional xy slice through the mid-plane of the population. The starting morphology of the 3D-printed population has undulation wavelength λ and amplitude A_0, as defined by the undulated path traced out by the injection nozzle. The cells subsequently swim through the pores between hydrogel particles, with mean pore size ξ. The population thereby migrates outward in a coherent front that eventually smooths; we track the radial position of the leading edge of the front R_f and the undulation amplitude A over time t. Caption continues on next page.

Figure 4.1: (C)-(E) Bottom-up (xy plane) projections of cellular fluorescence intensity measured using 3D confocal image stacks. Images show sections of three initially undulated populations in three different porous media, each at three different times (superimposed white, yellow, cyan), as the cells migrate radially outward. A pixel corresponds to ~ 1 cell, and the images only show a magnified view of the overall population. Panels (C)-(D) demonstrate the influence of varying the undulation wavelength, keeping the mean pore size the same; increasing λ slows smoothing. Panels (C) and (E) demonstrate the influence of varying the pore size, keeping the undulation wavelength the same; increasing ξ hastens smoothing. (F) For each experiment shown in (C)-(E), the undulation amplitude A, normalized by its initial value A_0, decays exponentially with the time Δt elapsed from the initiation of smoothing at $t = t_0$. Fitting the data (symbols) with an exponential decay (red lines) yields the smoothing time τ for each experiment. (G) Smoothing time τ measured in experiments increases with increasing undulation wavelength λ and decreasing medium mean pore size ξ, which enables cells to migrate more easily. Error bars reflect the uncertainty in determining the initiation time t_0 from the exponential fit of the data.

4.2 Results

4.2.1 Chemotactic smoothing is regulated by perturbation wavelength and cellular motility

As previously described in Chapter 2, to experimentally investigate the collective migration of *E. coli* populations, we confine them within porous media of tunable properties[38,39,163] consisting of hydrogel packings (Fig. 4.1A–B). A key feature of the hydrogel packings is that they are yield-stress solids; thus, an injection micronozzle can move along a prescribed path inside each medium by locally rearranging the particles, gently extruding densely-packed cells into the interstitial space (Fig. 4.1A–B). The particles then rapidly re-densify around the newly-introduced cells, re-forming a jammed solid matrix that supports the cells in place with minimal alteration to the overall pore structure[164–166]. This approach is there-

This chapter has been adapted from "Chemotactic smoothing of collective migration", by Tapomoy Bhattacharjee*, **Daniel B. Amchin***, Ricard Alert*, Jenna A. Ott, and Sujit S Datta, *eLife* 11, 71226 (2022) *Equal contribution. **Author Contributions:** T.B. and S.S.D. designed the experiments; T.B. performed all experiments with assistance from J.A.O.; D.B.A., J.A.O., and S.S.D. designed the numerical simulations; D.B.A. performed all numerical simulations with assistance from J.A.O.; R.A. performed all theoretical calculations through discussions with S.S.D.; T.B., D.B.A., R.A., and S.S.D. analyzed the data; S.S.D. designed and supervised the overall project. All authors discussed the results and implications and wrote the manuscript.

fore a form of 3D printing that enables the initial morphology of each bacterial population to be defined within the porous medium. The cells subsequently swim through the pores between particles, migrating outward through the pore space. For example, as we showed previously in Chapter 2 [163], cells of *E. coli* initially 3D printed in densely-packed straight cylinders collectively migrate radially outward in smooth ("flat"), coherent fronts. These fronts form and propagate *via* chemotaxis: the cells continually consume surrounding nutrient, generating a local gradient that they in turn bias their motion along [28,29,33,34,245]. As each front of cells migrates, it propagates the local nutrient gradient with it through continued consumption, thereby sustaining collective migration. In the absence of nutrient, migrating fronts do not form at all [163].

To test how perturbations in the overall morphology of the population influence its subsequent migration, other members of our lab 3D-print densely-packed *E. coli* in 1 cm-long cylinders with spatially-periodic undulations as perturbations prescribed along the x direction (Fig. 4.1B). Each population is embedded deep within a defined porous medium; an initial population morphology is schematized at time $t = 0$ in Fig. 4.1B, with the undulation wavelength and amplitude denoted by λ and A, respectively. An experimental realization with $A(t = 0) \approx 300\,\mu$m, $\lambda \approx 0.8$ mm, and $\xi = 1.7\,\mu$m is shown in white in Fig. 4.1C, which shows an xy cross section through the midplane of the population. After 3D printing, the outer periphery of the population spreads slowly, hindered by cell-cell collisions in the pore space, as the population establishes a steep gradient of nutrient through consumption [163]. Then, this periphery spontaneously organizes into a $\sim$ 300 μm-wide front of cells that collectively migrates outward (yellow in Fig. 4.1C). The undulated morphology of this front initially retains that of the initial population. Strikingly, however, the

front autonomously smooths out these large-scale undulations as it continues to propagate. We characterize this behavior by tracking the decay of the undulation amplitude, normalized by its initial value $A_0 \equiv A(\Delta t = 0)$, as a function of time elapsed from the initiation of smoothing, Δt (green circles in Fig. 4.1F). The normalized amplitude decays exponentially (red line in Fig. 4.1F), with a characteristic time scale $\tau \approx 2.5$ h, and the population eventually continues to migrate as a completely flat front (cyan in Fig. 4.1C).

We observe similar behavior when the wavelength λ is increased to 3.4 mm (Fig. 4.1D) or when the pore size ξ is increased to 2.2 μm (Fig. 4.1E); however, the dynamics of front smoothing are altered in both cases. Specifically, increasing the undulation wavelength slows smoothing, increasing τ by a factor of ≈ 3 to reach $\tau \approx 6.5$ h (green squares in Fig. 4.1F). Conversely, increasing the pore size—which enables cells to migrate through the pore space more easily—greatly hastens smoothing, decreasing τ by more than a factor of ≈ 10 to become $\tau \approx 0.2$ h (blue circles in Fig. 4.1F). This behavior is consistent across multiple experiments with varying λ and ξ, as summarized in Fig. 4.1G. Our experiments thus indicate that the smoothing of collective migration is regulated by both the undulation wavelength and the ease with which cells migrate.

4.2.2 A continuum model of chemotactic migration recapitulates the spatiotemporal features of smoothing

Here, to simulate the chemotactic migration of populations with large-amplitude perturbations, we numerically solve the same continuum model as in Chapter 2, but now in 2D using undulated morphologies as initial conditions for b as described in §4.4.1. Although we do not expect perfect quantitative agreement between the experiments and simulations

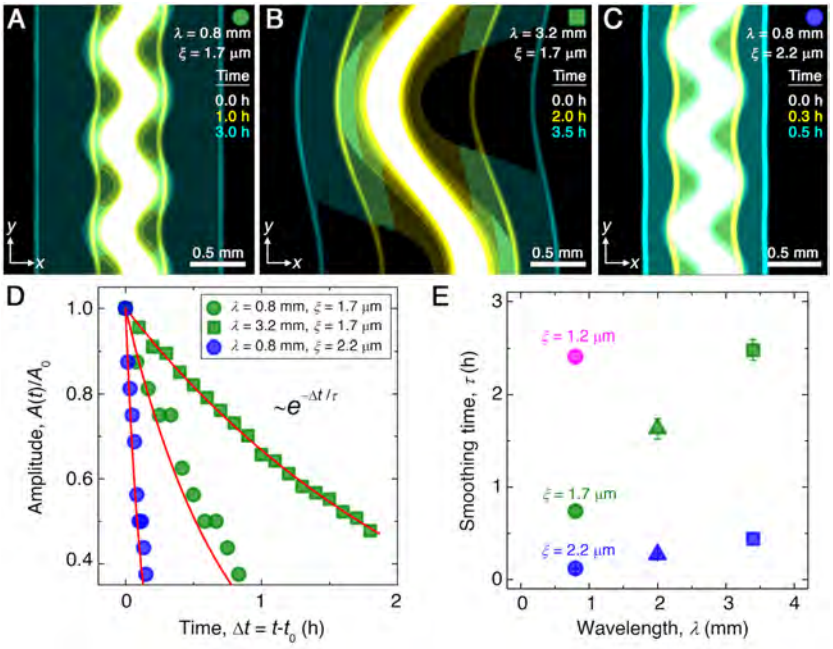

Figure 4.2: Continuum model captures the essential features of the smoothing of migrating bacterial populations. (A)-(C) Simulations corresponding to experiments reported in Fig. 4.1C–E, respectively, performed by numerically solving Eqs. 2.2-2.3 in two dimensions (xy plane). Images show the calculated cellular signal (details in §4.4) for three initially undulated populations in three different porous media, each at three different times (superimposed white, yellow, cyan), as the cells migrate outward. Panels (A)-(B) demonstrate the influence of varying the undulation wavelength, keeping the mean pore size the same; as in the experiments, increasing λ slows smoothing. Panels (A) and (C) demonstrate the influence of varying the pore size, keeping the undulation wavelength the same; as in the experiments, increasing ξ, incorporated in the model by using larger values of the diffusion and chemotactic coefficients as obtained directly from experiments, hastens smoothing. (D) For each simulation shown in (A)-(C), the undulation amplitude A,normalized by its initial value A_0, decays exponentially with the time Δt elapsed from the initiation of smoothing at $t = t_0$ as in the experiments. Fitting the data (symbols) with an exponential decay (red lines) again yields the smoothing time τ for each simulation. (E) Smoothing time τ obtained from the simulations increases with increasing undulation wavelength λ and decreasing medium mean pore size ξ, as in the experiments. Error bars reflect the uncertainty in determining the initiation time t_0 from the exponential fit of the data.

due to their difference in dimensionality and the simplified treatment of cell-cell interactions, the simulated fronts form, collectively migrate, and smooth in a manner that is remarkably similar to the experiments. Three examples are shown in Fig. 4.2C to 4.2E, corresponding to the experiments shown in Fig. 4.1C to 4.1E. Similar to the experiments, the outer periphery of each population first spreads slowly, then spontaneously organizes into an outward-migrating front that eventually smooths. We again find that the normalized undulation amplitude decays exponentially over time, as shown in Fig. 4.2D. As in the experiments, increasing the undulation wavelength λ slows smoothing; compare Fig. 4.2B to Fig. 4.2A. Also as in the experiments, increasing the pore size ξ, which increases the migration parameters D_b and χ, greatly hastens smoothing; compare Fig. 4.2C to Fig. 4.2A. This variation of the smoothing time scale τ obtained from simulations with λ and ξ is summarized in Fig. 4.2E. We observe the same behavior as in the experiments, with the absolute values of τ agreeing to within a factor of ~ 3. This agreement confirms that the continuum Keller-Segel model recapitulates the essential spatio-temporal features of smoothing seen in the experiments.

4.2.3 Chemotaxis is the primary driver of front smoothing

The simulations provide a way to directly assess the relative importance of cellular diffusion, chemotaxis, and cell proliferation to front smoothing. To this end, we perform the same simulation as in Fig. 4.2A, but with each of the corresponding three terms in Eq. 2.3 knocked out, and determine the resulting impact on collective migration. This procedure enables us to determine the factors necessary for smoothing.

While diffusion typically causes spatial inhomogeneities to smooth out, we do not expect

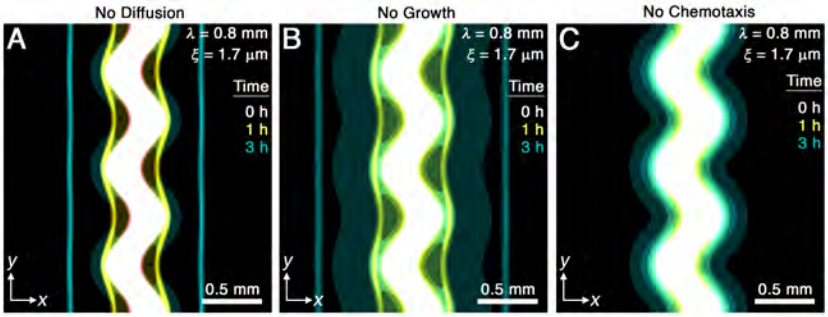

Figure 4.3: Chemotaxis is the primary driver of morphological smoothing. Images show the same simulation as in Fig. 4.2A, which serves as an exemplary case, but with either (A) diffusive cell motion, (B) cell proliferation, or (C) cell chemotaxis knocked out by setting the diffusivity D_b, proliferation rate γ, or chemotactic coefficient χ to zero, respectively. Simulated bacterial fronts lacking diffusion or proliferation still smooth, as shown in (A)-(B), but simulated fronts lacking chemotaxis do not smooth, as shown in (C)—demonstrating that chemotaxis is necessary and sufficient for the observed morphological smoothing.

it to play an appreciable role in the front smoothing observed here: the characteristic time scale over which undulations of wavelength $\lambda \approx 1$ mm diffusively smooth is $\sim \lambda^2/D_b \approx$ 100 to 700 h, up to three orders of magnitude larger than the smoothing time τ measured in experiments and simulations. We therefore expect that the undirected motion of bacteria is much too slow to contribute to front smoothing. The simulations for $\lambda = 0.8$ mm and $\xi = 1.7$ μm confirm this expectation: setting $D_b = 0$ yields fronts that still smooth over a time scale $\tau \sim 1$ h similar to the full simulations (Fig. 4.3A).

Another possible mechanism of front smoothing is differences in bacterial proliferation at different locations along the front periphery—for example, the front would smooth if cells in concave regions were able to proliferate faster than those in convex regions. However, differential proliferation typically destabilizes bacterial communities, as shown previously both experimentally and theoretically[246–251]. Furthermore, even if proliferation were to help smooth the overall population, we again expect this hypothetical mechanism to be too slow to appreciably contribute: the shortest time scale over which cells all grow-

ing exponentially at a maximal rate $\gamma \sim 1\,\mathrm{h}^{-1}$ spread over the length scale $A_0 \approx 300\,\mu\mathrm{m}$ by growing end-to-end is $\gamma^{-1}\log_2(A_0/d) \sim 7$ h, where $d \approx 2\,\mu\mathrm{m}$ is the cell body length for *E. coli*. This time scale is over an order of magnitude larger than the τ measured in experiments and simulations. The simulations again confirm our expectation: setting $\gamma = 0$ yields fronts that still smooth over a time scale $\tau \sim 1$ h similar to the full simulations (Fig. 4.3B).

These findings leave chemotaxis as the remaining possible mechanism of front smoothing. The simulations confirm this expectation: setting $\chi = 0$ yields a population that slowly spreads *via* diffusion and proliferation, but that does not form collectively migrating fronts at all (Fig. 4.3C). Therefore, chemotaxis is both necessary and sufficient for the observed front smoothing.

4.2.4 Distinct modes by which chemotaxis impacts front morphology

How exactly does chemotaxis smooth bacterial fronts? To address this question, we examine the spatially-varying chemotactic velocity $v_c = \chi\nabla f(c)$, which quantifies how rapidly different regions of the population migrate *via* chemotaxis. To gain intuition for the determinants of v_c, we recast this expression in terms of the nutrient gradient:

$$v_c = \underbrace{\chi f'(c)}_{\text{Response function}}\ \underbrace{\nabla c}_{\text{Forcing}}. \tag{4.1}$$

As in linear response theory, the chemotactic velocity can be viewed as the bacterial response to the driving force given by the nutrient gradient, ∇c, modulated by the chemotactic response function $\chi f'(c)$. Thus, variations in chemotactic velocity along the leading edge of the front, which specify how the overall front morphology evolves, are determined

by the combined effect of variations in the nutrient gradient and the chemotactic response function. We therefore examine each of these modes by which chemotaxis influences front morphology in turn.

We first consider the nutrient gradient, which is the typical focus of chemotaxis studies. Our simulations, which numerically solve the coupled system of Eqs. 2.2-2.3, directly yield the spatially-varying nutrient field c and therefore ∇c. A snapshot from the representative example of Fig. 4.2A is shown in Fig. 4.4A, with the contours of $c = c_-$ and $c = c_+$ indicated by the cyan and magenta lines, respectively. The contours are spaced closer at the convex "peaks" (e.g., at $y/\lambda = 0.5$) than at the concave "valleys" (e.g., at $y/\lambda = 0$) along the leading edge of the front. Thus, the magnitude of the driving force given by ∇c is larger at the peaks. We confirm this expectation by directly quantifying the nutrient gradient along the leading edge, focusing on the component $\partial_x c$ in the overall front propagation direction (x) for simplicity, as shown by the orange symbols in Fig. 4.4C; as expected, this driving force is stronger at the peaks. This spatial variation in the driving force promotes faster outward chemotactic migration at the peaks than at the valleys, amplifying front undulations—in opposition to our observation that the migrating population self-smooths. Variations in the local nutrient gradient along the leading edge of the front do not contribute to smoothing; rather, they oppose it.

We next turn to the chemotactic response function, which characterizes cellular signal transduction. Because χ is a constant for each porous medium [163], spatial variations in the response function are set by variations in $f'(c)$. The sensing function $f(c)$ is plotted in the upper panel of Fig. 4.4B. It varies linearly as $\sim c\,(1/c_- - 1/c_+)$ for $c \ll c_-$ and saturates at $\log(c_+/c_-)$ for $c \gg c_+$; the characteristic concentrations c_- and c_+ represent the dissocia-

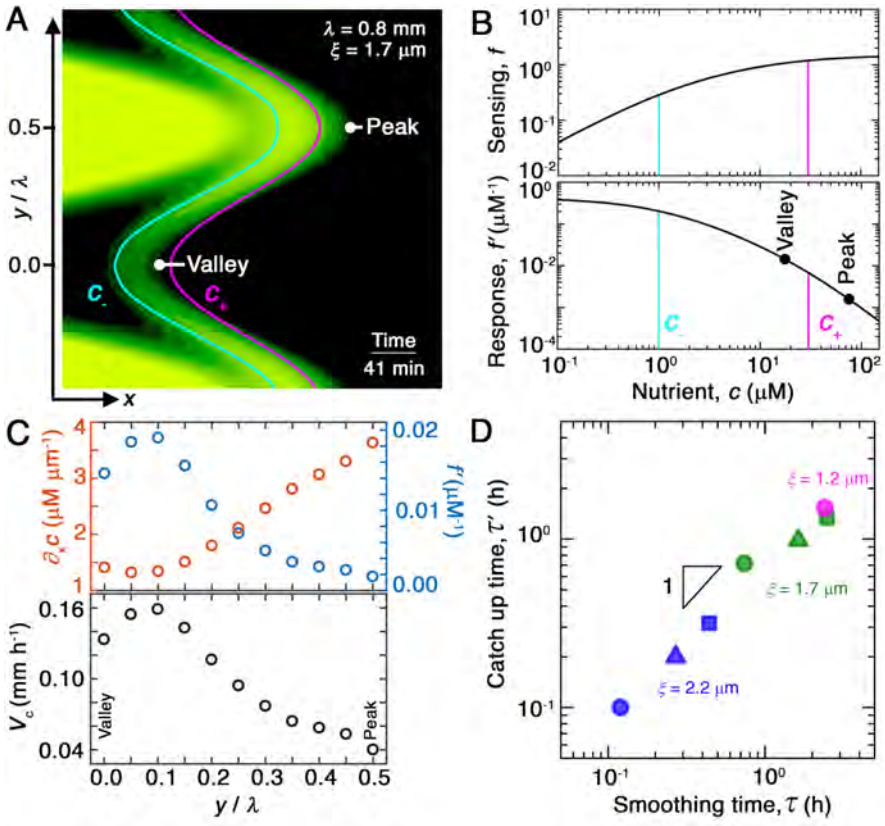

Figure 4.4: Chemotaxis alters the morphology of migrating bacterial fronts in two distinct ways. (A) Magnified view of a migrating bacterial front from the simulation shown in Fig. 4.2A at time $t = 41$ min as a representative example. To illustrate the spatially-varying nutrient levels, we show the contours of constant nutrient concentration $c = c_+$ and $c = c_-$ in magenta and cyan, respectively; these represent characteristic upper and lower limits of sensing. The contours are spaced closer at the leading edge of the convex peak ($y/\lambda = 0.5$) than the concave valley ($y/\lambda = 0$), indicating that the magnitude of the local nutrient gradient is larger at peaks than at valleys. The nutrient concentration itself, which increases monotonically with increasing x, is also larger at the peak than at the valley. (B) Top and bottom panels show the variation of the nutrient sensing function $f(c)$ and chemotactic response function $f'(c)$, respectively, with nutrient concentration c. Because sensing saturates at high nutrient concentrations, chemotactic response is weaker at higher c (peaks) than at lower c (valleys). (C) Top panel shows the x component of the nutrient gradient $\partial_x c$ (red, left axis) and the response function f' (blue, right axis), and bottom panel shows the x component of the chemotactic velocity $v_{c,x} = \chi f' \partial_x c$ computed from these quantities, evaluated at different lateral positions y along the leading edge of the front in (A). While the driving force of chemotaxis represented by $\partial_x c$ is smaller at the valley, the chemotactic response $\chi f'$ is larger at the valley and dominates in setting $v_{c,x}$: valleys move out faster than peaks, eventually catching up to them and smoothing out the undulations. (D) For all simulations (Fig. 4.2E), the smoothing time τ determined by analyzing the decay of large-scale undulations (Fig. 4.2D) is similar to the time τ' needed for valleys to catch up to peaks estimated using their different x-component chemotactic velocities. Note that we do not expect an exact match between τ and τ' as they are related yet different quantities.

tion constants of the nutrient for the inactive and active conformations of the cell-surface receptors, respectively[28–31]. The response function $\chi f'(c)$ therefore decreases strongly as c increases above c_+, which accordingly is often referred to as an upper limit of sensing (Fig. 4.4B, lower panel). That is, because high nutrient concentrations saturate cell-surface receptors, the chemotactic response function decreases with nutrient concentration. Inspection of the nutrient field indicates that nutrient concentrations are larger at the peaks than at the valleys along the leading edge of the front (Fig. 4.4A). Thus, the chemotactic response of cells is weaker at peaks than at valleys, as shown by the points in Fig. 4.4B, yielding slower outward chemotactic migration at peaks than at valleys and thereby reducing the amplitude of front undulations. Variations in the chemotactic response along the leading edge of the front promote smoothing, unlike variations in the nutrient gradient.

4.2.5 Spatial variations in chemotactic response drive morphological smoothing

We therefore hypothesize that the stabilizing effect of the chemotactic response (Fig. 4.4C, blue) dominates over the destabilizing influence of the nutrient gradient (Fig. 4.4C, red), leading to smoothing. Computation of the spatially-varying chemotactic velocity at the leading edge of the front using Eq. 4.1, focusing on the x velocity component $v_{c,x} \approx \chi f' \partial_x c$ for simplicity, supports this hypothesis: cells at concave regions migrate outward faster than those at convex regions (Fig. 4.4C, lower panel). To further test this hypothesis, we assess the influence of varying c_+; we expect that reducing this upper limit weakens chemotactic response not just at the peaks, but also the valleys, thereby slowing smoothing. While tuning solely c_+ is challenging in the experiments, this can be readily done in the simulation—

yielding slower smoothing, as expected (Fig. 4.5).

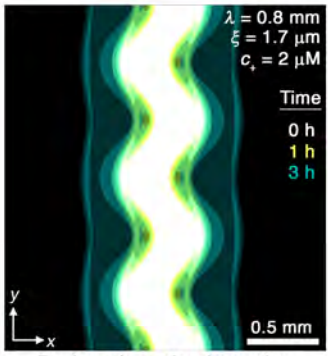

Figure 4.5: Effect of reduced sensing. To investigate the influence of varying the upper limit of sensing c_+, we repeat the simulation for the prototypical case of $\xi = 1.7$ μm and $\lambda = 0.8$ mm but with c_+ lowered by a factor of 15. Consistent with our expectation, we find that reducing this upper limit weakens chemotactic response not just at the peaks, but also the valleys, thereby slowing smoothing. Image is presented as in Fig. 4.2A.

As a final test of our hypothesis, for each simulation shown in Fig. 4.2, we determine the difference between the chemotactic velocities of the valleys and peaks, approximated by $\Delta v_{c,x} \approx \chi[(f'\partial_x c)_{\text{valley}} - (f'\partial_x c)_{\text{peak}}]$, as a function of time Δt. If smoothing is indeed due to variations of the chemotactic velocity along the leading edge, then the smoothing time τ determined by analyzing the decay of the undulation amplitude, $A = A_0 e^{-\Delta t/\tau}$ (Fig. 4.2D-E), should be similar to the time τ' at which valleys catch up to peaks, i.e., $\int_0^{\tau'} \Delta v_{c,x}\, \mathrm{d}\Delta t \approx A_0$. To test this expectation, we plot the τ' values thus obtained for all of our simulations of varying λ and ξ as a function of the corresponding τ, as shown in Fig. 4.4D. We find that τ' and τ are indeed similar to one another in all cases—confirming that smoothing is determined by spatial variations in chemotactic velocity.

4.3 Conclusion

By combining experiments and simulations, this study elucidates a mechanism by which collectively migrating populations can smooth out large-scale perturbations in their overall morphology. We focus on the canonical example of chemotactic migration, in which coherent fronts of cells move in response to a self-generated nutrient gradient. The smoothing of these fronts underlies the utility of standard agar-based assays for chemotaxis, in which bacteria spread outward in smooth, circular rings from a dense inoculum[28,44,45,252]—despite the presence of irregularities in the initial inoculum that are inevitably introduced by human error. To our knowledge, the robustness of the front morphology to such perturbations has never been examined or quantitatively explained; as a result, previous studies have only focused on the migration of the smooth fronts that ultimately result[26–29,33,34,163,245]. Our work now provides an explanation for why perturbed fronts smooth out. It therefore provides a counterpoint to previous studies investigating the ability of perturbations to instead disrupt collective migration[40–43,48–50,52,53,55–69]. It also complements recent theoretical work describing how chemotaxis can stabilize the hydrodynamic instabilities that arise in unconfined populations of self-propelled particles[253].

The 3D printing platform provides a unique way to tune the shape of the initial perturbation, as well as the extent to which cellular migration is hindered. The experiments performed by others in the lab using this approach reveal that the dynamics of smoothing are regulated by both the undulation wavelength and the ease with which cells migrate. The continuum simulations recapitulate the essential features of this behavior and shed light on the underlying mechanism. We find that even though cells in peaks of an undulated front

experience a stronger driving force given by the local nutrient gradient, the higher nutrient levels they are exposed to saturate their cell-surface receptors, and hence they exhibit a weaker chemotactic response than cells in valleys. That is, while variations in the nutrient gradient along the leading edge of a front act to amplify undulations, variations in the ability of cells to sense and respond to this gradient dominate and instead smooth out the undulation. Importantly, this mechanism of smoothing is distinct from diffusion, which is typically responsible for the smoothing of traveling waves in reaction-diffusion systems—and in our case, is much too slow to drive smoothing.

4.3.1 Conditions for chemotactic smoothing to arise

While our study utilizes a specific form of the sensing function $f(c)$ established for *E. coli*[28,29], the phenomenon of chemotactic smoothing can manifest more generally. Specifically, our description of smoothing requires that (i) convex regions of a population are exposed to more nutrient c than concave regions, and (ii) $f(c)$ is monotonically increasing and concave, with $f''(c) < 0$; when these conditions are satisfied, the chemotactic response is weaker at convex regions than at concave ones, thereby promoting smoothing (as indicated in Fig. 4.4B).

The first requirement is frequently satisfied for collective migration in general; for example, in chemotactic migration, nutrient concentration c decreases from the outward boundaries into the population over a length scale given by the interplay between nutrient diffusion and consumption. This first requirement is also satisfied by many other forms of active matter that rely on other modes of sensing to collectively migrate, for which c would

generically represent the stimulus being sensed. Documented examples include durotactic cell groups[254–256], phoretic active colloids[257–259], and phototactic robots[186,260]—systems for which migration is directed toward regions of larger c, and therefore convex regions are more likely to be exposed to larger c.

The second requirement is also satisfied for diverse active matter systems; in the context of chemotaxis, specific examples include other bacteria[203], enzymes[187,261,262], aggregating amoeba cells[198], and mammalian cell groups during development, immune response, and disease[46,185,263–267]. This second requirement is again also satisfied for active matter that collectively migrates using other sensing mechanisms, for which sensing has been documented to increase and eventually saturate with the stimulus, be it the stiffness of the underlying surface[254–256], temperature[257–259], or light intensity[186,260]. Thus, exploring the physics described here in diverse other forms of active matter will be a useful direction for future work.

As a final illustration of the necessity of the sensing function $f(c)$ to be concave, $f''(c) < 0$, we repeat our analysis but instead consider a strictly linear $f(c) = c/c_{\text{lin}}$, which does not saturate. We choose $c_{\text{lin}} = (1/c_- - 1/c_+)^{-1}$ so that the linear $f(c)$ matches our original logarithmic $f(c)$ at small c. With this linear sensing function, the chemotactic response is independent of concentration, $f'(c) = 1/c_{\text{lin}}$, and the condition of concavity is violated: $f''(c) = 0$. We therefore expect chemotactic smoothing to not occur. Consistent with our expectation, repeating the analysis underlying Fig. 4.4C but for the strictly linear $f(c)$ yields fronts for which valleys no longer move faster than peaks. Instead, as shown in Fig. 4.6, the profile of chemotactic velocity is now inverted with respect to that of the bottom panel in Fig. 4.4C. Hence, the front does not smooth. Overall, this sample computation illustrates

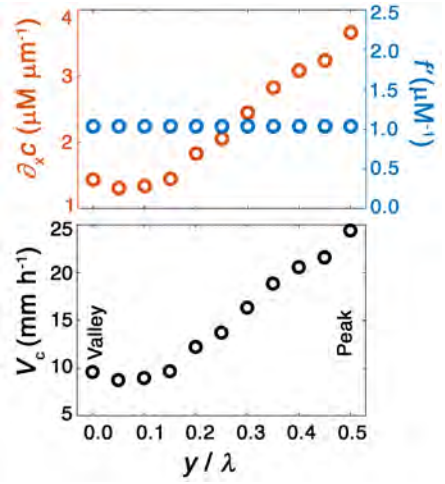

Figure 4.6: Chemotactic smoothing requires a concave sensing function $f(c)$. To illustrate the necessity of a concave sensing function with $f''(c) < 0$ for chemotactic smoothing, we repeat our analysis but for a strictly linear $f(c) = c/c_{\text{lin}}$ with $c_{\text{lin}} = (1/c_- - 1/c_+)^{-1}$. In this case, the condition of concavity is violated: $f''(c) = 0$. We therefore expect chemotactic smoothing to not occur. Top panel shows the x component of the nutrient gradient $\partial_x c$ (red, left axis) and the response function f' (blue, right axis), and bottom panel shows the x component of the chemotactic velocity $v_{c,x} = \chi f' \partial_x c$ computed from these quantities, evaluated at different lateral positions y along the leading edge of the front for this case of a strictly linear sensing function. In this case, we find that the valleys no longer move faster than peaks—consistent with our expectation.

a way of modifying $f(c)$ that abrogates sensing saturation and hence would prevent chemotactic smoothing.

4.3.2 Broader implications of chemotactic smoothing

The chemotactic smoothing process described here is autonomous, arising without any external intervention. Instead, it is a population-scale consequence of the limitations in cellular signal transduction—motivating future studies of other population-scale effects, beyond smoothing, that may emerge from individual behaviors. Indeed, while studies of chemotaxis typically focus on the role of the external nutrient gradient in driving cellular migration, our work highlights the distinct and pivotal role played by the cellular chemo-

tactic response function in regulating migration and large-scale population morphology more broadly. Our work therefore contributes a new factor to be considered in descriptions of morphogenesis, which thus far have focused on the role of other factors—such as differential forcing by signaling gradients, differential proliferation, intercellular mechanics, substrate interactions, and osmotic stresses[246–251,264,268–275]—in regulating the overall morphology of cellular communities and active matter in general.

4.4 Methods

4.4.1 Implementation of numerical simulations

The details of the model given in §2.4.2 also apply to Chapter 4. We now highlight the changes made to the model described in §2.4.3 to accommodate the modified geometry of the system. While the experimental geometry of undulating patterns in Chapter 4 is three dimensional, in Chapter 2, we found that radial and out of plane effects do not need to be considered to capture the essential features of bacterial front formation and migration. Thus, for simplicity, we use a 2D representation. In the x direction (coordinates defined in Figs. 4.2 and 4.4), no flux boundary conditions are used at the walls of the simulated region for both field variables b and c. In the y direction, no flux boundary conditions are used after one wavelength of the undulation, peak to peak, which comprises a single repeatable unit. The initial cylindrical distribution of cells 3D printed in the experiments has a diameter of $\sim$ 100 μm; so, in the x dimension of the numerical simulations, we use a Gaussian with a 100 μm full width at half maximum for the initial bacteria distribution $b(x, t = 0)$, with a peak value that matches the 3D printed cell density in the experiments, 0.95×10^{12} cells/mL. We vary the center x position of the Gaussian distribution sinusoidally along y

to reproduce a given experimental wavelength and amplitude. Experimental wavelengths were measured directly from confocal images and rounded to the nearest 10 μm. The initial condition of nutrient is $c = 10$ mM everywhere, characteristic of the liquid media used in the experiments. The initial nutrient concentration is likely lower within the experimental population initially due to nutrient consumption during the 3D printing process; however, we expect this discrepancy to play a negligible role as nutrient deprivation occurs rapidly in the simulations.

For the first and second derivatives in space, we use finite difference equations with central difference forms in 2D. Time steps of the simulations are 0.01 s and spatial resolution is 10 μm. Because the experimental chambers are 3.5 cm in diameter, we use a distance of 3.5×10^4 μm for the size of the entire simulated system in the x direction with the cells initially situated in the center. Our previous work [163] demonstrated that the choice of discretization does not appreciably influence the results in numerical simulations of flat fronts; furthermore, our new results for the simulations performed here (Fig. 4.7) indicate that our choice of discretization used is sufficiently finely-resolved such that the results in numerical simulations of undulated fronts are not appreciably influenced by discretization.

4.4.2 Characterizing simulated front dynamics

For the analysis shown in Fig. 4.2, the leading edge is defined as the locus of positions at which b falls below a threshold value equal to 10^{-4} times the maximum cell density of the initial bacterial distribution, as in [163]. For the analysis shown in Fig. 4.4, to more accurately track the leading edge of the front, we define it as the locus of positions at which b falls below a threshold value specific to each condition tested; the threshold is 0.003 cells per

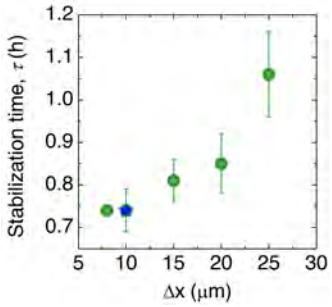

Figure 4.7: Convergence of the numerical simulations. To assess the influence of discretization, we repeat the simulation for the prototypical case of $\xi = 1.7$ μm and $\lambda = 0.8$ mm with different choices of the spatial discretization Δx and measure the smoothing time τ. In all cases we find qualitatively similar results, although the dynamics vary; however, as shown by the green data points, the dynamics do not appreciably change for discretization smaller than ≈ 10 μm, which is the value used in the main text simulations, as indicated by the blue star.

μm^3 for the prototypical case of $\xi = 1.7$ μm and $\lambda = 0.8$ mm shown in Fig. 4.4A-C, as well as all simulations for $\xi = 2.2$ μm; 0.002 cells per μm^3 for simulations for $\xi = 1.7$ μm and $\lambda = 2.0$ and 3.2 mm; and 0.001 cells per μm^3 for simulations for $\xi = 1.2$ μm and $\lambda = 0.8$ mm. We note that the b-dependence of the motility parameters D_b and χ does not play an appreciable role in our analysis of smoothing, since the definition used for the leading edge of each front is at a fixed, low value of b.

4.4.3 Robustness of front smoothing

One may speculate that smoothing could be avoided or even reversed by lowering the initial nutrient concentration to a value in between c_+ and c_-, thereby diminishing the difference in chemotactic response between peaks and valleys and allowing the amplifying effects of the nutrient gradient to dominate. However, a simulation performed with a much lower initial nutrient concentration of 10 μM throughout, chosen to be in between c_+ and c_-, does not even form a traveling front at all over the experimental time scale (Movie S7 in

the online version of[243]). This absence of a front is due to the reduction in nutrient consumption as modulated by the Monod function $g(c)$, which results in a drastic reduction in the nutrient gradient that drives front formation and propagation. Thus, despite varying the initial nutrient concentration over three orders of magnitude, the upper limit c_+ over an order of magnitude, and the migration parameters D_b and χ over an order of magnitude, we have not found conditions under which chemotactic fronts, if they form, do not smooth. Smoothing therefore appears to be robust to large changes in the environmental conditions.

5

Microbial mutualism generates multistable and oscillatory growth dynamics

5.1 Introduction

Chapters 2-4 described the growth and motility of a single bacterial population in response to chemical gradients formed by that same population. However, as described in Chapter

1, one bacterial population often interacts with another through their shared chemical environment. Although these interactions are often mutually beneficial, simple models for describing experimentally observed non-linear phenomena in such systems are lacking. As detailed in Chapter 1, these phenomena include bistability and oscillations in the growth dynamics of two species systems. Below, we formulate a minimal model that captures the essential features of mutualistic metabolic coupling that can produce both bistability and oscillations under conditions similar to the experimental works previously mentioned[71,96]. We extract useful nondimensional parameters from our model and solve the steady state form of the system of equations, allowing us to map out the state space of input conditions where both cell types can or cannot coexist. By doing so, we identify what role metabolic sharing plays in determining the boundaries of these regimes within the state space. Thus, our results help to provide quantitative and generalizable principles to guide future work studying microbial mutualists.

5.2 Methods

5.2.1 Development of the governing equations

As an illustrative and well-characterized[71,72,96,158] example, we consider the model two-species microbial community schematized in Fig. 5.1a(ii). This community is a mixture of aerobes (red in Fig. 5.1) and anaerobes (dark blue), whose metabolism and growth are

This chapter has been adapted from "Microbial mutualism generates multistable and oscillatory growth dynamics", by **Daniel B. Amchin**, Alejandro Martínez-Calvo, and Sujit S. Datta, submitted, *Biophysical Journal* (2022). **Author Contributions:** D.B.A. and S.S.D. designed the model; D.B.A. and S.S.D. designed the numerical simulations and theoretical analysis; D.B.A. performed all numerical simulations and theoretical analysis; D.B.A., A.M., and S.S.D. analyzed the data; S.S.D. designed and supervised the overall project. D.B.A. and S.S.D. discussed the results and implications and wrote the manuscript.

either promoted or instead suppressed in oxygenated environments, respectively. The bacteria are described by a number concentration b with subscripts $_{\text{aer}}$ and $_{\text{an}}$ for aerobes and anaerobes, respectively. Genome sequencing and metabolic profiling of such communities indicate that the consumption and secretion of only a small number of metabolites often drives experimental outcomes[72–74,76,82,276]—providing a clue that the full network of metabolic interactions could be dramatically simplified while still generating realistic community behaviors. Hence, inspired by[71], we focus on the case in which the anaerobes take up an exogenously-supplied complex carbohydrate (teal) that cannot be accessed by the aerobes, breaking it down into simple sugar molecules (green) that they either directly consume for their growth or liberate to be consumed by the entire microbial community; for simplicity, we do not consider any other compounds, such as short-chain fatty acids, that may also liberated upon carbohydrate breakdown. The aerobes consume oxygen (magenta)—thereby providing favorable conditions for the anaerobes—while also consuming liberated simple sugar to utilize for their own growth. To examine the complex phenomena that can emerge in this model community, and to develop biophysical principles that can describe these phenomena, here we mathematically describe these mutualistic interactions by building on the framework of consumer-resource models commonly used in ecology[80,107,124,276].

Reactor configuration. In particular, we consider these coupled chemical and bacterial dynamics in the well-defined environment of a continuously-stirred tank reactor (CSTR)[71,96], as shown in Fig. 5.1a(i); because all chemical and bacterial species are well-mixed, their concentrations are only functions of time, not space, in our model. In this configuration, a liquid feed flow containing dissolved complex carbohydrate at a concen-

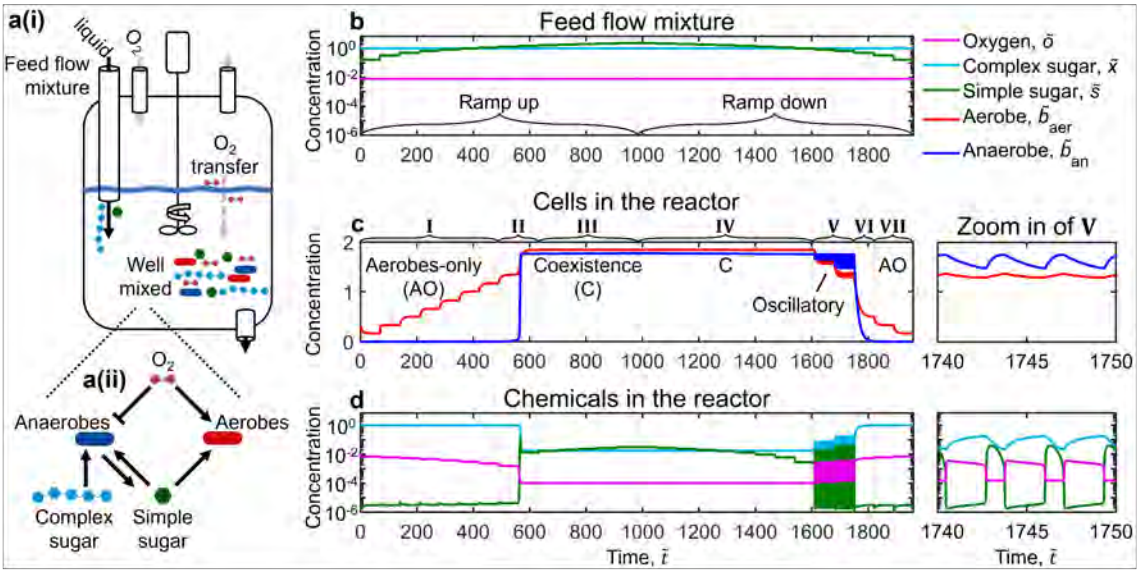

Figure 5.1: Model community of aerobes and anaerobes with mutualistic metabolic interactions exhibits two stable states, with bistable and oscillatory transitions between them driven by changing nutrient and oxygen fluxes. **a(i)** We consider a continuously-stirred tank reactor containing a well-mixed liquid culture of aerobes, anaerobes, dissolved oxygen, complex carbohydrate (labeled as complex sugar for brevity), and simple sugar. A liquid feed flow enters the reactor with dissolved complex carbohydrate and simple sugar, along with oxygen gas maintained at a constant partial pressure in the head space above the liquid. The rates of liquid outflow and inflow are matched, maintaining a constant liquid volume in the reactor. **a(ii)** Schematic of the mutualistic interactions between bacteria. Anaerobes take up complex carbohydrate and degrade it to simple sugar, some fraction of which is utilized solely by anaerobes, and the remainder of which is liberated to be shared by both anaerobes and aerobes for their growth. Aerobes consume oxygen, which inhibits (enhances) anaerobe (aerobe) activity. **b–d** show the results of an exemplary numerical simulation of our model with intermediate nutrient sharing ($\Xi = 0.5$) and oxygen abundance $\delta = 3.9 \times 10^{-3}$, using parameter values that are representative of experiments as given in Table 5.2. The composition of the incoming feed is given in **b**; to examine the influence of changing carbon fluxes, we progressively increase (ramp up) and then decrease (ramp down) the concentration of simple sugar in the feed. The resulting changes on the concentration of cells and chemicals in the reactor are given in **c** and **d**, respectively. Initially, the community is in the aerobes-only (AO) state (I), then abruptly transitions (II) to a state in which aerobes and anaerobes coexist (C, III–VI). Upon ramping down the simple sugar feed concentration, the C state persists, indicating hysteresis in the transitions between states. Further decreasing the simple sugar feed concentration gives rise to oscillations in the bacterial and chemical concentrations (magnified views to the right) before the community ultimately transitions back to the AO state (VII). All quantities are given in dimensionless form indicated by tildes; we rescale $\{t, x, s, o, b_{\rm an}, b_{\rm aer}\}$ by the characteristic quantities $\{\gamma_{\rm aer}^{-1}, x_{\rm feed}, x_{\rm feed}N\Xi, x_{\rm feed}N\Xi(\kappa_{o,{\rm aer},{\rm max}}/\kappa_{s,{\rm aer}}), x_{\rm feed}(\gamma_{\rm aer}/\kappa_{x,{\rm an}}), x_{\rm feed}N\Xi(\gamma_{\rm aer}/\kappa_{s,{\rm aer}})\}$ as detailed in the text.

tration $x_{\rm feed}$ and simple sugar at $s_{\rm feed}$ enters the reactor at a fixed volumetric flow rate; in general, we use x and s to describe the number concentrations of complex carbohydrate

and simple sugar in the reactor, respectively. The temperature and oxygen partial pressure in the head space of the reactor are held constant, thereby prescribing the saturation concentration of oxygen in the reactor liquid o_{sat}; hence, the dissolved molecular oxygen concentration o changes at a rate $\gamma_o(o_{\text{sat}} - o)$, where γ_o is the transfer rate coefficient[71]. The well-mixed liquid in the reactor exits at the same flow rate so as to maintain a constant internal volume. The flow rate divided by reactor volume then defines the dilution rate γ_d at which cells and carbon sources are refreshed to their feed flow quantities. We take $\gamma_d \ll \gamma_o$; therefore, oxygen transfer is rapid and we do not include γ_d in our equation describing oxygen dynamics. We also take the feed concentration of cells to be zero, and so, cells must grow within the reactor to avoid being diluted to a vanishing concentration and "washing out".

Complex carbohydrate uptake. The anaerobes take up the exogenously-supplied complex carbohydrate at a rate $b_{\text{an}}\kappa_{x,\text{an}}g_{x,\text{an}}(x)[1 - g_{o,\text{an}}(o)]$, where $\kappa_{x,\text{an}}$ describes the maximum uptake rate per cell. In general, the Michaelis-Menten function $g_{m,\text{i}}(m) \equiv m/(m + m_{1/2,\text{i}})$ quantifies the concentration dependence of the uptake of a substrate $m \in \{o, x, s\}$ by species $\text{i} \in \{\text{an}, \text{aer}\}$ relative to the characteristic concentration $m_{1/2,\text{i}}$[28,45,211–214,226]. Thus, the uptake rate increases and eventually saturates with increasing concentration of the complex carbohydrate, mediated by the availability of anaerobic conditions at $o \lesssim o_{1/2,\text{an}}$[124].

Consumption of simple sugar and oxygen. The anaerobes then break down the complex carbohydrate into simple sugar, a fraction Ξ of which are liberated by the anaerobes as a "common good" to be equally shared by all members of the microbial community, while the remaining $1 - \Xi$ are instead utilized solely by the anaerobes for their growth[71,80]. Thus, we describe the rate at which the anaerobes liberate simple sugar by $N\Xi b_{\text{an}}\kappa_{x,\text{an}}g_{x,\text{an}}(x)[1 -$

$g_{o,\mathrm{an}}(o)]$, where the degree of polymerization $N > 1$ quantifies the number of simple sugar units liberated from a complex carbohydrate molecule. The anaerobes and aerobes then consume the simple sugar at total rates $b_{\mathrm{an}}\kappa_{s,\mathrm{an}}g_{s,\mathrm{an}}(s)[1-g_{o,\mathrm{an}}(o)]$ and $b_{\mathrm{aer}}\kappa_{s,\mathrm{aer}}g_{s,\mathrm{aer}}(s)g_{o,\mathrm{aer}}(o)$, respectively; here, $\kappa_{s,\mathrm{an}}$ and $\kappa_{s,\mathrm{aer}}$ describe the maximum consumption rates per cell. Oxygen is concomitantly consumed by the aerobes at a rate $b_{\mathrm{aer}}\kappa_{o,\mathrm{aer}}(s)g_{o,\mathrm{aer}}(o)$, where the consumption rate per cell depends on carbon availability[111,277], and takes the form $\kappa_{o,\mathrm{aer}}(s)$ $\equiv \kappa_{o,\mathrm{aer,min}} + (\kappa_{o,\mathrm{aer,max}} - \kappa_{o,\mathrm{aer,min}})g_{s,\mathrm{aer}}(s)$; this function interpolates between the basal consumption rate in starved conditions, $\kappa_{o,\mathrm{aer,min}}$, and the maximum consumption rate in sugar-replete conditions, $\kappa_{o,\mathrm{aer,max}}$. While we take $\kappa_{o,\mathrm{aer,min}} > 0$ as is often the case, our results are unaltered if instead we take $\kappa_{o,\mathrm{aer,min}} = 0$ (Fig. 5.2). Conversely, choosing $\kappa_{o,\mathrm{aer,min}}$ $= \kappa_{o,\mathrm{aer,max}}$, which completely removes the dependence of oxygen consumption by aerobes on simple sugar availability, influences some of the emergent community behavior (Fig. 5.5) as expected, as described further below.

Bacterial growth. Simple sugar consumption then results in cellular growth. The rate at which anaerobe concentration increases has a contribution from the consumption of non-shared sugars, $N(1-\Xi)b_{\mathrm{an}}\gamma_{\mathrm{an}}g_{x,\mathrm{an}}(x)[1-g_{o,\mathrm{an}}(o)]$, and another contribution from the consumption of liberated simple sugar that is shared among all bacteria, $b_{\mathrm{an}}\gamma_{\mathrm{an}}g_{s,\mathrm{an}}(s)[1-g_{o,\mathrm{an}}(o)]$; here, γ_{an} is the maximal cellular growth rate per unit simple sugar. Conversely, the rate at which aerobe concentration increases only reflects the consumption of shared simple sugar, $b_{\mathrm{aer}}\gamma_{\mathrm{aer}}g_{s,\mathrm{aer}}(s)g_{o,\mathrm{aer}}(o)$, where again γ_{aer} is the maximal cellular growth rate per unit simple sugar. This formulation of our model treats oxygen as a joint mediator of both aerobic and anaerobic metabolism of the sugar, albeit in opposing ways; an alternative formulation that instead employs Liebig's law of the minimum, wherein growth is set solely

by the scarcest of the two (oxygen or sugar) yields identical results, as shown in Fig. 5.3.

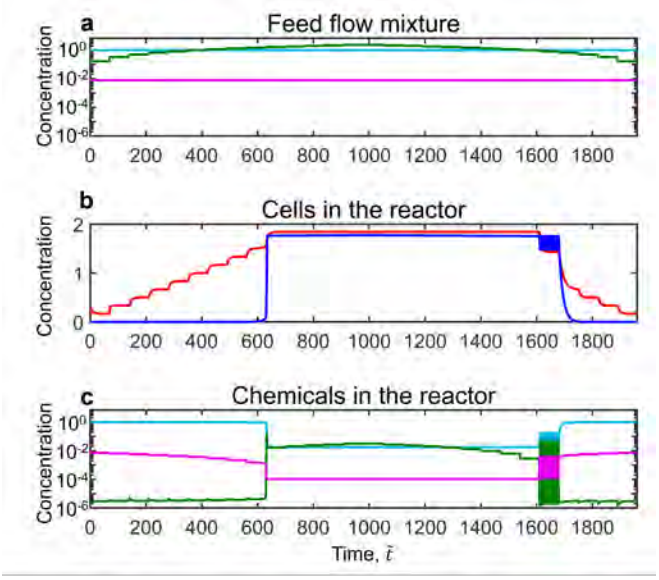

Figure 5.2: Our findings of bistability and oscillations are unchanged if the minimum oxygen consumption rate by aerobes is set to zero. While our main text results take $\kappa_{o,\mathrm{aer},\mathrm{min}} > 0$ as is often the case, setting $\kappa_{o,\mathrm{aer},\mathrm{min}} = 0$ yields nearly identical results, as shown in the Figure above, which corresponds to Fig. 5.1.

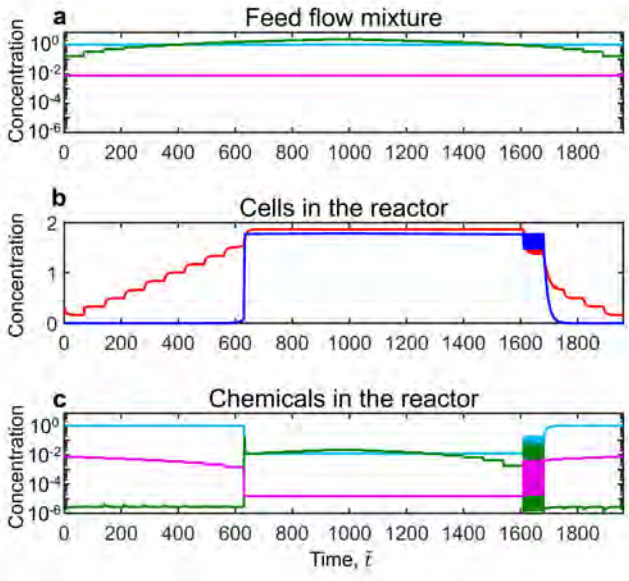

Figure 5.3: Our findings of bistability and oscillations are unchanged upon incorporating Liebig's law of the minimum. For simplicity and to make our model more generally applicable to other mediators of microbial metabolism (e.g., pH, signaling molecules, toxins), we take oxygen as a joint mediator of carbon metabolism. Alternatively incorporating Liebig's law of the minimum, wherein the scarcest of the two (oxygen or sugar) determines growth rate and the uptake rate of the non-limiting of the two, yields identical results as shown above (identical simulation as in Fig. 5.1 but with Liebig's law). For this formulation, we define a function $g_{\text{aer}}(o,s) \equiv \min\{g_{s,\text{aer}}(s), \omega g_{o,\text{aer}}(o)\}$, where $\omega = 6$ is the utilization ratio that corresponds to the oxygen molecules required to fully utilize one glucose monomer[111]. Then, we replace $\kappa_{o,\text{aer}}(s)g_{o,\text{aer}}(o)$ with $\kappa_{o,\text{aer,max}}g_{\text{aer}}(o,s)$ in Eq. 5.3 and $g_{s,\text{aer}}(s)g_{o,\text{aer}}(o)$ with $g_{\text{aer}}(o,s)$ in Eqs. 5.2 and 5.5.

Governing equations. Our model is thus summarized as:

$$\text{Complex carbohydrate}: \frac{dx}{dt} = \underbrace{\gamma_d x_{\text{feed}}}_{\text{Inflow}} - \underbrace{\gamma_d x}_{\text{Outflow}} - \underbrace{b_{\text{an}} \kappa_{x,\text{an}} g_{x,\text{an}}(x)[1 - g_{o,\text{an}}(o)]}_{\text{Anaerobe uptake of } x}, \quad (5.1)$$

$$\text{Simple sugar}: \frac{ds}{dt} = \underbrace{\gamma_d s_{\text{feed}}}_{\text{Inflow}} - \underbrace{\gamma_d s}_{\text{Outflow}} + \underbrace{N \Xi b_{\text{an}} \kappa_{x,\text{an}} g_{x,\text{an}}(x)[1 - g_{o,\text{an}}(o)]}_{\text{Anaerobe liberation of } s} \quad (5.2)$$

$$- \underbrace{b_{\text{an}} \kappa_{s,\text{an}} g_{s,\text{an}}(s)[1 - g_{o,\text{an}}(o)]}_{\text{Anaerobe consumption of } s} - \underbrace{b_{\text{aer}} \kappa_{s,\text{aer}} g_{s,\text{aer}}(s) g_{o,\text{aer}}(o)}_{\text{Aerobe consumption of } s},$$

$$\text{Oxygen}: \frac{do}{dt} = \underbrace{\gamma_o (o_{\text{sat}} - o)}_{\text{Influx at liquid interface}} - \underbrace{b_{\text{aer}} \kappa_{o,\text{aer}}(s) g_{o,\text{aer}}(o)}_{\text{Aerobe consumption of } o}, \quad (5.3)$$

$$\text{Anaerobes}: \frac{db_{\text{an}}}{dt} = - \underbrace{\gamma_d b_{\text{an}}}_{\text{Outflow}} + \underbrace{N(1 - \Xi) b_{\text{an}} \gamma_{\text{an}} g_{x,\text{an}}(x)[1 - g_{o,\text{an}}(o)]}_{\text{Growth from non-shared } s} \quad (5.4)$$

$$+ \underbrace{b_{\text{an}} \gamma_{\text{an}} g_{s,\text{an}}(s)[1 - g_{o,\text{an}}(o)]}_{\text{Growth from shared } s},$$

$$\text{Aerobes}: \frac{db_{\text{aer}}}{dt} = - \underbrace{\gamma_d b_{\text{aer}}}_{\text{Outflow}} + \underbrace{b_{\text{aer}} \gamma_{\text{aer}} g_{s,\text{aer}}(s) g_{o,\text{aer}}(o)}_{\text{Growth from } s}, \quad (5.5)$$

where t represents time.

5.2.2 Characteristic dimensionless parameters

Non-dimensionalizing Eqs. 5.1–5.5 yields useful dimensionless parameters characterizing the biological, chemical, and physical dynamics underlying this complex system. In particular, we choose to rescale $\{t, x, s, o, b_{\text{an}}, b_{\text{aer}}\}$ by the characteristic quantities $\{\gamma_{\text{aer}}^{-1}, x_{\text{feed}}, x_{\text{feed}}\mathcal{N}\Xi, x_{\text{feed}}\mathcal{N}\Xi(\kappa_{o,\text{aer,max}}/\kappa_{s,\text{aer}}), x_{\text{feed}}(\gamma_{\text{aer}}/\kappa_{x,\text{an}}), x_{\text{feed}}\mathcal{N}\Xi(\gamma_{\text{aer}}/\kappa_{s,\text{aer}})\}$ that describe the aerobe doubling time, feed concentration of complex carbohydrate, concentration of liberated simple sugar from this feed, corresponding concentration of consumed oxygen, corresponding concentration of newly-grown anaerobes, and corresponding concentration of newly-grown aerobes, respectively. We also rescale $\kappa_{o,\text{aer}}(s)$ by $\kappa_{o,\text{aer,max}}$. This process yields the non-dimensional equations:

$$\text{Complex carbohydrate}: \quad \frac{d\tilde{x}}{d\tilde{t}} = \gamma(1-\tilde{x}) - \tilde{b}_{\text{an}}\tilde{g}_{x,\text{an}}(\tilde{x})[1-\tilde{g}_{o,\text{an}}(\tilde{o})], \tag{5.6}$$

$$\begin{aligned}\text{Simple sugar}: \quad \frac{d\tilde{s}}{d\tilde{t}} &= \gamma(\beta\Xi^{-1}-\tilde{s}) + \tilde{b}_{\text{an}}\tilde{g}_{x,\text{an}}(\tilde{x})[1-\tilde{g}_{o,\text{an}}(\tilde{o})] \\ &\quad -\alpha\Xi^{-1}\tilde{b}_{\text{an}}\tilde{g}_{s,\text{an}}(\tilde{s})[1-\tilde{g}_{o,\text{an}}(\tilde{o})] - \tilde{b}_{\text{aer}}\tilde{g}_{s,\text{aer}}(\tilde{s})\tilde{g}_{o,\text{aer}}(\tilde{o}),\end{aligned} \tag{5.7}$$

$$\text{Oxygen}: \quad \frac{d\tilde{o}}{d\tilde{t}} = \kappa(\delta\Xi^{-1}-\tilde{o}) - \tilde{b}_{\text{aer}}\tilde{\kappa}_{o,\text{aer}}(\tilde{s})\tilde{g}_{o,\text{aer}}(\tilde{o}), \tag{5.8}$$

$$\begin{aligned}\text{Anaerobes}: \quad \frac{d\tilde{b}_{\text{an}}}{d\tilde{t}} &= -\gamma\tilde{b}_{\text{an}} + N(1-\Xi)\lambda\tilde{b}_{\text{an}}\tilde{g}_{x,\text{an}}(\tilde{x})[1-\tilde{g}_{o,\text{an}}(\tilde{o})] \\ &\quad +\lambda\tilde{b}_{\text{an}}\tilde{g}_{s,\text{an}}(\tilde{s})[1-\tilde{g}_{o,\text{an}}(\tilde{o})],\end{aligned} \tag{5.9}$$

$$\text{Aerobes}: \frac{d\tilde{b}_{\text{aer}}}{d\tilde{t}} = -\gamma\tilde{b}_{\text{aer}} + \tilde{b}_{\text{aer}}\tilde{g}_{s,\text{aer}}(\tilde{s})\tilde{g}_{o,\text{aer}}(\tilde{o}), \tag{5.10}$$

where the tildes indicate non-dimensionalized variables. Seven dimensionless parameters emerge:

- The *anaerobic uptake* parameter $\alpha \equiv \kappa_{s,\text{an}}/(\kappa_{x,\text{an}}N)$ compares the anaerobic carbon uptake rates of simple sugar and complex carbohydrates. When $\alpha > 1$, anaerobe uptake of simple sugar is faster than that of complex carbohydrates, whereas when $\alpha < 1$, anaerobe uptake of complex carbohydrates dominates. As shown in Table 5.1, typical experiments can fall in either regime.

- The *simple sugar abundance* parameter $\beta \equiv s_{\text{feed}}/(x_{\text{feed}}N)$ compares the abundance of simple sugar in the feed with that contained in the complex carbohydrate in the feed. When $\beta > 1$, carbon enters the system predominantly in the form of simple sugar, whereas when $\beta < 1$, carbon enters the system predominantly in the form of complex carbohydrates. As shown in Table 5.1, typical experiments fall in this latter regime.

- The *aerobic washout* parameter $\gamma \equiv \gamma_d/\gamma_{\text{aer}}$ compares the rates of aerobic growth and dilution. When $\gamma > 1$, aerobes are diluted from the reactor faster than they can grow, leading to their washout, whereas when $\gamma < 1$, aerobic growth is sufficiently fast for them to remain in the reactor. As shown in Table 5.1, typical experiments fall in this latter regime.

- The *oxygen abundance* parameter $\delta \equiv (o_{\text{sat}}/\kappa_{o,\text{aer,max}})/(x_{\text{feed}}N/\kappa_{s,\text{aer}})$ compares the time needed for aerobes to deplete oxygen from the saturated influx with the time

needed for them to deplete the quantity of simple sugar contained in the feed of complex carbohydrate. When $\delta > 1$, depletion of oxygen by the aerobes is slow compared to that of simple sugar, whereas when $\delta < 1$, oxygen is rapidly depleted by aerobic consumption. As shown in Table 5.1, typical experiments fall in this latter regime.

- The *oxygen transfer* parameter $\kappa \equiv \gamma_o / \gamma_{\text{aer}}$ compares the rates of oxygen influx and aerobic growth. When $\kappa > 1$, the oxygen supply is rapidly replenished to its saturation concentration o_{sat}, whereas when $\kappa < 1$, oxygen influx is slow. As shown in Table 5.1, typical experiments fall in the former regime.

- The *growth* parameter $\lambda \equiv \gamma_{\text{an}} / \gamma_{\text{aer}}$ compares the rates of anaerobic and aerobic growth. When $\lambda > 1$, anaerobes can grow much faster than aerobes, whereas when $\lambda < 1$, aerobic growth dominates. As shown in Table 5.1, typical experiments can fall in either regime.

- The *oxygen consumption* parameter $\varepsilon \equiv \kappa_{o,\text{aer,min}} / \kappa_{o,\text{aer,max}}$ compares the minimum and maximum oxygen consumption rates by aerobes under nutrient-depleted or nutrient-replete conditions, respectively. When $\varepsilon = 1$ (its maximal value, by definition), oxygen consumption by aerobes does not depend on simple sugar availability, whereas when $\varepsilon \ll 1$ oxygen consumption is strongly dependent on simple sugar levels. As shown in Table 1, in this work, we consider both limits for generality.

Our overarching goal is to address the question: *For a given microbial community, how does changing the balance of carbon and oxygen fluxes alter its overall composition?* To this end,

in what follows, we use the model summarized by Eqs. 5.6–5.10 to explore the influence of varying β and δ, keeping all other parameters constant.

Parameter	Name	Values	References
Ξ	Shared fraction	0 to 1	71,74,82,162,276
N	Degree of polymerization	10^0 to 10^2	71,74,82,162,276
$\alpha \equiv \kappa_{s,\mathrm{an}}/(\kappa_{x,\mathrm{an}}N)$	Anaerobic uptake	0 to 10^1	71,82,158,162
$\beta \equiv s_{\mathrm{feed}}/(x_{\mathrm{feed}}N)$	Simple sugar abundance	0 to 10^0	71,72,74,76,82,158,162,278,279
$\gamma \equiv \gamma_d/\gamma_{\mathrm{aer}}$	Aerobic washout	0 to 10^0	29,71,72,74,158,162,278,279
$\delta \equiv (o_{\mathrm{sat}}/\kappa_{o,\mathrm{aer,max}})/(x_{\mathrm{feed}}N/\kappa_{s,\mathrm{aer}})$	Oxygen abundance	10^{-3} to 10^{-1}	71,111,158,277
$\kappa \equiv \gamma_o/\gamma_{\mathrm{aer}}$	Oxygen transfer	10^1 to 10^2	29,71
$\lambda \equiv \gamma_{\mathrm{an}}/\gamma_{\mathrm{aer}}$	Growth	0 to 10^1	74,82,124,276,278,279
$\varepsilon \equiv \kappa_{o,\mathrm{aer,min}}/\kappa_{o,\mathrm{aer,max}}$	Oxygen consumption	0 to 10^0	See Fig. 5.5

Table 5.1: Dimensionless parameters characterizing our model. Also listed are ranges of their values reported in previous studies.

5.2.3 Implementation of numerical simulations

First, to explore the influence of varying simple sugar abundance, we systematically vary s_{feed} (which varies β) and use numerical simulations of Eqs. 5.6–5.10 to examine the resulting variations in the complex carbohydrate, simple sugar, oxygen, aerobe, and anaerobe concentrations in the reactor, represented by the non-dimensional variables $\tilde{x}, \tilde{s}, \tilde{o}, \tilde{b}_{\mathrm{aer}}, \tilde{b}_{\mathrm{an}}$, respectively. We keep all the other input parameters constant at their representative experimental values as given in Table 5.2. Then, to explore the additional influence of varying oxygen depletion, we also vary o_{sat} (which varies δ) and examine the resulting variations in chemical and bacterial concentrations. Finally, to investigate the pivotal influence of metabolic mutualism, we examine these behaviors for different values of the sharing parameter Ξ, ranging from a high value of 0.9 representing "altruistic" liberation of sugars by the

anaerobes to a low value of 0.1 representing "greedy" utilization of sugars by the anaerobes.

To do so, we use the `ode23t` solver in `MATLAB`, initializing each simulation with low aerobe and anaerobe concentrations $b_{\text{aer},0}$ and $b_{\text{an},0}$ chosen to be ≈ 0.3 and $\approx 10^{-3}$ times smaller than the characteristic concentrations $\{x_{\text{feed}}(\gamma_{\text{aer}}/\kappa_{x,\text{an}}), x_{\text{feed}}N\Xi(\gamma_{\text{aer}}/\kappa_{s,\text{aer}})\}$ (Table 5.2), matching the experiments in[71]. The initial time step is 10^{-15} s, chosen to be $> 10^{18}$ times smaller than the characteristic time scale γ_{aer}^{-1}. The solver then varies the time step dynamically to ensure a relative error tolerance of 10^{-4} for all quantities or absolute error tolerances of 10^{7} cells/mL and 10^{-6} μM for cells and chemicals, respectively; these tolerance values are chosen to be $\approx \{50, 400\}$ and $\approx \{60, 3000, 1600\}$ times smaller than the characteristic concentrations $\{x_{\text{feed}}(\gamma_{\text{aer}}/\kappa_{x,\text{an}}), x_{\text{feed}}N\Xi(\gamma_{\text{aer}}/\kappa_{s,\text{aer}})\}$ (cells) and $\{x_{\text{feed}}, x_{\text{feed}}N\Xi, x_{\text{feed}}N\Xi(\kappa_{o,\text{aer,max}}/\kappa_{s,\text{aer}})\}$ (chemicals), respectively. For each distinct $\{\beta, \delta\}$ condition explored, we then solve Eqs. 5.6–5.10 for a duration of $\Delta\tilde{t} = 70$ to match[71] (Fig. 5.1) or $\Delta\tilde{t} = 280$ (Figs. 5.6 and 5.7) to ensure we reach a (possibly dynamic) steady state, using the final state of the preceding condition to initialize the next with a new value of β, representing a change in the influx of fresh simple sugar into the reactor. Furthermore, as in[71], we also employ a "reinoculation protocol" in which if either $\{b_{\text{aer}}, b_{\text{an}}\}$ drops below the low initial concentrations $\{b_{\text{aer},0}, b_{\text{an},0}\}$ at the end of a given simulation condition, we reset them to those initial values at the beginning of the next simulation condition tested to prevent irreversible washout of cells from the reactor.

Parameter	Value in Fig. 5.1	Value in Fig. 5.6	Value in Fig. 5.7	References
Ξ	0.5		0.1, 0.5, 0.9	[71]
N	100			[71]
Δt	50 h	200 h	200 h	[71]
o_{sat}	13 μM		1.8 to 23 μM	[71]
x_{feed}	60 μM			[71]
s_{feed}	0.5 to 7 mM			[71]
$b_{\text{aer},0}$	1.7×10^8 cells/mL			[71]
$b_{\text{an},0}$	5.0×10^6 cells/mL			[71]
Initial s	0			[71]
Initial o	18 μM			
Initial x	60 μM			[71]
$o_{1/2,\text{aer}}$	1 μM			[29]
$o_{1/2,\text{an}}$	0.35 μM			[71]
$x_{1/2,\text{an}}$	8 μM			[71]
$s_{1/2,\text{aer}}$	0.05 μM			[71]
$s_{1/2,\text{an}}$	1.4 mM			[71]
$\kappa_{o,\text{aer,max}}$	1.2×10^{-12} mM (cells/mL)$^{-1}$ s^{-1}			[29]
$\kappa_{o,\text{aer,min}}$	3.3×10^{-14} mM (cells/mL)$^{-1}$ s^{-1}			[111,277]
$\kappa_{x,\text{an}}$	6.7×10^{-15} mM (cells/mL)$^{-1}$ s^{-1}			[71]
$\kappa_{s,\text{aer}}$	2.2×10^{-12} mM (cells/mL)$^{-1}$ s^{-1}			[71]
$\kappa_{s,\text{an}}$	9.1×10^{-13} mM (cells/mL)$^{-1}$ s^{-1}			[71]
γ_{aer}	1.4 h^{-1}			[111]
γ_{an}	0.05 h^{-1}			* see caption
γ_o	47.4 h^{-1}			[71]
γ_d	0.2 h^{-1}			[71]
Ξ	0.5		0.1, 0.5, and 0.9	
N	100			
α	1.4			
β	0.083 to 1.2			
γ	0.14			
δ	0.0039		0.00056 to 0.0072	
κ	34			
λ	0.036			
ε	0.029			
$\tilde{o}_{1/2,\text{aer}}$	6.2×10^{-4}			
$\tilde{o}_{1/2,\text{an}}$	2.2×10^{-4}			
$\tilde{x}_{1/2,\text{an}}$	0.13			
$\tilde{s}_{1/2,\text{aer}}$	1.7×10^{-5}			
$\tilde{s}_{1/2,\text{an}}$	0.47			

Table 5.2: Parameter values used in our simulations. Upper and lower tables show dimensional and corresponding dimensionless parameters, respectively. Values not listed are the same as in Fig. 5.1.

* This value was chosen to be much lower than the aerobic growth rate, while still being non-zero.

5.3 Results

5.3.1 Chemical and bacterial dynamics under varying simple sugar abundance

How do variations in simple sugar abundance alter the composition of the overall microbial community? And are these alterations history dependent, as is often observed in experiments? To answer these questions, we first investigate the coupled chemical and bacterial dynamics quantified by Eqs. 5.6–5.10 that emerge upon successive variations in the feed simple sugar concentration s_{feed} (i.e., varying β) for an exemplary case of $\Xi = 0.5$ and $N = 100$. In particular, as shown in Fig. 5.1b, we hold the feed concentrations of oxygen (magenta) and complex carbohydrate (teal) constant, and successively increase s_{feed} (green, increasing β) step-wise every $\Delta\tilde{t} = 70$ ("ramp up"). To investigate any possible history dependence, we then "ramp down" by successively decreasing s_{feed} (decreasing β) step-wise by the same amount. The resulting concentrations of cells and chemicals in the reactor are shown in Figs. 5.1c–d, respectively.

The aerobes-only state. During the initial phase of the ramp up period ($0 \leq \tilde{t} \leq 490$, denoted by I in Fig. 5.1c), oxygen consumption by the aerobes is insufficient to sustain anaerobic growth (dark blue, Fig. 5.1c). As a result, the microbial community is in the *aerobes-only* (AO) state in which solely aerobes consume the supplied simple sugar (green, Fig. 5.1d) and utilize it for their growth; the concentration of complex carbohydrate (teal) remains unchanged, since this is only taken up by anaerobes. In this state, with each successive increase in simple sugar abundance β, the aerobe concentration exponentially reaches a new steady-state value (red, Fig. 5.1c). The oxygen concentration concomitantly approaches progressively decreasing steady-state values due to aerobic consumption (magenta,

Fig. 5.1d). For clarity of notation, we denote long-time steady-state values of chemical and bacterial concentrations by the subscript $_s$ hereafter.

Coexistence and hysteresis. As the concentration of aerobes rises with increasing simple sugar abundance β, the oxygen concentration in the reactor eventually decreases enough to sustain anaerobic growth as well—as shown by the drop in the magenta line just before $\tilde{t} \approx 560$ in Fig. 5.1d. Consequently, the anaerobe concentration increases dramatically (dark blue, Fig. 5.1c); we denote this transition by II.

As the anaerobes proliferate, they take up the exogenously-supplied complex carbohydrate (teal, Fig. 5.1d) and continually liberate new simple sugar to be shared by the entire microbial community (Fig. 5.4). Despite the low oxygen concentration in the reactor, aerobes can also proliferate, albeit with low metabolic activity. Hence, these carbon-replete conditions give rise to the *coexistence* (C) state ($560 < \tilde{t} \leq 980$, denoted by III in Fig. 5.1c). Both aerobes (red) and anaerobes (dark blue) are maintained at nearly constant concentrations, buffered against subsequent changes in the feed simple sugar supply.

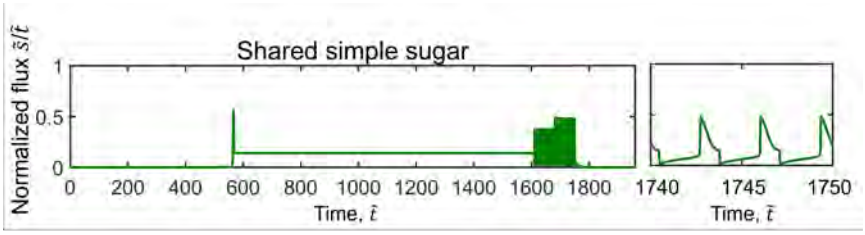

Figure 5.4: Dynamics of simple sugar sharing by the anaerobes. The shared flux of simple sugar is given by $\tilde{b}_{\mathrm{an}}\tilde{g}_{x,\mathrm{an}}(\tilde{x})[1 - \tilde{g}_{o,\mathrm{an}}(\tilde{o})]$ (the second term in Eq. 5.7) and is shown for the simulation in Fig. 5.1. On the right, we show a magnified view of the oscillatory dynamics immediately before the transition from the C to AO states.

Indeed, the coexistence state also persists as the simple sugar abundance β is ramped down ($980 < \tilde{t} \leq 1610$, denoted by IV in Fig. 5.1c). Strikingly, we observe hysteretic be-

havior: the chemical and bacterial concentrations during the ramp down do not mirror those of the ramp up period—as observed experimentally as well[71]. For example, the coexistence state persists over a broader range of simple sugar abundance β, including at values that were too low to initiate coexistence during ramp up; see, for example, $1400 < \tilde{t} \leq 1680$ in Fig. 5.1c–d. Having established a mutually-beneficial state, this mixed microbial community continues to coexist, despite the decreasing levels of exogenously-supplied simple sugar.

Oscillatory dynamics. Further decreasing the simple sugar abundance β leads to a new mode of coexistence. Surprisingly, we observe sustained oscillations in both chemical and bacterial concentrations ($1610 < \tilde{t} \leq 1750$, denoted by V in Fig. 5.1c)—again recapitulating some experimental observations[96]. The concentrations of both aerobes and anaerobes rise and fall in phase (magnified view to the right of Fig. 5.1c). The chemical concentrations correspondingly switch between metastable conditions resembling the coexistence state with low oxygen, but high simple sugar availability, and the aerobes-only state with high oxygen, but low simple sugar availability (Fig. 5.1d, right).

These complex dynamics again reflect the central role of microbial mutualism. In the low-oxygen metastable state, anaerobes can take up complex carbohydrate (teal) and liberate new simple sugar molecules that are utilized by the entire community (e.g., rise in the green line at $\tilde{t} \approx 1743$). Then, as the complex carbohydrate is increasingly depleted by the anaerobes, less simple sugar is liberated (Fig. 5.4) and available for the community to use (drop in the green line for $1743 \lesssim \tilde{t} \lesssim 1744$). Because oxygen consumption depends on carbon availability, aerobic consumption of oxygen becomes concomitantly limited—eventually driving an abrupt transition to the high-oxygen metastable state (e.g., rise in the

magenta line at $\tilde{t} \approx 1744$). Under these conditions, anaerobic metabolism is impeded but not completely abrogated, enabling the concentration of complex carbohydrate to gradually be replenished (teal, $1744 < \tilde{t} < 1746$) and broken down into shared simple sugar. Thus, the amount of shared simple sugar concomitantly increases (Fig. 5.4), enabling the aerobes to increasingly deplete oxygen (magenta, $1744 < \tilde{t} < 1746$)—eventually driving another abrupt transition back to the low-oxygen state ($\tilde{t} \approx 1746$) in which anaerobic growth is sustained again. Indeed, removing the dependence of oxygen consumption by aerobes on simple sugar availability abolishes the oscillations entirely (Fig. 5.5)—providing further confirmation of this picture.

Transition back to the aerobes-only state. Further decreasing the simple sugar abundance β eventually causes the high-oxygen state to dominate—leading to a precipitous decline in the concentration of anaerobes ($1750 \leq \tilde{t} \leq 1820$, denoted by VI in Fig. 5.1c). The community thus transitions back to the AO state denoted by VII in Fig. 5.1c.

Taken together, these results (Fig. 5.1b–d) highlight the rich chemical and bacterial behaviors that emerge from our minimal model of metabolic mutualism. Remarkably, despite the simplicity of the model compared to those that consider a more complex network of metabolic fluxes, it successfully recapitulates the two different states observed in experiments upon varying carbon and oxygen fluxes[71]: the aerobes-only (AO) state and the state of aerobe-anaerobe coexistence (C). Our model also recapitulates the hysteretic nature of transitioning between these two states[71] as well as the possible emergence of oscillations between them[96], as observed in many experiments. Having recapitulated these behaviors, we next set out to uncover the underlying biophysical principles that govern them.

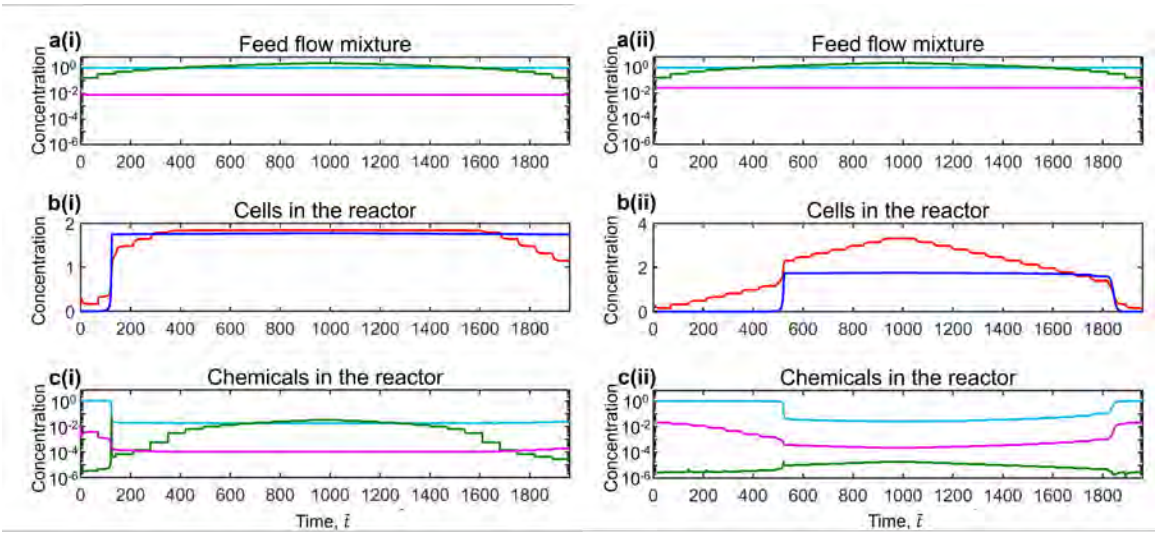

Figure 5.5: Removing the dependence of oxygen consumption by aerobes on carbon availability eliminates oscillatory growth dynamics and yields simulations that closely match prior metabolic model predictions. **(i)** Results of the identical simulation as in Fig. 5.1, but with $\kappa_{o,\mathrm{aer,min}} = \kappa_{o,\mathrm{aer,max}}$ ($\varepsilon = 1$). In this case, because oxygen is depleted more rapidly, the coexistence state arises earlier and persists over the entire range of β that is subsequently explored. Because this range of β does not induce a transition from coexistence (C) back to the aerobes-only (AO) state, oscillations (which arise during this transition as shown in Fig. 5.1) do not have the chance to occur. To further probe this behavior, in **(ii)** we increase the value of oxygen inflow concentration to 43 μM (δ of 0.014), which induces the transition from the C to AO states. Nevertheless, in this case, oscillations still do not occur, indicating that the dependence of oxygen consumption on carbon availability is necessary for the oscillatory dynamics observed in Fig 5.1 to arise. Notably, **(ii)** indicates that the concentration of aerobes continually increases with β in the coexistence regime ($\tilde{t} = 600$ to 1000) in this case, as was also observed in [71]; moreover, the regime over which bistability persists corresponds closely to the results of the more sophisticated metabolic modeling in [71].

5.3.2 Biophysical principles governing the different states and transitions between them

To summarize the findings in Fig. 5.1, we plot the steady-state bacterial concentrations $b_{\mathrm{aer,s}}$ and $b_{\mathrm{an,s}}$ for the different values of simple sugar abundance β tested in Fig. 5.6a–b; the corresponding steady-state concentrations of oxygen, complex carbohydrate, and simple sugar are shown in c–e. The circles show the results of the full numerical simulations, while the

curves show the results of the theoretical predictions developed hereafter. The filled circles show the states that arise during the ramp up period (increasing β), while the open circles show the ramp down period (decreasing β). As described in §5.3.1, the microbial community is initially in the aerobes-only state with $b_{\text{aer,s}} > 0$ and $b_{\text{an,s}} = 0$ (leftmost points in Fig. 5.6). As the simple sugar abundance β is increased, the aerobe concentration $b_{\text{aer,s}}$ monotonically increases (denoted by I in panel a) while the anaerobe concentration $b_{\text{an,s}}$ remains negligible. Then, above a critical value of $\beta = \beta_{\text{aer,crit}} \approx 0.6$, the community abruptly transitions to the state of coexistence (II) with $b_{\text{aer,s}} \approx 1.85$ and $b_{\text{an,s}} \approx 1.75$, independent of subsequent increases in β (III). The reverse behavior is hysteretic upon ramping down: the community persists in the coexistent state over a broader range of $1.2 > \beta > 0.4$ (IV), eventually exhibiting oscillatory dynamics (indicated by V and the undulating red line in panel a). It then abruptly transitions back to the aerobes-only state as simple sugar abundance decreases below a critical value $\beta = \beta_{\text{coex,min}} \approx 0.28$ (VI–VII).

Having characterized these states and transitions between them, we next seek biophysical principles that quantitatively determine the:

- Steady-state concentration $b_{\text{aer,s}}$ in the AO state (I and VII),
- Critical value $\beta_{\text{aer,crit}}$ that determines the transition from the AO to C state (II),
- Steady-state concentrations $b_{\text{aer,s}}$ and $b_{\text{an,s}}$ in the C state (III and IV),
- Critical value $\beta_{\text{coex,min}}$ that determines the subsequent transition from the C to AO state (VI).

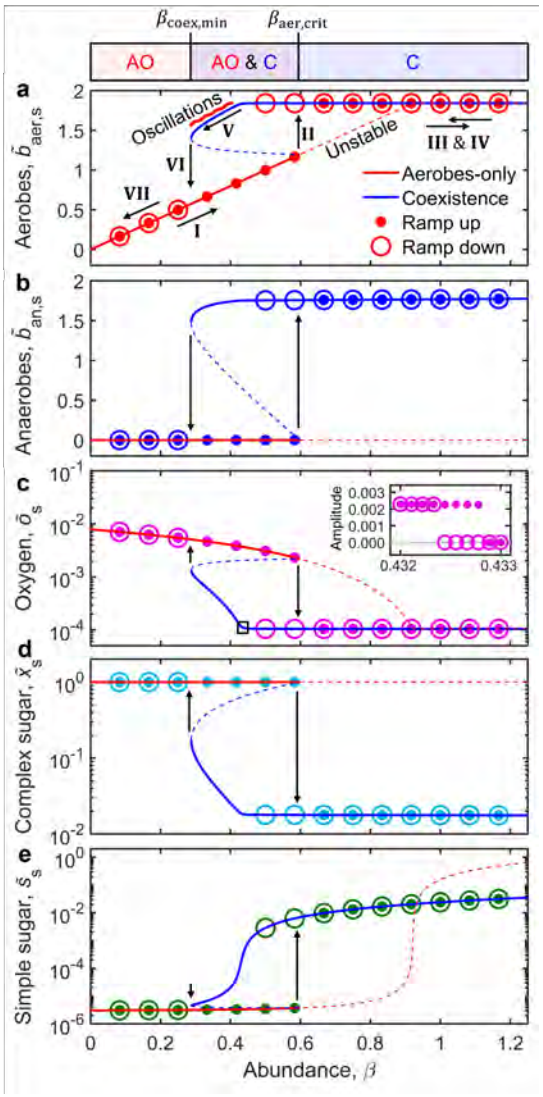

Figure 5.6: Phase space of microbial steady states. Panels **a–b** show the steady-state aerobe and anaerobe concentrations at each value of the simple sugar abundance β for the simulation shown in Fig. 5.1; the corresponding steady-state chemical concentrations are given in panels **c–e**. Filled and open circles show ramp up (increasing β) and ramp down (decreasing β), respectively. Red and blue curves show the analytical solutions predicted by our theory (Eqs. 5.11–5.15); solid and dashed lines indicate the stable and unstable states, respectively. Initially the microbial community is in the aerobes-only (AO) state (I), and then transitions (II) to the coexistence (C) state (III) above $\beta = \beta_{aer,crit} \approx 0.6$. Upon ramping down, the community persists in the C state (IV) over a broader range of β, indicating hysteretic behavior. It eventually exhibits oscillations (V) and then transitions (VI) back to the AO state (VII) below $\beta = \beta_{coex,min} \approx 0.28$. Inset to **c** shows the amplitude of oscillations in oxygen concentration just near the onset of oscillatory dynamics, in the narrow region indicated by the small black box in the main panel; the oscillation amplitude displays a hysteresis loop characteristic of a subcritical Hopf bifurcation, with the grey line indicating zero amplitude for clarity. The overlying bar indicates monostable AO, bistable AO and C, and monostable C regimes demarcated by the critical values $\beta_{coex,min}$ and $\beta_{aer,crit}$. Black arrows indicate the direction of transitions between states. All input parameters are the same as in Fig. 5.1 except $\Delta\tilde{t} = 280$, which is longer to ensure that simulations reach the long-time steady state. All quantities are given in dimensionless form indicated by tildes; we rescale $\{x, s, o, b_{an}, b_{aer}\}$ by the characteristic quantities $\{x_{feed}, x_{feed}N\Xi, x_{feed}N\Xi(\kappa_{o,aer,max}/\kappa_{s,aer}), x_{feed}(\gamma_{aer}/\kappa_{x,an}), x_{feed}N\Xi(\gamma_{aer}/\kappa_{s,aer})\}$ as detailed in the text.

The aerobes-only state. In the AO state, at each imposed value of the simple sugar abundance β, the aerobe concentration reaches a well-defined steady-state value $b_{\mathrm{aer,s}}$ (I and VII in Figs. 5.1c, 5.6); the simple sugar and oxygen concentrations reach corresponding steady-state values $\tilde{s}_{\mathrm{s}}$ and $\tilde{o}_{\mathrm{s}}$, respectively. Therefore, we begin by seeking steady-state solutions to Eqs. 5.6–5.10 by setting $d/d\tilde{t} = 0$. This procedure yields

$$\text{From Eq. 5.6}: \quad \tilde{b}_{\mathrm{an,s}}(\tilde{x}_{\mathrm{s}}, \tilde{o}_{\mathrm{s}}) = \frac{\gamma(1-\tilde{x}_{\mathrm{s}})}{\tilde{g}_{x,\mathrm{an}}(\tilde{x}_{\mathrm{s}})[1-\tilde{g}_{o,\mathrm{an}}(\tilde{o}_{\mathrm{s}})]}, \tag{5.11}$$

$$\begin{aligned}\text{From Eq. 5.7}: \quad \beta(\tilde{s}_{\mathrm{s}}, \tilde{x}_{\mathrm{s}}, \tilde{o}_{\mathrm{s}}) = \quad & \Xi\gamma^{-1}\tilde{b}_{\mathrm{aer,s}}(\tilde{s}_{\mathrm{s}}, \tilde{o}_{\mathrm{s}})\tilde{g}_{s,\mathrm{aer}}(\tilde{s}_{\mathrm{s}})\tilde{g}_{o,\mathrm{aer}}(\tilde{o}_{\mathrm{s}}) \\ & + \alpha\gamma^{-1}\tilde{b}_{\mathrm{an,s}}(\tilde{x}_{\mathrm{s}}, \tilde{o}_{\mathrm{s}})\tilde{g}_{s,\mathrm{an}}(\tilde{s}_{\mathrm{s}})[1-\tilde{g}_{o,\mathrm{an}}(\tilde{o}_{\mathrm{s}})] \\ & - \Xi\gamma^{-1}\tilde{b}_{\mathrm{an,s}}(\tilde{x}_{\mathrm{s}}, \tilde{o}_{\mathrm{s}})\tilde{g}_{x,\mathrm{an}}(\tilde{x}_{\mathrm{s}})[1-\tilde{g}_{o,\mathrm{an}}(\tilde{o}_{\mathrm{s}})] \\ & + \Xi\tilde{s}_{\mathrm{s}},\end{aligned} \tag{5.12}$$

$$\text{From Eq. 5.8}: \quad \tilde{b}_{\mathrm{aer,s}}(\tilde{s}_{\mathrm{s}}, \tilde{o}_{\mathrm{s}}) = \frac{\kappa(\delta\Xi^{-1}-\tilde{o}_{\mathrm{s}})}{\tilde{\kappa}_{o,\mathrm{aer}}(\tilde{s}_{\mathrm{s}})\tilde{g}_{o,\mathrm{aer}}(\tilde{o}_{\mathrm{s}})}, \tag{5.13}$$

$$\text{From Eq. 5.10}: \quad \tilde{s}_{\mathrm{s}}(\tilde{o}_{\mathrm{s}}) = \frac{\tilde{s}_{1/2,\mathrm{aer}}}{\tilde{g}_{o,\mathrm{aer}}(\tilde{o}_{\mathrm{s}})\gamma^{-1}-1}. \tag{5.14}$$

In the AO state, $\tilde{b}_{\mathrm{an,s}} = 0$; thus, Eq. 5.11 yields $\tilde{x}_{\mathrm{s}} = 1$. Substituting this equality combined with Eq. 5.14 into Eqs. 5.12–5.13 then yields both β and $\tilde{b}_{\mathrm{aer,s}}$ as functions of solely $\tilde{o}_{\mathrm{s}}$. In-

verting $\beta(\tilde{o}_s)$ then yields our final result, the aerobes-only solutions for $\tilde{o}_s(\beta)$ and $\tilde{b}_{aer,s}(\beta)$ shown by the red curves in Fig. 5.6a,c. These solutions capture our numerical data (circles for I and VII) exactly—quantifying the intuition that in the AO state, aerobes consume the supplied simple sugar, mediated by oxygen consumption, and utilize it for their growth.

Transition to coexistence. As the oxygen concentration in the reactor decreases with increasing aerobe concentration, it eventually becomes low enough to sustain anaerobic growth as well (II in Figs. 5.1c–d, 5.6). Consequently, the microbial community transitions to the C state. Intuitively, this transition is analogous to the process by which a small inoculum of a new species (anaerobes) "invades" an existing colony of an indigenous species (aerobes)[123]—the onset of which is determined by the transition between $d\tilde{b}_{an}/d\tilde{t} < 0$ (anaerobic washout) and $d\tilde{b}_{an}/d\tilde{t} > 0$ (anaerobic invasion). Therefore, we begin by setting $d\tilde{b}_{an}/d\tilde{t} = 0$, which yields

$$\text{From Eq. 5.9}: \quad \tilde{g}_{o,an}(\tilde{o}_s) = 1 - \frac{\gamma\lambda^{-1}}{N(1-\Xi)\tilde{g}_{x,an}(\tilde{x}_s) + \tilde{g}_{s,an}(\tilde{s}_s)}. \tag{5.15}$$

In the AO state immediately prior to the transition to coexistence, $\tilde{b}_{an,s} = 0$, $\tilde{x}_s = 1$, and $\tilde{s}_s \ll \tilde{s}_{1/2,an}$ (Fig. 5.1d), and therefore, $\tilde{g}_{x,an}(\tilde{x}_s) = (1 + \tilde{x}_{1/2,an})^{-1}$ and $\tilde{g}_{s,an}(\tilde{s}_s) \approx \tilde{s}_s/\tilde{s}_{1/2,an} \ll N(1-\Xi)\tilde{g}_{x,an}(\tilde{x}_s)$. Substituting these simplifications into Eq. 5.15 then yields estimates for the critical oxygen concentration and corresponding simple sugar abundance at which the microbial community transitions to the C state: $\tilde{o}_{s,crit}/\tilde{o}_{1/2,an} \approx \lambda\gamma^{-1}N(1-\Xi)(1+\tilde{x}_{1/2,an})^{-1} - 1 = 10.0$ and $\beta_{aer,crit} \approx \Xi(\tilde{b}_{aer,s,crit} + \tilde{s}_{s,crit}) = 0.60$, respectively, where $\tilde{b}_{aer,s,crit}$ and $\tilde{s}_{s,crit}$ are given by substituting $\tilde{o}_{s,crit}$ into Eqs. 5.13–5.14. These estimates are in excellent agreement with the values $0.48 \leq \tilde{o}_{s,crit}/\tilde{o}_{1/2,an} \leq 10.6$ and $0.58 \leq \beta_{aer,crit} \leq 0.75$ obtained from our numerical simulation (Figs. 5.1d, 5.6)—quantifying the intuition that to transition to the

C state, oxygen consumption by aerobes must be sufficient to provide conditions for anaerobes to begin to "invade" the reactor without being washed out. For $\beta > \beta_{\text{aer,crit}}$, $\tilde{b}_{\text{an,s}} > 0$, and therefore, the AO solution indicated by the red lines in Fig. 5.6 becomes unstable (dashed).

The coexistence state. Without any simplifications, the steady-state relations obtained previously (Eqs. 5.11–5.15) jointly yield exact analytical solutions for $\tilde{s}_{\text{s}}$, $\tilde{x}_{\text{s}}$, β, $\tilde{b}_{\text{aer,s}}$, and $\tilde{b}_{\text{an,s}}$ as functions of solely $\tilde{o}_{\text{s}}$. Therefore, we expect that these equations fully describe the steady-state chemical and bacterial concentrations in the C state. To verify this expectation, we plot these quantities for varying $\tilde{o}_{\text{s}}$, as shown by the blue curves in Fig. 5.6. The solutions capture our numerical data (circles for III and IV) exactly—quantifying the intuition that in the C state, anaerobes break down complex carbohydrate to simple sugar, sustaining their own growth as well as that of the aerobes, which also consume oxygen and thereby maintain favorable conditions for the anaerobes to continue to survive.

Transition back to the aerobes-only state. Upon ramping down the simple sugar abundance β, coexistence persists until $\beta = \beta_{\text{coex,min}} < \beta_{\text{aer,crit}}$: the extant population of anaerobes shares simple sugar with the aerobes, enabling them to continue to grow, consume oxygen, and sustain anaerobic growth as well—despite the low value of β. The critical value $\beta_{\text{coex,min}}$ is then simply given by the minimum value of β for which a real-valued solution to the coexistence state (as obtained earlier, shown by the blue curves in Fig. 5.6) exists. We thereby estimate $\beta_{\text{coex,min}} \approx 0.29$, in excellent agreement with the value $0.25 \leq \beta_{\text{coex,min}} \leq 0.33$ obtained from our numerical simulation—quantifying the intuition that even lower levels of simple sugar abundance do not enable aerobes to consume enough oxygen to sustain anaerobic growth. As a result, the C solution indicated by the blue lines in

Fig. 5.6 becomes unstable (dashed) and the community transitions back to the AO state (VI). Within the context of dynamical systems theory, the oscillatory dynamics that arise prior to this transition (V) are characteristic of a limit cycle around a stable equilibrium point in phase space; indeed, the amplitude of the oscillations in e.g., oxygen concentration displays a hysteresis loop characteristic of a subcritical Hopf bifurcation, as shown in the inset to Fig. 5.6c. Further investigating the features of this instability will be an interesting direction for future work.

Taken together, these results demonstrate that not only does our full model recapitulate the two states (AO and C) observed in experiments, as well as the hysteretic transitions between them, but the steady-state solutions given by Eqs. 5.11–5.15 also provide a way to analytically describe these behaviors. Thus, to develop a broader understanding of the underlying biophysics, we next examine how these complex phenomena depend on both oxygen depletion and sharing of simple sugar more generally.

5.3.3 Oxygen depletion and nutrient sharing jointly enable coexistence

Given the necessity of oxygen depletion for coexistence, we hypothesize that increasing δ—which corresponds to reduced depletion of oxygen by the aerobes—will shift the AO-C transition to larger values of simple sugar abundance β. To test this hypothesis, we repeat the simulations shown in Fig. 5.6, ramping β up and then down between 0 and 1.2, keeping the same intermediate value of the sharing parameter $\Xi = 0.5$ but with varying δ. The results are shown in the state diagram shown in the middle panel of Fig. 5.7, with the results of Figs. 5.1 and 5.6 given by the points along $\delta = 3.9 \times 10^{-3}$. Consistent with the findings reported in Figs. 5.1 and 5.6, the microbial community initially exists in the

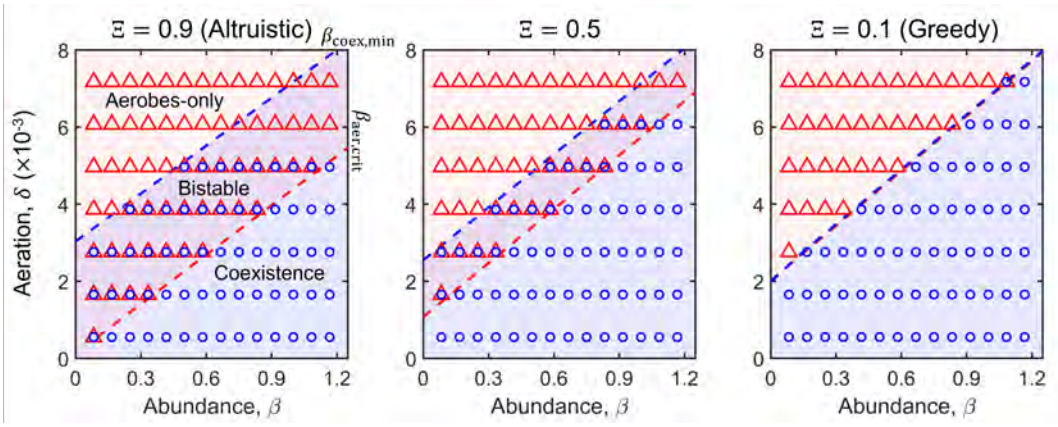

Figure 5.7: State diagrams for microbial communities under varying simple sugar and oxygen abundance. Symbols indicate the steady state reached by the microbial community in numerical simulations such as those in Fig. 5.6, holding a given value of the oxygen abundance parameter δ during ramp up (increasing simple sugar abundance β from 0 to 1.2) and ramp down (decreasing β from 1.2 to 0); red circles and blue triangles show the monostable aerobes-only (AO) and coexistence (C) states, respectively. Superimposed red circles and blue triangles show the bistable regime in which the AO state manifests during ramp up, while the C state manifests during ramp down. The transitions from AO to C and vice versa are described by the critical values $\beta = \beta_{aer,crit}$ and $\beta = \beta_{coex,min}$, respectively. The background shading and dashed lines show the stable states and critical β values predicted by our analytical steady-state solutions given by Eqs. 5.11–5.15. The analytical theory and numerical simulations show excellent agreement, except as expected for the case of large δ, for which $\beta_{aer,crit}$ exceeds the upper limit of the β explored; thus, coexistence is never reached and the bistable regime is precluded. In all cases, coexistence requires both oxygen depletion and nutrient sharing (small δ and large β). Moreover, the regime of bistability over which coexistence persists narrows in going from the "altruistic" limit of strong nutrient sharing (left panel $\Xi = 0.9$) to the "greedy" limit of weak nutrient sharing (right panel, $\Xi = 0.1$) by anaerobes.

aerobes-only (AO) state (red triangles) at low β, eventually transitioning to the coexistence (C) state (blue circles) as β is ramped up above a critical value $\beta_{aer,crit}$. Moreover, as expected for the case of large δ—for which $\beta_{aer,crit}$ exceeds the upper limit of the β explored—coexistence is never reached and the bistable regime is precluded. Upon ramping down β, the community persists in the C state in a bistable regime (superimposed red triangles and blue circles) until it eventually transitions back to the AO state below another critical value $\beta_{coex,min}$. In agreement with our hypothesis, these states and the transitions between them are sensitive to oxygen depletion: as oxygen depletion by the aerobes is reduced (increasing

δ), the AO state persists over a broader range of β, with both transitions between the AO and C states shifted to larger values of β. Our analytical steady-state solutions given by Eqs. 5.11–5.15 capture these shifts exactly; the shading in Fig. 5.7 corresponds to the top bar in Fig. 5.6, indicating the AO and C states as well as the bistable regime between them, and the dashed lines show the analytical solutions for $\beta_{\text{aer,crit}}$ (red) and $\beta_{\text{coex,min}}$ (blue). This close agreement quantifies the intuition that coexistence requires both oxygen depletion and nutrient sharing.

As a final demonstration of this point, we repeat these simulations, but for different values of the sharing parameter Ξ, as well. In particular, we explore two different limits: that of large $\Xi = 0.9$, in which the anaerobes are "altruistic" and share a larger fraction of the simple sugar liberated from complex carbohydrate with the entire community, and conversely that of small $\Xi = 0.1$, in which the anaerobes are instead "greedy" and only share a smaller fraction of the liberated simple sugar. The results are summarized by the left- and right-most panels of Fig. 5.7, respectively; the theoretical predictions for the resulting states and transitions between them, as determined using Eqs. 5.11–5.15, are shown by the shaded regions and dashed lines demarcating them, respectively. We find excellent agreement between the full numerical simulations and the analytical theory, confirming the validity of our biophysical analysis more broadly. In both cases of altruistic or greedy anaerobes, we again find that the overall community initially exists in the AO state at low simple sugar abundance β, eventually transitions to the C state with increasing β, and then continues to coexist with decreasing β until it transitions back to the AO state at even lower β. Moreover, we again find that the AO (C) state spans a wider range of β at larger (smaller) δ, highlighting the importance of oxygen depletion in enabling coexistence.

Confirming our expectation, nutrient sharing also plays a pivotal role in enabling coexistence. For example, in the altruistic case of $\Xi = 0.9$, coexistence persists over a broader window of $\{\beta, \delta\}$ after having been established i.e., during ramp down, as shown by the left-most panel of Fig. 5.7. Conversely, in the greedy case of $\Xi = 0.1$, the regime of bistability over which coexistence can persist nearly vanishes, as shown by the right-most panel. Close examination of the corresponding shifts in the boundaries between the AO and C states $\beta_{\text{aer,crit}}$ (red) and $\beta_{\text{coex,min}}$ (blue) reveals the underlying cause. Increased sharing of simple sugar (larger Ξ) increases $\beta_{\text{aer,crit}}$ (red line shifts to the right): it is more difficult to initially sustain the population of anaerobes if they utilize less of the complex carbohydrate for their own growth. However, despite this cost associated with altruism, it can also be beneficial. Increased sharing also decreases $\beta_{\text{coex,min}}$ (blue line shifts to the left): having been stably established in the community, anaerobes can continue to supply simple sugar to sustain aerobic growth, which in turn maintains the low-oxygen environment needed for the anaerobes themselves to continue to survive. Thus, as the old adage goes, *sharing is caring*.

5.4 Conclusion

Centuries of research have established that competition for limited resources—the "frequently recurring struggle for existence", as Charles Darwin put it[280]—can profoundly impact the growth and functioning of a multi-species community. It is now becoming increasingly clear that mutualistic interactions between distinct cell types also abound and play key roles in microbial communities; however, the dizzyingly-complex array of different interactions that arise in nature makes it challenging to isolate the influence of mutualism on community behavior. To address this challenge, in this chapter, we examined the

growth of a simplified aerobe-anaerobe community with mutualistic metabolic interactions between the two species: the anaerobes sustain aerobic growth by breaking down non-metabolized complex carbohydrate to shared simple sugar, while the aerobes sustain anaerobic growth in turn by consuming oxygen.

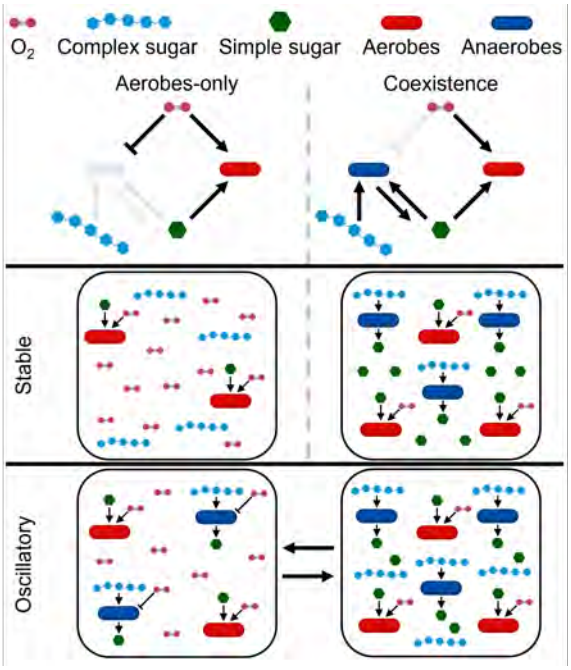

Figure 5.8: Summary of the different behaviors that arise in this microbial community. At low simple sugar abundance, the community is in the stable aerobes-only state (top and middle left) in which solely aerobes consume simple sugar, but are not concentrated enough to deplete oxygen for anaerobic growth. At high simple sugar abundance, the community transitions to the stable coexistence state (top and middle right) in which aerobes sufficiently deplete oxygen to sustain anaerobic growth, which in turn enables simple sugars to be liberated from complex carbohydrate and shared with the overall community. Upon subsequently decreasing the simple sugar abundance, before it transitions back to the aerobes-only stable state, the community oscillates between the low-oxygen (bottom right) and high-oxygen (bottom left) metastable states. In the former state, complex carbohydrate is rapidly broken down by anaerobes, causing aerobes to eventually run out of simple sugar and diminishing their ability to deplete oxygen—driving a transition to the latter state. In the latter, anaerobic breakdown of complex carbohydrate is slower, which enables complex carbohydrate and the subsequently liberated simple sugar to eventually become replenished, causing aerobes to increasingly deplete oxygen—driving a transition back to the former state.

Remarkably, despite its simplicity, we found that our model of this community recapitu-

lates many of the behaviors exhibited by laboratory and natural communities. In particular, it can adopt *multiple stable states*—transitioning between the states of aerobe-only (AO) growth and aerobe-anaerobe coexistence (C) in response to changes in carbon and oxygen fluxes, as summarized in Fig. 5.8. It also exhibits *multistability*—either of the AO and C states can arise under identical conditions, depending on the history of carbon and oxygen fluxes—leading to *hysteresis* and even *oscillatory* growth dynamics. Taken together, these results provide a simple demonstration of how mutualism can generate the complex growth behaviors that commonly arise in many different microbial communities. As such, our work complements the vast and insightful literature in microbial ecology focusing on the role of competition in influencing community behavior. Examining the influence of additional non-mutualistic interactions in our model would therefore be an interesting extension of work.

Indeed, a strength of our model is that it can reproduce the community behavior predicted by a more sophisticated metabolic model of a similar aerobe-anaerobe community[71] (as detailed further in Fig. 5.5). This more sophisticated model considers the full genome-scale network—comprising thousands of different metabolites and reactions—of metabolic interactions, which span the range from competitive to mutualistic. By contrast, ours only considers the interactions shown in Fig. 5.1a(ii), which are primarily mutualistic for the parameter values we used. This agreement between the model predictions could simply be fortuitous; but if not, it would corroborate the idea that consumption and secretion of only a small number of metabolites often dominates community behavior, as suggested by some experiments[72–74,76,82,84,276]. Further study is needed to test this idea and disentangle the relative contributions of different metabolites/metabolic pathways on

community-level functioning.

Another strength of our model is that, owing to its simplicity, it provides analytical predictions (Eqs. 5.11–5.15) and biophysical intuition for the different behaviors exhibited by this microbial community. Our approach could thus be used to inform the design of future experiments seeking to better characterize these behaviors, without requiring the large quantities of data—which may not be readily accessible—that are needed as inputs to sophisticated metabolic models. For example, the analytical predictions accurately describe the chemical and bacterial concentrations in both the AO and C states, as well as the transitions between the states (Figs. 5.6 and 5.7), governed by the interplay of both oxygen depletion and nutrient sharing. In particular, our analysis shows that for aerobe-anaerobe coexistence to arise, aerobes must be able to consume sufficient oxygen to provide conditions for anaerobes to begin to "invade" the reactor. It also reveals the origins of hysteresis when transitioning away from coexistence: anaerobe sharing of simple sugar with the aerobes enables them to continue to grow and consume oxygen, even in conditions of reduced simple sugar supply, thereby sustaining coexistence. Finally, our analysis demonstrates that oscillations in bacterial growth—which are usually thought to be caused by competition[77,82,88,88,96–102]—arise in this community instead due to periodic fluctuations in oxygen depletion by the aerobes that are coupled to fluctuations in carbon availability, mediated by anaerobic growth and metabolism. Consistent with this interpretation, removing the dependence of oxygen consumption by the aerobes on carbon availability—as may sometimes be the case[71]—abolishes the oscillations (Fig. 5.5). Guided by our findings, it would be interesting to further explore the nature of these oscillations in experiments, in addition to further characterizing them within the framework of dynamical systems theory.

The community considered here provides a simplified representation of the aerobe-anaerobe communities that play critical roles in human health, our environment, waste treatment, and other biotechnological processes[71,73,74,76,80,108–124,134–143,145–157]; thus, our work sets a foundation for future research with potential implications extending beyond microbiology and biological physics. To this end, our model takes a step toward capturing the essential biophysical processes underlying the complex dynamics of such microbial communities—but in doing so, necessarily required some simplifying assumptions and approximations. For example, we considered growth of two species in the well-mixed environment of a bioreactor, in which the distribution of all chemicals is spatially uniform, and the imposed oxygen and carbon fluxes are held constant until the community reaches a steady state. However, natural environments often have spatial and temporal fluctuations in nutrient availability[281,282], involving a larger repertoire of metabolites and mediators of metabolism, and with more than two microbial species that may adapt to changing conditions through evolutionary adaptation or phenotypic plasticity. These added complexities can give rise to fascinating new behaviors, leading to e.g., the emergence of spatial structure and facilitated coexistence in communities[72,73,88,139,158,283,284]. It could also be that microbes tune the extent of sharing (quantified by Ξ), which presumably could be under evolutionary selection, to e.g., optimize their individual growth or promote coexistence. Investigating these effects using the foundation provided by our model will be an important direction for future research.

6

Outlook and future directions

6.1 Chemotactic migration under confinement

A theory describing hopping, trapping, and crowding. The Keller-Segel equations can be derived elegantly from first principles[37]. One direction for future work is to account for hopping, trapping, and cell-cell collisions in this type of derivation so as to produce a model that incorporates features of confined motion. In particular, it would be interesting

to compare the functional form of μ_{crowd} with the resulting form of the motility parameters of such a model. Care must be taken to address spreading due to jammed growth, if including this feature is desired.

The effect of confinement on other motility mechanisms. Other mechanisms of motility other than flagellated motility may be more or less suited to traversing confined and/or disordered spaces? Understanding which modes of motility are better adapted to confinement than others is an important step toward understanding the evolutionary benefits of different motility mechanisms.

Rapid behavioral assays based on traveling fronts. The speed and spatial profile of a traveling front is readily obtainable from a single experiment and contains information about both motility and nutrient consumption. (In fact, some of the connections between parameters and observation were surprising to me: for example, the Monod constant for consumption strongly influences the width of the peak). It is feasible that a single experiment could be used to rapidly extract a large number of the relevant parameters of practical significance (consumption rate, Monod constant, the upper and lower bounds of logarithmic sensing, and the motility parameters for diffusion and chemotaxis). Such a protocol for parameter extraction may benefit from the use of machine learning given the large parameter space. Furthermore, high resolution photography may be sufficient to capture the essential features of the profile and its speed.

Pore size gradients. Pore size gradients emerge in some natural environments. How these gradients redirect traveling populations of cells is an interesting extension of the work shown in Chapter 2. Smooth gradients may alter the shape of the front, while crossing pore size regions with sharp boundaries may impact the direction of the traveling front as pore

size "fault lines" are crossed.

Impeded nutrient diffusion. In our experimental system, the porous hydrogels that hinder cell motion do not hinder nutrient diffusion. In some applications, the "solid" phase of the relevant medium may be, to some degree, impermeable to nutrient as well as cells. We postulate that nutrient impermeable grains would both change the overall diffusivity of the nutrient within the medium and also modify the local nutrient gradient conditions non-trivially: at the pore scale, local nutrient gradients would necessarily be directed along the free path towards the most nutrient abundance. Could this local gradient direction help guide cells through the pore space? Conversely, in the context of negative chemotaxis, it is not obvious whether the same directedness in the local nutrient gradient may enhance or hinder chemotaxis. Finally, it would be interesting to examine how to incorporate these effects into the Keller-Segel model.

6.2 Mixed microbial populations

Spatial variation. How aerobes and anaerobes collaborate in environments that are not well mixed is a fascinating and important direction for future work. It is unclear what spatial structures might form in the presence of an oxygen gradient and/or gradients of nutrient: Will the densities of aerobes and anearobes vary along the direction of an oxygen gradient alone, or will 2D or 3D patterns emerge? What is the role of directed or undirected motility in establishing spatial structure?

Using the work in Chapter 5 as a reference point leads to these additional interesting questions: compared with well mixed conditions, are spatially heterogeneous populations more robust to starvation? Are they more or less amenable to the initial start-up of an

anaerobe colony? Will oscillations as seen in Chapter 5 be sustained or prevented by spatial variation?

As with our approach in Chapters 2-4, combining numerical modeling with experiments of spatially heterogeneous aerobe and anaerobe communities will lead to a deeper understanding of the interactions between populations of cells. Furthermore, examining how structured environments mediate the spatially heterogeneous features of these systems would lead to important discoveries to better describe the growth and spreading of diverse microbial communities in complex environments.

A

A.1 List of symbols

Table A.1: Table of frequently used symbols.

Symbol	Quantity	Typical units
ξ	Mean pore size of surrounding medium	μm
φ	Void volume fraction of surrounding medium	none
l_{c}	Chord length within the void space of the surrounding medium	μm
l_{h}	Hop length	μm
d	Cell size	μm
τ_{h}	Hop time	s
τ_{t}	Trap time	s
D_c	Nutrient diffusion coefficient	$\mu\mathrm{m}^2/\mathrm{s}$
D_b	Bacteria active diffusion coefficient	$\mu\mathrm{m}^2/\mathrm{s}$
D_{b0}	Diffusion coefficient without the effects of cellular crowding	$\mu\mathrm{m}^2/\mathrm{s}$
χ	Bacteria chemotactic coefficient	$\mu\mathrm{m}^2/\mathrm{s}$
χ_0	Chemotactic coefficient without the effects of cellular crowding	$\mu\mathrm{m}^2/\mathrm{s}$
κ	Nutrient consumption rate	$\mathrm{mM}\ (\mathrm{cells/mL})^{-1}\ \mathrm{s}^{-1}$
γ	Cell growth rate	s^{-1}
c_{char}	Monod constant for half maximal consumption and growth	μM
c_-	Lower nutrient limit of logarithmic sensing	μM
c_+	Upper nutrient limit of logarithmic sensing	μM
v_{c}	Local chemotactic velocity	μm/min
v_{fr}	Traveling front velocity	μm/min
R_f, X_f	Leading edge position of front defined by a low density threshold	μm

References

[1] S. Balzan, C. de Almeida Quadros, R. De Cleva, B. Zilberstein, and I. Cecconello. Bacterial translocation: overview of mechanisms and clinical impact. *J. Gastroenterol. Hepatol.*, 22(4):464–471, 2007.

[2] Bonnie Chaban, H Velocity Hughes, and Morgan Beeby. The flagellum in bacterial pathogens: for motility and a whole lot more. In *Seminars in cell and developmental biology*, volume 46, pages 91–103. Elsevier, 2015.

[3] Sujit S Datta, Asher Preska Steinberg, and Rustem F Ismagilov. Polymers in the gut compress the colonic mucus hydrogel. *Proc. Natl. Acad. Sci. U. S. A.*, 113(26): 7041–7046, 2016.

[4] Michael W Harman, Star M Dunham-Ems, Melissa J Caimano, Alexia A Belperron, Linda K Bockenstedt, Henry C Fu, Justin D Radolf, and Charles W Wolgemuth. The heterogeneous motility of the Lyme disease spirochete in gelatin mimics dissemination through tissue. *Proc. Natl. Acad. Sci. U. S. A.*, 109(8):3059–3064, 2012.

[5] David Ribet and Pascale Cossart. How bacterial pathogens colonize their hosts and invade deeper tissues. *Microbes and infection*, 17(3):173–183, 2015.

[6] Anja Siitonen and Marjatta Nurminen. Bacterial motility is a colonization factor in experimental urinary tract infection. *Infect. Immun.*, 60(9):3918–3920, 1992.

[7] Renate Lux, James N Miller, No-Hee Park, and Wenyuan Shi. Motility and chemotaxis in tissue penetration of oral epithelial cell layers by Treponema denticola. *Infect. Immun.*, 69(10):6276–6283, 2001.

[8] Heather S O'Neil and Hesne Marquis. Listeria monocytogenes flagella are used for motility, not as adhesins, to increase host cell invasion. *Infect. Immun.*, 74(12): 6675–6681, 2006.

[9] CO Gill and N Penney. Penetration of bacteria into meat. *Applied and Environmental Microbiology*, 33(6):1284–1286, 1977.

[10] Hiroaki Shirai, Ashim K Datta, and Seiichi Oshita. Penetration of aerobic bacteria into meat: A mechanistic understanding. *Journal of Food Engineering*, 196:193–207, 2017.

[11] Dana N Thornlow, Emily L Brackett, Jonathan M Gigas, Nele Van Dessel, and Neil S Forbes. Persistent enhancement of bacterial motility increases tumor penetration. *Biotechnol. Bioeng.*, 112(11):2397–2405, 2015.

[12] Bhushan J Toley and Neil S Forbes. Motility is critical for effective distribution and accumulation of bacteria in tumor tissue. *Integrative Biology*, 4(2):165–176, 2012.

[13] Arnaud Dechesne, Gang Wang, Gamze Gülez, Dani Or, and Barth F Smets. Hydration-controlled bacterial motility and dispersal on surfaces. *Proceedings of the National Academy of Sciences*, 107(32):14369–14372, 2010.

[14] Rocheli de Souza, Adriana Ambrosini, and Luciane MP Passaglia. Plant growth-promoting bacteria as inoculants in agricultural soils. *Genet. Mol. Biol.*, 38(4):401–419, 2015.

[15] Gillian A Turnbull, J Alun W Morgan, John M Whipps, and Jon R Saunders. The role of bacterial motility in the survival and spread of Pseudomonas fluorescens in soil and in the attachment and colonisation of wheat roots. *FEMS Microbiol. Ecol*, 36(1):21–31, 2001.

[16] M Watt, JA Kirkegaard, and JB Passioura. Rhizosphere biology and crop productivity, a review. *Soil Res.*, 44(4):299–317, 2006.

[17] Olubukola Oluranti Babalola. Beneficial bacteria of agricultural importance. *Biotechnology letters*, 32(11):1559–1570, 2010.

[18] Joanna ST Adadevoh, C Andrew Ramsburg, and Roseanne Marie Ford. Chemotaxis increases the retention of bacteria in porous media with residual NAPL entrapment. *Environ. Sci. Technol.*, 52:7289–7295, 2018.

[19] Joanna S. T. Adadevoh, Sarah Triolo, C. Andrew Ramsburg, and Roseanne M. Ford. Chemotaxis increases the residence time of bacteria in granular media containing distributed contaminant sources. *Environ. Sci. Technol.*, 50(1):181–187, 2016.

[20] Roseanne M Ford and Ronald W Harvey. Role of chemotaxis in the transport of bacteria through saturated porous media. *Adv. Water Resour.*, 30(6-7):1608–1617, 2007.

[21] Meng Wang, Roseanne M Ford, and Ronald W Harvey. Coupled effect of chemotaxis and growth on microbial distributions in organic-amended aquifer sediments: Observations from laboratory and field studies. *Environ. Sci. Technol*, 42(10):3556–3562, 2008.

[22] Heather L Reddy and Roseanne M Ford. Analysis of biodegradation and bacterial transport: Comparison of models with kinetic and equilibrium bacterial adsorption. *Journal of contaminant hydrology*, 22(3-4):271–287, 1996.

[23] Howard C. Berg. *E. coli in motion*. Springer-Verlag, New York, 2004.

[24] Eric Lauga and Thomas R Powers. The hydrodynamics of swimming microorganisms. *Reports on progress in physics*, 72(9):096601, 2009.

[25] Howard C Berg. *Random walks in biology*. Princeton University Press, 2018.

[26] Douglas A Lauffenburger. Quantitative studies of bacterial chemotaxis and microbial population dynamics. *Microbial Ecology*, 22(1):175–185, 1991.

[27] Evelyn F Keller and Lee A Segel. Traveling bands of chemotactic bacteria: a theoretical analysis. *Journal of theoretical biology*, 30(2):235–248, 1971.

[28] Jonas Cremer, Tomoya Honda, Ying Tang, Jerome Wong-Ng, Massimo Vergassola, and Terence Hwa. Chemotaxis as a navigation strategy to boost range expansion. *Nature*, 575(7784):658–663, 2019.

[29] Xiongfei Fu, Setsu Kato, Junjiajia Long, Henry H Mattingly, Caiyun He, Dervis Can Vural, Steven W Zucker, and Thierry Emonet. Spatial self-organization resolves conflicts between individuality and collective migration. *Nature communications*, 9(1):1–12, 2018.

[30] Y. S. Dufour, X. Fu, L. Hernandez-Nunez, and T. Emonet. Limits of feedback control in bacterial chemotaxis. *PLoS Computational Biology*, 10:e1003694, 2014.

[31] Yiling Yang, Abiola M. Pollard, Carolin Höfler, Gernot Poschet, Markus Wirtz, Rüdiger Hell, and Victor Sourjik. Relation between chemotaxis and consumption of amino acids in bacteria. *Molecular microbiology*, 96(6):1272–1282, 2015.

[32] Julius Adler. Chemotaxis in bacteria. *Science*, 153(3737):708–716, 1966.

[33] Julius Adler. Effect of amino acids and oxygen on chemotaxis in Escherichia coli. *Journal of bacteriology*, 92(1):121–129, 1966.

[34] Jonathan Saragosti, Vincent Calvez, Nikolaos Bournaveas, Benoıt Perthame, Axel Buguin, and Pascal Silberzan. Directional persistence of chemotactic bacteria in a traveling concentration wave. *Proceedings of the National Academy of Sciences*, 108 (39):16235–16240, 2011.

[35] GM Odell and EF Keller. Traveling bands of chemotactic bacteria revisited. *Journal of Theoretical Biology*, 56:243–247, 1976.

[36] Evelyn F Keller and Garrett M Odell. Necessary and sufficient conditions for chemotactic bands. *Mathematical Biosciences*, 27(3-4):309–317, 1975.

[37] Maximilian Seyrich, Andrzej Palugniok, and Holger Stark. Traveling concentration pulses of bacteria in a generalized keller–segel model. *New Journal of Physics*, 21(10): 103001, 2019.

[38] Tapomoy Bhattacharjee and Sujit S Datta. Bacterial hopping and trapping in porous media. *Nat. Commun.*, 10(1):2075, 2019.

[39] Tapomoy Bhattacharjee and Sujit S Datta. Confinement and activity regulate bacterial motion in porous media. *Soft Matter*, 15(48):9920–9930, 2019.

[40] Cs Sándor, Andras Libal, Charles Reichhardt, and CJ Olson Reichhardt. Dynamic phases of active matter systems with quenched disorder. *Physical Review E*, 95(3): 032606, 2017.

[41] Oleksandr Chepizhko and Fernando Peruani. Diffusion, subdiffusion, and trapping of active particles in heterogeneous media. *Physical review letters*, 111(16):160604, 2013.

[42] Oleksandr Chepizhko and Fernando Peruani. Active particles in heterogeneous media display new physics. *The European Physical Journal Special Topics*, 224(7): 1287–1302, 2015.

[43] Alexandre Morin, Nicolas Desreumaux, Jean-Baptiste Caussin, and Denis Bartolo. Distortion and destruction of colloidal flocks in disordered environments. *Nature Physics*, 13:63–67, 2017.

[44] A J Wolfe and H C Berg. Migration of bacteria in semisolid agar. *Proc. Natl. Acad. Sci. U. S. A.*, 86(18):6973–6977, 1989.

[45] Ottavio A Croze, Gail P Ferguson, Michael E Cates, and Wilson CK Poon. Migration of chemotactic bacteria in soft agar: role of gel concentration. *Biophysical journal*, 101(3):525–534, 2011.

[46] Brian A Camley. Collective gradient sensing and chemotaxis: modeling and recent developments. *Journal of Physics: Condensed Matter*, 30(22):223001, 2018.

[47] Sebastian Gude, Erçağ Pinçe, Katja M Taute, Anne-Bart Seinen, Thomas S Shimizu, and Sander J Tans. Bacterial coexistence driven by motility and spatial competition. *Nature*, 578(7796):588–592, 2020.

[48] Ian Y Wong, Sarah Javaid, Elisabeth A Wong, Sinem Perk, Daniel A Haber, Mehmet Toner, and Daniel Irimia. Collective and individual migration following the epithelial–mesenchymal transition. *Nature materials*, 13(11):1063–1071, 2014.

[49] Oleksandr Chepizhko, Eduardo G Altmann, and Fernando Peruani. Optimal noise maximizes collective motion in heterogeneous media. *Physical review letters*, 110 (23):238101, 2013.

[50] John Toner, Nicholas Guttenberg, and Yuhai Tu. Swarming in the dirt: Ordered flocks with quenched disorder. *Physical review letters*, 121(24):248002, 2018.

[51] Ananyo Maitra. Active uniaxially ordered suspensions on disordered substrates. *Physical Review E*, 101(1):012605, 2020.

[52] David Yllanes, M Leoni, and MC Marchetti. How many dissenters does it take to disorder a flock? *New Journal of Physics*, 19(10):103026, 2017.

[53] Pradip K Bera and AK Sood. Motile dissenters disrupt the flocking of active granular matter. *Physical Review E*, 101(5):052615, 2020.

[54] Zahra Alirezaeizanjani, Robert Großmann, Veronika Pfeifer, Marius Hintsche, and Carsten Beta. Chemotaxis strategies of bacteria with multiple run modes. *Science advances*, 6(22):eaaz6153, 2020.

[55] Ricard Alert and Xavier Trepat. Physical models of collective cell migration. *Annual Review of Condensed Matter Physics*, 11:77–101, 2020.

[56] Ricard Alert, Carles Blanch-Mercader, and Jaume Casademunt. Active fingering instability in tissue spreading. *Physical review letters*, 122(8):088104, 2019.

[57] Michelle Driscoll, Blaise Delmotte, Mena Youssef, Stefano Sacanna, Aleksandar Donev, and Paul Chaikin. Unstable fronts and motile structures formed by microrollers. *Nature Physics*, 13(4):375–379, 2017.

[58] Amin Doostmohammadi, Sumesh P Thampi, and Julia M Yeomans. Defect-mediated morphologies in growing cell colonies. *Physical review letters*, 117(4): 048102, 2016.

[59] John J Williamson and Guillaume Salbreux. Stability and roughness of interfaces in mechanically regulated tissues. *Physical review letters*, 121(23):238102, 2018.

[60] Christopher J. Miles, Arthur A. Evans, Michael J. Shelley, and Saverio E. Spagnolie. Active matter invasion of a viscous fluid: Unstable sheets and a no-flow theorem. *Phys. Rev. Lett.*, 122:098002, 2019.

[61] G. Subramanian, Donald L. Koch, and Sean R. Fitzgibbon. The stability of a homogeneous suspension of chemotactic bacteria. *Phys. Fluids*, 23:041901, 2011.

[62] E. Lushi, R. E. Goldstein, and M. J. Shelley. Collective chemotactic dynamics in the presence of self-generated fluid flows. *Phys. Rev. E*, 86:040902(R), 2012.

[63] E. Lushi, R. E. Goldstein, and M. J. Shelley. Nonlinear concentration patterns and bands in autochemotactic suspensions. *Phys. Rev. E*, 98:052411, 2018.

[64] Martine Ben Amar and Carlo Bianca. Onset of nonlinearity in a stochastic model for auto-chemotactic advancing epithelia. *Scientific Reports*, 6(1):1–12, 2016.

[65] Martine Ben Amar. Collective chemotaxis and segregation of active bacterial colonies. *Scientific reports*, 6(1):1–9, 2016.

[66] M. Funaki, M. Mimura, and T. Tsujikawa. Travelling front solutions arising in the chemotaxis-growth model. *Interface. Free Bound.*, 8:223–245, 2006.

[67] M. P. Brenner, L. S. Levitov, and E. O. Budrene. Physical mechanisms for chemotactic pattern formation by bacteria. *Biophys. J.*, 74:1677–1693, 1998.

[68] M. Mimura and T. Tsujikawa. Aggregating pattern dynamics in a chemotaxis model including growth. *Physica A*, 230:499–543, 1996.

[69] H. Stark. Artificial chemotaxis of self-phoretic active colloids: Collective behavior. *Acc. Chem. Res.*, 51:2681–2688, 2018.

[70] Tim A Hoek, Kevin Axelrod, Tommaso Biancalani, Eugene A Yurtsev, Jinghui Liu, and Jeff Gore. Resource availability modulates the cooperative and competitive nature of a microbial cross-feeding mutualism. *PLoS biology*, 14(8):e1002540, 2016.

[71] Tahmineh Khazaei, Rory L Williams, Said R Bogatyrev, John C Doyle, Christopher S Henry, and Rustem F Ismagilov. Metabolic multistability and hysteresis in a model aerobe-anaerobe microbiome community. *Science advances*, 6(33):eaba0353, 2020.

[72] Francisco Díaz-Pascual, Martin Lempp, Kazuki Nosho, Hannah Jeckel, Jeanyoung K Jo, Konstantin Neuhaus, Raimo Hartmann, Eric Jelli, Mads Frederik Hansen, Alexa Price-Whelan, et al. Spatial alanine metabolism determines local growth dynamics of Escherichia coli colonies. *eLife*, 10:e70794, 2021.

[73] Steven Smriga, Davide Ciccarese, and Andrew R Babbin. Denitrifying bacteria respond to and shape microscale gradients within particulate matrices. *Communications Biology*, 4(1):1–9, 2021.

[74] Sammy Pontrelli, Rachel Szabo, Shaul Pollak, Julia Schwartzman, Daniela Ledezma-Tejeida, Otto X Cordero, and Uwe Sauer. Metabolic cross-feeding structures the assembly of polysaccharide degrading communities. *Science advances*, 8(8):eabk3076, 2022.

[75] Olga Ponomarova, Natalia Gabrielli, Daniel C Sévin, Michael Mülleder, Katharina Zirngibl, Katsiaryna Bulyha, Sergej Andrejev, Eleni Kafkia, Athanasios Typas, Uwe Sauer, et al. Yeast creates a niche for symbiotic lactic acid bacteria through nitrogen overflow. *Cell systems*, 5(4):345–357, 2017.

[76] Leonardo Oña, Samir Giri, Neele Avermann, Maximilian Kreienbaum, Kai M Thormann, and Christian Kost. Obligate cross-feeding expands the metabolic niche of bacteria. *Nature Ecology & Evolution*, 5(9):1224–1232, 2021.

[77] Frederick K Balagaddé, Lingchong You, Carl L Hansen, Frances H Arnold, and Stephen R Quake. Long-term monitoring of bacteria undergoing programmed population control in a microchemostat. *Science*, 309(5731):137–140, 2005.

[78] Jonathan Friedman, Logan M Higgins, and Jeff Gore. Community structure follows simple assembly rules in microbial microcosms. *Nature ecology & evolution*, 1(5):1–7, 2017.

[79] Noah Ribeck and Richard E Lenski. Modeling and quantifying frequency-dependent fitness in microbial populations with cross-feeding interactions. *Evolution*, 69(5):1313–1320, 2015.

[80] Joshua E Goldford, Nanxi Lu, Djordje Bajić, Sylvie Estrela, Mikhail Tikhonov, Alicia Sanchez-Gorostiaga, Daniel Segrè, Pankaj Mehta, and Alvaro Sanchez. Emergent simplicity in microbial community assembly. *Science*, 361(6401):469–474, 2018.

[81] Sylvie Estrela, Jean CC Vila, Nanxi Lu, Djordje Bajić, Maria Rebolleda-Gómez, Chang-Yu Chang, Joshua E Goldford, Alicia Sanchez-Gorostiaga, and Álvaro Sánchez. Functional attractors in microbial community assembly. *Cell Systems*, 13(1):29–42, 2022.

[82] Jintao Liu, Arthur Prindle, Jacqueline Humphries, Marçal Gabalda-Sagarra, Munehiro Asally, D Lee Dong-yeon, Jordi Garcia-Ojalvo, and Gürol M Süel. Metabolic co-dependence gives rise to collective oscillations within biofilms. *Nature*, 523 (7562):550–554, 2015.

[83] T Bush, IB Butler, A Free, and RJ Allen. Redox regime shifts in microbially mediated biogeochemical cycles. *Biogeosciences*, 12(12):3713–3724, 2015.

[84] Jintao Liu, Rosa Martinez-Corral, Arthur Prindle, Dong-yeon D Lee, Joseph Larkin, Marçal Gabalda-Sagarra, Jordi Garcia-Ojalvo, and Gürol M Süel. Coupling between distant biofilms and emergence of nutrient time-sharing. *Science*, 356 (6338):638–642, 2017.

[85] Tadashi Fukami. Historical contingency in community assembly: integrating niches, species pools, and priority effects. *Annual Review of Ecology, Evolution, and Systematics*, 46:1–23, 2015.

[86] Logan M Higgins, Jonathan Friedman, Hao Shen, and Jeff Gore. Co-occurring soil bacteria exhibit a robust competitive hierarchy and lack of non-transitive interactions. *BioRxiv*, page 175737, 2017.

[87] Erik S Wright and Kalin H Vetsigian. Inhibitory interactions promote frequent bistability among competing bacteria. *Nature communications*, 7(1):1–7, 2016.

[88] Jef Huisman and Franz J Weissing. Biological conditions for oscillations and chaos generated by multispecies competition. *Ecology*, 82(10):2682–2695, 2001.

[89] Didier Gonze, Leo Lahti, Jeroen Raes, and Karoline Faust. Multi-stability and the origin of microbial community types. *The ISME journal*, 11(10):2159–2166, 2017.

[90] Vanni Bucci, Serena Bradde, Giulio Biroli, and Joao B Xavier. Social interaction, noise and antibiotic-mediated switches in the intestinal microbiota. *PLoS computational biology*, 8(4):e1002497, 2012.

[91] Stefan Vet, Sophie de Buyl, Karoline Faust, Jan Danckaert, Didier Gonze, and Lendert Gelens. Bistability in a system of two species interacting through mutualism as well as competition: Chemostat vs. lotka-volterra equations. *PloS one*, 13 (6):e0197462, 2018.

[92] Daniel R Amor, Christoph Ratzke, and Jeff Gore. Transient invaders can induce shifts between alternative stable states of microbial communities. *Science Advances*, 6 (8):eaay8676, 2020.

[93] Vilhelm L Andersen Woltz, Clare I Abreu, Jonathan Friedman, and Jeff Gore. Emergence of alternative stable states in microbial communities in a fluctuating environment. *bioRxiv*, page 678367, 2019.

[94] Veronika Dubinkina, Yulia Fridman, Parth Pratim Pandey, and Sergei Maslov. Multistability and regime shifts in microbial communities explained by competition for essential nutrients. *eLife*, 8:e49720, 2019.

[95] Stefan Vet, Lendert Gelens, and Didier Gonze. Mutualistic cross-feeding in microbial systems generates bistability via an allee effect. *Scientific reports*, 10(1):1–12, 2020.

[96] Julian WT Wimpenny and Hamid Abdollahi. Growth of mixed cultures of Paracoccus denitrificans and Desulfovibrio desulfuricans in homogeneous and in heterogeneous culture systems. *Microbial ecology*, 22(1):1–13, 1991.

[97] Federico Bocci, Yoko Suzuki, Mingyang Lu, and José N Onuchic. Role of metabolic spatiotemporal dynamics in regulating biofilm colony expansion. *Proceedings of the National Academy of Sciences*, 115(16):4288–4293, 2018.

[98] Eugene Anatoly Yurtsev, Arolyn Conwill, and Jeff Gore. Oscillatory dynamics in a bacterial cross-protection mutualism. *Proceedings of the National Academy of Sciences*, 113(22):6236–6241, 2016.

[99] Rosa Martinez-Corral, Jintao Liu, Gürol M Süel, and Jordi Garcia-Ojalvo. Bistable emergence of oscillations in growing Bacillus subtilis biofilms. *Proc. Natl. Acad. Sci. U.S.A.*, 115(36):E8333–E8340, 2018.

[100] David W Graham, Charles W Knapp, Erik S Van Vleck, Katie Bloor, Teresa B Lane, and Christopher E Graham. Experimental demonstration of chaotic instability in biological nitrification. *The ISME journal*, 1(5):385–393, 2007.

[101] Ricardo López-Ruiz and Danièle Fournier-Prunaret. Complex behaviour in a discrete coupled logistic model for the symbiotic interaction of two species. *arXiv preprint nlin/0401045*, 2004.

[102] Bhavin S Khatri, Andrew Free, and Rosalind J Allen. Noise-driven oscillations in microbial population dynamics. *arXiv:1112.4836*, 2011.

[103] AG Fredrickson and Gregory Stephanopoulos. Microbial competition. *Science*, 213 (4511):972–979, 1981.

[104] Melanie Ghoul and Sara Mitri. The ecology and evolution of microbial competition. *Trends in microbiology*, 24(10):833–845, 2016.

[105] H Yoon, G Klinzing, and HW Blanch. Competition for mixed substrates by microbial populations. *Biotechnology and Bioengineering*, 19(8):1193–1210, 1977.

[106] S Pavlou, IG Kevrekidis, and G Lyberatos. On the coexistence of competing microbial species in a chemostat under cycling. *Biotechnology and bioengineering*, 35(3): 224–232, 1990.

[107] Robert MacArthur. Species packing and competitive equilibrium for many species. *Theoretical population biology*, 1(1):1–11, 1970.

[108] Brandon EL Morris, Ruth Henneberger, Harald Huber, and Christine Moissl-Eichinger. Microbial syntrophy: interaction for the common good. *FEMS microbiology reviews*, 37(3):384–406, 2013.

[109] Robert M May. *Stability and complexity in model ecosystems*. Princeton university press, 2019.

[110] Nick W Smith, Paul R Shorten, Eric Altermann, Nicole C Roy, and Warren C McNabb. The classification and evolution of bacterial cross-feeding. *Frontiers in Ecology and Evolution*, 7:153, 2019.

[111] Jana Schwarz-Linek, Jochen Arlt, Alys Jepson, Angela Dawson, Teun Vissers, Dario Miroli, Teuta Pilizota, Vincent A Martinez, and Wilson CK Poon. Escherichia coli as a model active colloid: A practical introduction. *Colloids and Surfaces B: Biointerfaces*, 137:2–16, 2016.

[112] Goutham N Vemuri, Elliot Altman, DP Sangurdekar, Arkady B Khodursky, and MA1472329 Eiteman. Overflow metabolism in Escherichia coli during steady-state growth: transcriptional regulation and effect of the redox ratio. *Applied and environmental microbiology*, 72(5):3653–3661, 2006.

[113] Nicole Paczia, Anke Nilgen, Tobias Lehmann, Jochem Gätgens, Wolfgang Wiechert, and Stephan Noack. Extensive exometabolome analysis reveals extended overflow metabolism in various microorganisms. *Microbial cell factories*, 11(1):1–14, 2012.

[114] Elżbieta Rozpędowska, Linda Hellborg, Olena P Ishchuk, Furkan Orhan, Silvia Galafassi, Annamaria Merico, Megan Woolfit, Concetta Compagno, and Jure Piškur. Parallel evolution of the make–accumulate–consume strategy in saccharomyces and dekkera yeasts. *Nature communications*, 2(1):1–7, 2011.

[115] Sriram Varahan and Sunil Laxman. Bend or break: how biochemically versatile molecules enable metabolic division of labor in clonal microbial communities. *Genetics*, 219(2):iyab109, 2021.

[116] Bernhard Schink. Synergistic interactions in the microbial world. *Antonie Van Leeuwenhoek*, 81(1):257–261, 2002.

[117] Annelie Pernthaler, Anne E Dekas, C Titus Brown, Shana K Goffredi, Tsegereda Embaye, and Victoria J Orphan. Diverse syntrophic partnerships from deep-sea methane vents revealed by direct cell capture and metagenomics. *Proceedings of the National Academy of Sciences*, 105(19):7052–7057, 2008.

[118] Samir Giri, Leonardo Oña, Silvio Waschina, Shraddha Shitut, Ghada Yousif, Christoph Kaleta, and Christian Kost. Metabolic dissimilarity determines the establishment of cross-feeding interactions in bacteria. *Current Biology*, 31(24):5547–5557, 2021.

[119] Sivan Elias and Ehud Banin. Multi-species biofilms: living with friendly neighbors. *FEMS microbiology reviews*, 36(5):990–1004, 2012.

[120] Mette Burmølle, Dawei Ren, Thomas Bjarnsholt, and Søren J Sørensen. Interactions in multispecies biofilms: do they actually matter? *Trends in microbiology*, 22 (2):84–91, 2014.

[121] Kai Wei Kelvin Lee, Saravanan Periasamy, Manisha Mukherjee, Chao Xie, Staffan Kjelleberg, and Scott A Rice. Biofilm development and enhanced stress resistance of a model, mixed-species community biofilm. *The ISME journal*, 8(4):894–907, 2014.

[122] Alan R Pacheco, Mauricio Moel, and Daniel Segrè. Costless metabolic secretions as drivers of interspecies interactions in microbial ecosystems. *Nature communications*, 10(1):1–12, 2019.

[123] Zhiyuan Li, Bo Liu, Sophia Hsin-Jung Li, Christopher G King, Zemer Gitai, and Ned S Wingreen. Modeling microbial metabolic trade-offs in a chemostat. *PLoS computational biology*, 16(8):e1008156, 2020.

[124] Lori Niehaus, Ian Boland, Minghao Liu, Kevin Chen, David Fu, Catherine Henckel, Kaitlin Chaung, Suyen Espinoza Miranda, Samantha Dyckman, Matthew Crum, et al. Microbial coexistence through chemical-mediated interactions. *Nature communications*, 10(1):1–12, 2019.

[125] A. Sanchez and J. Gore. Feedback between population and evolutionary dynamics determines the fate of social microbial populations. *PLoS Biol.*, 11(4):e1001547, 2013.

[126] C. Hauert, S. De Monte, J. Hofbauer, and K. Sigmund. Volunteering as red queen mechanism for cooperation in public goods games. *Science*, 296(5570):1129–1132, 2002.

[127] M. A. Nowak. *Evolutionary dynamics: exploring the equations of life*. Harvard university press, 2006.

[128] M. A. Nowak. Five rules for the evolution of cooperation. *Science*, 314(5805):1560–1563, 2006.

[129] C. Hauert, M. Holmes, and M. Doebeli. Evolutionary games and population dynamics: maintenance of cooperation in public goods games. *Proc. R. Soc. B: Biol. Sci.*, 273(1600):2565–2571, 2006.

[130] C. Hauert, J. Y. Wakano, and M. Doebeli. Ecological public goods games: cooperation and bifurcation. *Theor. Popul. Biol.*, 73(2):257–263, 2008.

[131] M. Perc, J. Gómez-Gardenes, A. Szolnoki, L. M. Floría, and Y. Moreno. Evolutionary dynamics of group interactions on structured populations: a review. *J. R. Soc. Interface*, 10(80):20120997, 2013.

[132] S. A. Levin. Public goods in relation to competition, cooperation, and spite. *Proc. Natl. Acad. Sci. U.S.A.*, 111(Supplement 3):10838–10845, 2014.

[133] J. Rauch, J. Kondev, and A. Sanchez. Cooperators trade off ecological resilience and evolutionary stability in public goods games. *J. R. Soc. Interface*, 14(127):20160967, 2017.

[134] Shady A Amin, David H Green, Mark C Hart, Frithjof C Küpper, William G Sunda, and Carl J Carrano. Photolysis of iron–siderophore chelates promotes bacterial–algal mutualism. *Proceedings of the National Academy of Sciences*, 106 (40):17071–17076, 2009.

[135] Martin T Croft, Andrew D Lawrence, Evelyne Raux-Deery, Martin J Warren, and Alison G Smith. Algae acquire vitamin B12 through a symbiotic relationship with bacteria. *Nature*, 438(7064):90–93, 2005.

[136] Diana H Wall and John C Moore. Interactions underground: soil biodiversity, mutualism, and ecosystem processes. *BioScience*, 49(2):109–117, 1999.

[137] Faina Kamilova, Lev V Kravchenko, Alexander I Shaposhnikov, Tatiyana Azarova, Nataliya Makarova, and Ben Lugtenberg. Organic acids, sugars, and L-tryptophane in exudates of vegetables growing on stonewool and their effects on activities of rhizosphere bacteria. *Molecular Plant-Microbe Interactions*, 19(3):250–256, 2006.

[138] Kathryn M Jones, Hajime Kobayashi, Bryan W Davies, Michiko E Taga, and Graham C Walker. How rhizobial symbionts invade plants: the Sinorhizobium–Medicago model. *Nature Reviews Microbiology*, 5(8):619–633, 2007.

[139] Benedict Borer, Robin Tecon, and Dani Or. Spatial organization of bacterial populations in response to oxygen and carbon counter-gradients in pore networks. *Nature communications*, 9(1):1–11, 2018.

[140] Suresh R Subashchandrabose, Balasubramanian Ramakrishnan, Mallavarapu Megharaj, Kadiyala Venkateswarlu, and Ravi Naidu. Mixotrophic cyanobacteria and microalgae as distinctive biological agents for organic pollutant degradation. *Environment international*, 51:59–72, 2013.

[141] Jeanyoung Jo, Alexa Price-Whelan, and Lars EP Dietrich. Gradients and consequences of heterogeneity in biofilms. *Nature Reviews Microbiology*, pages 1–15, 2022.

[142] Maria Avila, David M Ojcius, and Özlem Yilmaz. The oral microbiota: living with a permanent guest. *DNA and cell biology*, 28(8):405–411, 2009.

[143] Aimee K Wessel, Talha A Arshad, Mignon Fitzpatrick, Jodi L Connell, Roger T Bonnecaze, Jason B Shear, and Marvin Whiteley. Oxygen limitation within a bacterial aggregate. *MBio*, 5(2):e00992–14, 2014.

[144] Nick W Smith, Paul R Shorten, Eric H Altermann, Nicole C Roy, and Warren C McNabb. Hydrogen cross-feeders of the human gastrointestinal tract. *Gut Microbes*, 10(3):270–288, 2019.

[145] Harry J Flint, Karen P Scott, Sylvia H Duncan, Petra Louis, and Evelyne Forano. Microbial degradation of complex carbohydrates in the gut. *Gut microbes*, 3(4): 289–306, 2012.

[146] Jan Bures, Jiri Cyrany, Darina Kohoutova, Miroslav Förstl, Stanislav Rejchrt, Jaroslav Kvetina, Viktor Vorisek, and Marcela Kopacova. Small intestinal bacterial overgrowth syndrome. *World journal of gastroenterology: WJG*, 16(24):2978, 2010.

[147] Leon Zheng, Caleb J Kelly, and Sean P Colgan. Physiologic hypoxia and oxygen homeostasis in the healthy intestine. a review in the theme: cellular responses to hypoxia. *American Journal of Physiology-Cell Physiology*, 309(6):C350–C360, 2015.

[148] DJ Bradshaw, PD Marsh, GK Watson, and C Allison. Oral anaerobes cannot survive oxygen stress without interacting with facultative/aerobic species as a microbial commmunity. *Letters in Applied Microbiology*, 25(6):385–387, 1997.

[149] D Worlitzsch, C Rintelen, K Böhm, B Wollschläger, N Merkel, M Borneff-Lipp, and G Döring. Antibiotic-resistant obligate anaerobes during exacerbations of cystic fibrosis patients. *Clinical Microbiology and Infection*, 15(5):454–460, 2009.

[150] Pradeep K Singh, Amy L Schaefer, Matthew R Parsek, Thomas O Moninger, Michael J Welsh, and EP Greenberg. Quorum-sensing signals indicate that cystic fibrosis lungs are infected with bacterial biofilms. *Nature*, 407(6805):762–764, 2000.

[151] Ingo Schmidt, Olav Sliekers, Markus Schmid, Irina Cirpus, Marc Strous, Eberhard Bock, J Gijs Kuenen, and Mike SM Jetten. Aerobic and anaerobic ammonia oxidizing bacteria–competitors or natural partners? *FEMS microbiology ecology*, 39(3): 175–181, 2002.

[152] Michael Wagner and Alexander Loy. Bacterial community composition and function in sewage treatment systems. *Current opinion in biotechnology*, 13(3):218–227, 2002.

[153] Yun H Kong, Michael Beer, Robert J Seviour, Kenneth C Lindrea, and Gavin N Rees. Structure and functional analysis of the microbial community in an aerobic: anaerobic sequencing batch reactor (SBR) with no phosphorus removal. *Systematic and applied microbiology*, 24(4):597–609, 2001.

[154] Emily J Zakem, Amala Mahadevan, Jonathan M Lauderdale, and Michael J Follows. Stable aerobic and anaerobic coexistence in anoxic marine zones. *The ISME journal*, 14(1):288–301, 2020.

[155] Milla Salmela, Tapio Lehtinen, Elena Efimova, Suvi Santala, and Rahul Mangayil. Metabolic pairing of aerobic and anaerobic production in a one-pot batch cultivation. *Biotechnology for biofuels*, 11(1):1–13, 2018.

[156] Tom Fenchel and Bland Finlay. Oxygen and the spatial structure of microbial communities. *Biological Reviews*, 83(4):553–569, 2008.

[157] Siegfried E Vlaeminck, Akihiko Terada, Barth F Smets, Haydée De Clippeleir, Thomas Schaubroeck, Selin Bolca, Lien Demeestere, Jan Mast, Nico Boon, Marta Carballa, et al. Aggregate size and architecture determine microbial activity balance for one-stage partial nitritation and anammox. *Applied and environmental microbiology*, 76(3):900–909, 2010.

[158] John A Cole, Lars Kohler, Jamila Hedhli, and Zaida Luthey-Schulten. Spatially-resolved metabolic cooperativity within dense bacterial colonies. *BMC systems biology*, 9(1):1–17, 2015.

[159] Kai Zhuang, Mounir Izallalen, Paula Mouser, Hanno Richter, Carla Risso, Radhakrishnan Mahadevan, and Derek R Lovley. Genome-scale dynamic modeling of the competition between Rhodoferax and Geobacter in anoxic subsurface environments. *The ISME journal*, 5(2):305–316, 2011.

[160] Radhakrishnan Mahadevan, Jeremy S Edwards, and Francis J Doyle III. Dynamic flux balance analysis of diauxic growth in Escherichia coli. *Biophysical journal*, 83(3): 1331–1340, 2002.

[161] Milan JA Van Hoek and Roeland MH Merks. Emergence of microbial diversity due to cross-feeding interactions in a spatial model of gut microbial metabolism. *BMC systems biology*, 11(1):1–18, 2017.

[162] Eric Wolfsberg, Christopher P Long, and Maciek R Antoniewicz. Metabolism in dense microbial colonies: 13c metabolic flux analysis of E. coli grown on agar identifies two distinct cell populations with acetate cross-feeding. *Metabolic engineering*, 49:242–247, 2018.

[163] Tapomoy Bhattacharjee, Daniel B Amchin, Jenna A Ott, Felix Kratz, and Sujit S Datta. Chemotactic migration of bacteria in porous media. *Biophysical Journal*, 120 (16):3483–3497, 2021.

[164] Tapomoy Bhattacharjee, Steven M Zehnder, Kyle G Rowe, Suhani Jain, Ryan M Nixon, W Gregory Sawyer, and Thomas E Angelini. Writing in the granular gel medium. *Sci. Adv.*, 1(8):e1500655, 2015.

[165] Tapomoy Bhattacharjee, Christopher P Kabb, Christopher S O'Bryan, Juan M Urueenia, Brent S Sumerlin, W Gregory Sawyer, and Thomas E Angelini. Polyelectrolyte scaling laws for microgel yielding near jamming. *Soft matter*, 14(9):1559–1570, 2018.

[166] Tapomoy Bhattacharjee, Carmen J Gil, Samantha L Marshall, Juan M Urueña, Christopher S O'Bryan, Matt Carstens, Benjamin Keselowsky, Glyn D Palmer, Steve Ghivizzani, C Parker Gibbs, et al. Liquid-like solids support cells in 3D. *ACS Biomater. Sci. Eng.*, 2(10):1787–1795, 2016.

[167] Ann M O'Hara and Fergus Shanahan. The gut flora as a forgotten organ. *EMBO reports*, 7(7):688–693, 2006.

[168] Rodney D Berg. The indigenous gastrointestinal microflora. *Trends in microbiology*, 4(11):430–435, 1996.

[169] Francisco Díaz-Pascual, Raimo Hartmann, Martin Lempp, Lucia Vidakovic, Boya Song, Hannah Jeckel, Kai M Thormann, Fitnat H Yildiz, Jörn Dunkel, Hannes Link, et al. Breakdown of Vibrio cholerae biofilm architecture induced by antibiotics disrupts community barrier function. *Nature microbiology*, 4(12):2136–2145, 2019.

[170] Jing Yan, Benedikt Sabass, Howard Stone, Ned Wingreen, and Bonnie Bassler. Biofilm growth program and architecture revealed by single-cell live imaging. In *APS March Meeting Abstracts*, volume 2017, pages H5–006, 2017.

[171] Ray Keren, Adi Lavy, Boaz Mayzel, and Micha Ilan. Culturable associated-bacteria of the sponge Theonella swinhoei show tolerance to high arsenic concentrations. *Frontiers in Microbiology*, 6:154, 2015.

[172] David C Smith, Grieg F Steward, Richard A Long, and Farooq Azam. Bacterial mediation of carbon fluxes during a diatom bloom in a mesocosm. *Deep Sea Research Part II: Topical Studies in Oceanography*, 42(1):75–97, 1995.

[173] Douglas E Caldwell and Sarah J Caldwell. A Zoogloea sp. associated with blooms of Anabaena flos-aquae. *Canadian journal of microbiology*, 24(8):922–931, 1978.

[174] Edith A Widder. Bioluminescence in the ocean: origins of biological, chemical, and ecological diversity. *Science*, 328(5979):704–708, 2010.

[175] David W Armitage. Bacteria facilitate prey retention by the pitcher plant Darlingtonia californica. *Biology letters*, 12(11):20160577, 2016.

[176] Howard C Berg and Douglas A Brown. Chemotaxis in Escherichia coli analysed by three-dimensional tracking. *Nature*, 239:500–504, 1972.

[177] Linda Turner, William S Ryu, and Howard C Berg. Real-time imaging of fluorescent flagellar filaments. *Journal of bacteriology*, 182(10):2793–2801, 2000.

[178] Nikita Vladimirov, Dirk Lebiedz, and Victor Sourjik. Predicted auxiliary navigation mechanism of peritrichously flagellated chemotactic bacteria. *PLoS computational biology*, 6(3), 2010.

[179] Steven M Block, Jeffrey E Segall, and Howard C Berg. Impulse responses in bacterial chemotaxis. *Cell*, 31(1):215–226, 1982.

[180] Markus Hilpert. Lattice-boltzmann model for bacterial chemotaxis. *Journal of mathematical biology*, 51(3):302–332, 2005.

[181] Nicholas A Licata, Bitan Mohari, Clay Fuqua, and Sima Setayeshgar. Diffusion of bacterial cells in porous media. *Biophysical journal*, 110(1):247–257, 2016.

[182] Kevin Jan Duffy, Peter T Cummings, and Roseanne M Ford. Random walk calculations for bacterial migration in porous media. *Biophysical journal*, 68(3):800–806, 1995.

[183] M C Marchetti, J F Joanny, S Ramaswamy, T B Liverpool, J Prost, M Rao, and R A Simha. Hydrodynamics of soft active matter. *Reviews of Modern Physics*, 85:1143, 2013.

[184] Thierry Emonet, Charles M Macal, Michael J North, Charles E Wickersham, and Philippe Cluzel. Agentcell: a digital single-cell assay for bacterial chemotaxis. *Bioinformatics*, 21(11):2714–2721, 2005.

[185] P A Iglesias and P N Devreotes. Navigating through models of chemotaxis. *Current Opinion in Cell Biology*, 20(1):35–40, 2008.

[186] S Palagi and P Fischer. Bioinspired microrobots. *Nature Reviews Materials*, 3: 113–124, 2018.

[187] Ah-Young Jee, Sandipan Dutta, Yoon-Kyoung Cho, Tsvi Tlusty, and Steve Granick. Enzyme leaps fuel antichemotaxis. *Proc. Natl. Acad. Sci. U. S. A.*, 115(1):14–18, 2017.

[188] Charles Reichhardt and Cynthia J. Olson Reichhardt. Active matter transport and jamming on disordered landscapes. *Phys. Rev. E*, 90:012701, 2014.

[189] Clemens Bechinger, Roberto Di Leonardo, Hartmut Löwen, Charles Reichhardt, Giorgio Volpe, and Giovanni Volpe. Active particles in complex and crowded environments. *Rev. Mod. Phys.*, 88(4):045006, 2016.

[190] Charles Reichhardt and Cynthia J. Olson Reichhardt. Avalanche dynamics for active matter in heterogeneous media. *New J. Phys.*, 20:025002, 2018.

[191] Z. Tong, E. M. Balzer, M. R. Dallas, W. C. Hung, K. J. Stebe, and K. Konstantopoulos. Chemotaxis of cell populations through confined spaces at single-cell resolution. *PLoS One*, 7:e29211, 2012.

[192] Andrey Sokolov and Igor S Aranson. Physical properties of collective motion in suspensions of bacteria. *Physical review letters*, 109(24):248109, 2012.

[193] Jörn Dunkel, Sebastian Heidenreich, Knut Drescher, Henricus H Wensink, Markus Bär, and Raymond E Goldstein. Fluid dynamics of bacterial turbulence. *Physical review letters*, 110(22):228102, 2013.

[194] J Gachelin, A Rousselet, A Lindner, and E Clement. Collective motion in an active suspension of Escherichia coli bacteria. *New Journal of Physics*, 16(2):025003, 2014.

[195] Jonathan D Partridge, Gil Ariel, Orly Schvartz, Rasika M Harshey, and Avraham Be'er. The 3D architecture of a bacterial swarm has implications for antibiotic tolerance. *Scientific reports*, 8(1):1–11, 2018.

[196] Remy Colin, Knut Drescher, and Victor Sourjik. Chemotactic behaviour of Escherichia coli at high cell density. *Nature communications*, 10(1):1–11, 2019.

[197] Sungsu Park, Peter M Wolanin, Emil A Yuzbashyan, Hai Lin, Nicholas C Darnton, Jeffry B Stock, Pascal Silberzan, and Robert Austin. Influence of topology on bacterial social interaction. *Proceedings of the National Academy of Sciences*, 100(24): 13910–13915, 2003.

[198] Evelyn F Keller and Lee A Segel. Initiation of slime mold aggregation viewed as an instability. *J. Theor. Biol.*, 26(3):399–415, 1970.

[199] Evelyn F Keller and Lee A Segel. Model for chemotaxis. *Journal of theoretical biology*, 30(2):225–234, 1971.

[200] Frederick C Neidhardt, Philip L Bloch, and David F Smith. Culture medium for enterobacteria. *Journal of bacteriology*, 119(3):736–747, 1974.

[201] Jérôme Wong-Ng, Anna Melbinger, Antonio Celani, and Massimo Vergassola. The role of adaptation in bacterial speed races. *PLoS computational biology*, 12(6), 2016.

[202] Robert Mesibov and Julius Adler. Chemotaxis toward amino acids in Escherichia coli. *Journal of Bacteriology*, 112(1):315–326, 1972.

[203] Filippo Menolascina, Roberto Rusconi, Vicente I Fernandez, Steven Smriga, Zahra Aminzare, Eduardo D Sontag, and Roman Stocker. Logarithmic sensing in Bacillus subtilis aerotaxis. *NPJ Syst. Biol. Appl.*, 3(1):16036, 2017.

[204] M Lowder, A Unge, Ninwe Maraha, Janet K Jansson, J Swiggett, and JD Oliver. Effect of starvation and the viable-but-nonculturable state on Green Fluorescent Protein (GFP) fluorescence in GFP-tagged Pseudomonas fluorescens A506. *Applied and environmental microbiology*, 66(8):3160–3165, 2000.

[205] Silke Neumann, Nikita Vladimirov, Anna K Krembel, Ned S Wingreen, and Victor Sourjik. Imprecision of adaptation in Escherichia coli chemotaxis. *PLoS One*, 9(1): e84904, 2014.

[206] Robert G Wetzel. *Limnology: lake and river ecosystems*. Gulf professional publishing, 2001.

[207] Jeffrey R Hazel and Bruce D Sidell. A method for the determination of diffusion coefficients for small molecules in aqueous solution. *Analytical biochemistry*, 166(2): 335–341, 1987.

[208] Elena O Budrene and Howard C Berg. Complex patterns formed by motile cells of Escherichia coli. *Nature*, 349(6310):630–633, 1991.

[209] Elena O Budrene and Howard C Berg. Dynamics of formation of symmetrical patterns by chemotactic bacteria. *Nature*, 376(6535):49–53, 1995.

[210] N Mittal, E O Budrene, M P Brenner, and A van Oudenaarden. Motility of Escherichia coli cells in clusters formed by chemotactic aggregation. *Proceedings of the National Academy of Sciences*, 100(23):13259–13263, 2003.

[211] Jacques Monod. The growth of bacterial cultures. *Annual review of microbiology*, 3 (1):371–394, 1949.

[212] DE Woodward, R Tyson, MR Myerscough, JD Murray, EO Budrene, and HC Berg. Spatio-temporal patterns generated by Salmonella typhimurium. *Biophys. J.*, 68(5): 2181–2189, 1995.

[213] Talaat E Shehata and Allen G Marr. Effect of nutrient concentration on the growth of Escherichia coli. *J. Bacteriol.*, 107(1):210–216, 1971.

[214] G. D. Schellenberg and C. E Furlong. Resolution of the multiplicity of the glutamate and aspartate transport systems of Escherichia coli. *Journal of Biological Chemistry*, 252(24):9055–9064, 1977.

[215] Victor Sourjik and Ned S Wingreen. Responding to chemical gradients: bacterial chemotaxis. *Curr. Opin. Cell Biol.*, 24(2):262–268, 2012.

[216] Thomas S Shimizu, Yuhai Tu, and Howard C Berg. A modular gradient-sensing network for chemotaxis in Escherichia coli revealed by responses to time-varying stimuli. *Mol. Syst. Biol.*, 6(1):382, 2010.

[217] Yuhai Tu, Thomas S Shimizu, and Howard C Berg. Modeling the chemotactic response of Escherichia coli to time-varying stimuli. *Proc. Natl. Acad. Sci. U. S. A.*, 105(39):14855–14860, 2008.

[218] Yevgeniy V Kalinin, Lili Jiang, Yuhai Tu, and Mingming Wu. Logarithmic sensing in Escherichia coli bacterial chemotaxis. *Biophysical journal*, 96(6):2439–2448, 2009.

[219] Oren Shoval, Lea Goentoro, Yuval Hart, Avi Mayo, Eduardo Sontag, and Uri Alon. Fold-change detection and scalar symmetry of sensory input fields. *Proceedings of the National Academy of Sciences*, 107(36):15995–16000, 2010.

[220] Milena D Lazova, Tanvir Ahmed, Domenico Bellomo, Roman Stocker, and Thomas S Shimizu. Response rescaling in bacterial chemotaxis. *Proceedings of the National Academy of Sciences*, 108(33):13870–13875, 2011.

[221] Antonio Celani, Thomas S Shimizu, and Massimo Vergassola. Molecular and functional aspects of bacterial chemotaxis. *J. Stat. Phys.*, 144(2):219, 2011.

[222] David Rodabaugh and James R Wesson. On the efficient use of predictor-corrector methods in the numerical solution of differential equations. *NASA Technical Report*, TN D-2946, 1965.

[223] E Baylis Shanks. Solutions of differential equations by evaluations of functions. *Mathematics of Computation*, 20(93):21–38, 1966.

[224] Thomas Hillen and Kevin J Painter. A user's guide to PDE models for chemotaxis. *Journal of mathematical biology*, 58(1-2):183, 2009.

[225] Avaneesh V Narla, Jonas Cremer, and Terence Hwa. A traveling-wave solution for bacterial chemotaxis with growth. *Proceedings of the National Academy of Sciences*, 118(48), 2021.

[226] Jonas Cremer, Igor Segota, Chih-yu Yang, Markus Arnoldini, John T Sauls, Zhongge Zhang, Edgar Gutierrez, Alex Groisman, and Terence Hwa. Effect of flow and peristaltic mixing on bacterial growth in a gut-like channel. *Proceedings of the National Academy of Sciences*, 113(41):11414–11419, 2016.

[227] FDC Farrell, Oskar Hallatschek, D Marenduzzo, and B Waclaw. Mechanically driven growth of quasi-two-dimensional microbial colonies. *Physical review letters*, 111(16):168101, 2013.

[228] Daniel R Noguera, Gonzalo Pizarfo, David A Stahl, and Bruce E Rittmann. Simulation of multispecies biofilm development in three dimensions. *Water Science and Technology*, 39(7):123–130, 1999.

[229] Eshel Ben-Jacob, Inon Cohen, and David L Gutnick. Cooperative organization of bacterial colonies: from genotype to morphotype. *Annual review of microbiology*, 52 (1):779–806, 1998.

[230] Murray Eden. A two-dimensional growth process. In *Proceedings of the fourth Berkeley symposium on mathematical statistics and probability*, volume 4, pages 223–239. Univ of California Press Berkeley, 1961.

[231] JD Murray. *Mathematical biology II: spatial models and biomedical applications*, volume 3. Springer-Verlag, 2001.

[232] Hiroshi Fujikawa and Mitsugu Matsushita. Fractal growth of Bacillus subtilis on agar plates. *Journal of the physical society of Japan*, 58(11):3875–3878, 1989.

[233] Luis Cisneros, Christopher Dombrowski, Raymond E Goldstein, and John O Kessler. Reversal of bacterial locomotion at an obstacle. *Physical Review E*, 73 (3):030901, 2006.

[234] Knut Drescher, Jörn Dunkel, Luis H Cisneros, Sujoy Ganguly, and Raymond E Goldstein. Fluid dynamics and noise in bacterial cell–cell and cell–surface scattering. *Proceedings of the National Academy of Sciences*, 108(27):10940–10945, 2011.

[235] D Dell'Arciprete, ML Blow, AT Brown, FDC Farrell, Juho S Lintuvuori, AF McVey, D Marenduzzo, and Wilson CK Poon. A growing bacterial colony in two dimensions as an active nematic. *Nature communications*, 9(1):1–9, 2018.

[236] Dmitri Volfson, Scott Cookson, Jeff Hasty, and Lev S Tsimring. Biomechanical ordering of dense cell populations. *Proceedings of the National Academy of Sciences*, 105(40):15346–15351, 2008.

[237] Salvatore Torquato and B Lu. Chord-length distribution function for two-phase random media. *Physical Review E*, 47(4):2950, 1993.

[238] Jean-François Mercier, Gary W Slater, and Hong L Guo. Numerically exact diffusion coefficients for lattice systems with periodic boundary conditions. I. theory. *The Journal of chemical physics*, 110(12):6050–6056, 1999.

[239] Isaac Klapper and Jack Dockery. Finger formation in biofilm layers. *SIAM Journal on Applied Mathematics*, 62(3):853–869, 2002.

[240] DA Head. Linear surface roughness growth and flow smoothening in a three-dimensional biofilm model. *Physical Review E*, 88(3):032702, 2013.

[241] Louise Dyson and Ruth E Baker. The importance of volume exclusion in modelling cellular migration. *Journal of mathematical biology*, 71(3):691–711, 2015.

[242] Youguang Ma, Chunying Zhu, Peisheng Ma, and KT Yu. Studies on the diffusion coefficients of amino acids in aqueous solutions. *Journal of Chemical & Engineering Data*, 50(4):1192–1196, 2005.

[243] Tapomoy Bhattacharjee, Daniel B Amchin, Ricard Alert, Jenna Anne Ott, and Sujit Sankar Datta. Chemotactic smoothing of collective migration. *eLife*, 11:e71226, 2022.

[244] Eric K Chu, Onur Kilic, Hojung Cho, Alex Groisman, and Andre Levchenko. Self-induced mechanical stress can trigger biofilm formation in uropathogenic Escherichia coli. *Nature communications*, 9(1):1–10, 2018.

[245] Yang Bai, Caiyun He, Pan Chu, Junjiajia Long, Xuefei Li, and Xiongfei Fu. Spatial modulation of individual behaviors enables an ordered structure of diverse phenotypes during bacterial group migration. *eLife*, 10:e67316, 2021.

[246] Hiroshi Fujikawa and Mitsugu Matsushita. Fractal growth of Bacillus subtilis on agar plates. *J. Phys. Soc. Jpn.*, 58:3875–3878, 1989.

[247] Juan A. Bonachela, Carey D. Nadell, Joao B. Xavier, and Simon A. Levin. Universality in bacterial colonies. *J. Stat. Phys.*, 144:303–315, 2011.

[248] Carey Nadell, Kevin R. Foster, and Joao B. Xavier. Emergence of spatial structure in cell groups and the evolution of cooperation. *PLoS Comput. Biol.*, 6(3):e1000716, 2010.

[249] F. D. C. Farrell, O. Hallatschek, D. Marenduzzo, and B. Waclaw. Mechanically driven growth of quasi-two-dimensional microbial colonies. *Phys. Rev. Lett.*, 111: 168101, 2013.

[250] Sarah Trinschek, Karin John, and Uwe Thiele. Modelling of surfactant-driven front instabilities in spreading bacterial colonies. *Soft Matter*, 14(22):4464–4476, 2018.

[251] Rosalind J Allen and Bartlomiej Waclaw. Bacterial growth: A statistical physicist's guide. *Reports on Progress in Physics*, 82(1):016601, 2018.

[252] R P Tittsler and L A Sandholzer. The use of semi-solid agar for the detection of bacterial motility. *J. Bacteriology*, 31(6):575–580, 1936.

[253] Mehrana R Nejad and Ali Najafi. Chemotaxis mediated interactions can stabilize the hydrodynamic instabilities in active suspensions. *Soft Matter*, 15(15):3248–3255, 2019.

[254] Pere Roca-Cusachs, Raimon Sunyer, and Xavier Trepat. Mechanical guidance of cell migration: lessons from chemotaxis. *Current opinion in cell biology*, 25(5):543–549, 2013.

[255] Raimon Sunyer, Vito Conte, Jorge Escribano, Alberto Elosegui-Artola, Anna Labernadie, Léo Valon, Daniel Navajas, José Manuel García-Aznar, José J Muñoz, Pere Roca-Cusachs, et al. Collective cell durotaxis emerges from long-range intercellular force transmission. *Science*, 353(6304):1157–1161, 2016.

[256] Ricard Alert and Jaume Casademunt. Role of substrate stiffness in tissue spreading: Wetting transition and tissue durotaxis. *Langmuir*, 35(23):7571–7577, 2018.

[257] Pierre Illien, Ramin Golestanian, and Ayusman Sen. 'Fuelled' motion: phoretic motility and collective behaviour of active colloids. *Chem. Soc. Rev.*, 46(18):5508–5518, 2017.

[258] Benno Liebchen and Hartmut Löwen. Synthetic chemotaxis and collective behavior in active matter. *Acc. Chem. Res.*, 51(12):2982–2990, 2018.

[259] Holger Stark. Artificial chemotaxis of self-phoretic active colloids: Collective behavior. *Acc. Chem. Res.*, 51(11):2681–2688, 2018.

[260] Mite Mijalkov, Austin McDaniel, Jan Wehr, and Giovanni Volpe. Engineering sensorial delay to control phototaxis and emergent collective behaviors. *Phys. Rev. X*, 6 (1):011008, 2016.

[261] Jaime Agudo-Canalejo, Pierre Illien, and Ramin Golestanian. Phoresis and enhanced diffusion compete in enzyme chemotaxis. *Nano Lett.*, 18(4):2711–2717, 2018.

[262] Farzad Mohajerani, Xi Zhao, Ambika Somasundar, Darrell Velegol, and Ayusman Sen. A theory of enzyme chemotaxis: From experiments to modeling. *Biochemistry*, 57(43):6256–6263, 2018.

[263] Eric Theveneau, Lorena Marchant, Sei Kuriyama, Mazhar Gull, Barbara Moepps, Maddy Parsons, and Roberto Mayor. Collective chemotaxis requires contact-dependent cell polarity. *Dev. Cell*, 19(1):39–53, 2010.

[264] Rebecca McLennan, Louise Dyson, Katherine W. Prather, Jason A. Morrison, Ruth E. Baker, Philip K. Maini, and Paul M. Kulesa. Multiscale mechanisms of cell migration during development: theory and experiment. *Development*, 139(16): 2935–2944, 2012.

[265] Gema Malet-Engra, Weimiao Yu, Amanda Oldani, Javier Rey-Barroso, Nir S Gov, Giorgio Scita, and Loïc Dupré. Collective cell motility promotes chemotactic prowess and resistance to chemorepulsion. *Curr. Biol.*, 25(2):242–50, 2015.

[266] Alberto Puliafito, Alessandro De Simone, Giorgio Seano, Paolo Armando Gagliardi, Laura Di Blasio, Federica Chianale, Andrea Gamba, Luca Primo, and Antonio Celani. Three-dimensional chemotaxis-driven aggregation of tumor cells. *Sci. Rep.*, 5(1):15205, 2015.

[267] Luke Tweedy, Peter A Thomason, Peggy I Paschke, Kirsty Martin, Laura M Machesky, Michele Zagnoni, and Robert H Insall. Seeing around corners: Cells solve mazes and respond at a distance using attractant breakdown. *Science*, 369(6507): eaay9792, 2020.

[268] F Beroz, J Yan, Y Meir, B Sabass, HA Stone, BL Bassler, and NS Wingreen. Verticalization of bacterial biofilms. *Nat. Phys.*, 14:954, 2018.

[269] Chenyi Fei, Sheng Mao, Jing Yan, Ricard Alert, Howard A Stone, Bonnie L Bassler, Ned S Wingreen, and Andrej Košmrlj. Nonuniform growth and surface friction determine bacterial biofilm morphology on soft substrates. *Proceedings of the National Academy of Sciences*, 117(14):7622–7632, 2020.

[270] J Yan, C Fei, S Mao, A Moreau, NS Wingreen, A Kosmrlj, HA Stone, and BL Bassler. Mechanical instability and interfacial energy drive biofilm morphogenesis. *eLife*, 8:e43920, 2019.

[271] J Yan, CD Nadell, HA Stone, NS Wingreen, and BL Bassler. Extracellular-matrix-mediated osmotic pressure drives Vibrio cholerae biofilm expansion and cheater exclusion. *Nat. Commun.*, 8:327, 2017.

[272] Katherine Copenhagen, Ricard Alert, Ned S Wingreen, and Joshua W Shaevitz. Topological defects promote layer formation in Myxococcus xanthus colonies. *Nature Physics*, 17(2):211–215, 2021.

[273] William PJ Smith, Yohan Davit, James M Osborne, Wook Kim, Kevin R Foster, and Joe M Pitt-Francis. Cell morphology drives spatial patterning in microbial communities. *Proceedings of the National Academy of Sciences*, 114(3):E280–E286, 2017.

[274] P Ghosh, J Mondal, E Ben-Jacob, and H Levine. Mechanically-driven phase separation in a growing bacterial colony. *Proceedings of the National Academy of Sciences*, 112:E2166–E2173, 2015.

[275] Qiuting Zhang, Jian Li, Japinder Nijjer, Haoran Lu, Mrityunjay Kothari, Ricard Alert, Tal Cohen, and Jing Yan. Morphogenesis and cell ordering in confined bacterial biofilms. *Proceedings of the National Academy of Sciences*, 118(31), 2021.

[276] Kapil Amarnath, Avaneesh V Narla, Sammy Pontrelli, Jiajia Dong, Tolga Caglar, Brian R Taylor, Julia Schwartzman, Uwe Sauer, Otto X Cordero, and Terence Hwa. Stress-induced cross-feeding of internal metabolites provides a dynamic mechanism of microbial cooperation. *bioRxiv*, 2021.

[277] Carine Douarche, Axel Buguin, Hanna Salman, and Albert Libchaber. E. coli and oxygen: a motility transition. *Physical review letters*, 102(19):198101, 2009.

[278] Adam Z Rosenthal, Yutao Qi, Sahand Hormoz, Jin Park, Sophia Hsin-Jung Li, and Michael B Elowitz. Metabolic interactions between dynamic bacterial subpopulations. *eLife*, 7:e33099, 2018.

[279] Alma Dal Co, Simon Van Vliet, and Martin Ackermann. Emergent microscale gradients give rise to metabolic cross-feeding and antibiotic tolerance in clonal bacterial populations. *Philosophical Transactions of the Royal Society B*, 374(1786):20190080, 2019.

[280] Charles Darwin. *On the origin of species*. John Murray, 1859.

[281] Jack A Gilbert, Joshua A Steele, J Gregory Caporaso, Lars Steinbrück, Jens Reeder, Ben Temperton, Susan Huse, Alice C McHardy, Rob Knight, Ian Joint, et al. Defining seasonal marine microbial community dynamics. *ISME J.*, 6(2):298–308, 2012.

[282] Samuel A Smits, Jeff Leach, Erica D Sonnenburg, Carlos G Gonzalez, Joshua S Lichtman, Gregor Reid, Rob Knight, Alphaxard Manjurano, John Changalucha, Joshua E Elias, et al. Seasonal cycling in the gut microbiome of the Hadza hunter-gatherers of Tanzania. *Science*, 357(6353):802–806, 2017.

[283] Tom Burkart and Erwin Frey. Periodic temporal environmental variations induce coexistence in resource competition models. *arXiv:2202.11635*, 2022.

[284] Immanuel Meyer, Bnaya Steinmetz, and Nadav M Shnerb. Species coexistence and temporal environmental fluctuations: a quantitative comparison between stochastic and seasonal variations. *bioRxiv*, 2021.

This thesis was typeset using LaTeX, originally developed by Leslie Lamport and based on Donald Knuth's TeX. The body text is set in 11 point Egenolff-Berner Garamond, a revival of Claude Garamont's humanist typeface. The above illustration, "Science Experiment 02", was created by Ben Schlitter and released under CC BY-NC-ND 3.0. A template that can be used to format a PhD thesis with this look and feel has been released under the permissive MIT (X11) license, and can be found online at github.com/suchow/Dissertate or from its author, Jordan Suchow, at suchow@post.harvard.edu.